UNIVERSITÁ DEGLI STUDI DI PARMA
Dottorato di Ricerca in Fisica
Ciclo XXV

Nanostructured magnetic materials for sensors and biomedicine

Coordinatore:
Prof. PIERPAOLO LOTTICI

Supervisori:
Prof. Antonio Deriu
Dott.ssa Franca Albertini
Dott.ssa Francesca Casoli
Dott. Salvatore Iannotta

Dottoranda:
Valentina Chiesi

Anno Accademico 2012/2013

To my parents Rodolfo and Mara

Introduction

In the last twenty years the discovery of new nanostructured materials and nanoscale physical effects have paved the way for several technologies; thanks to these discoveries *nanotechnology* is now a word used in our everyday language. In the nanoworld the properties of materials are completely different from the bulk and can give rise to new and surprising solutions to problems arising in very different fields, from medicine, to energy production or telecommunications. Nanotechnology allows, for instance, to have smaller, easier to use, more sensitive and lighter sensors. In medicine, the day when nano-vectors and nano-manipulators will become reality is not so far.

The research activity presented in this thesis focuses on different magnetic nanostructures, i.e., thin films, nanoparticles and nanocomposites, characterized by physical properties which can fruitfully be exploited in sensors and biomedicine. Novel properties in magnetic nanostructures can arise for a number of reasons, such as confinement of the magnetic material into two- or one-dimensional structures and close proximity with other materials in layered or nanocomposite structures. When specific functional magnetic properties are due to size reduction, an in depth study of the correlation between magnetism and size reduction is mandatory for the nanostructured material optimization for a given application. For this reason, we have followed the same methodological approach for each studied material: starting from the material design, passing through a complete structural and magnetic characterization has allowed us, in the most prominent cases, to model the magnetic properties and give an answer to application requirements.

This thesis is made up of six chapters. In the first chapter basic elements of magnetism and magnetic materials are recalled, which are useful to understand the experimental results. In particular the attention is on the effect of size reduction on magnetic phenomenology and magnetization processes, on surface effects in thin films and nanoparticles and on the effect of interactions between magnetic nanoparticles.

In the second chapter the experimental techniques used to characterize thin films and nanoparticles are shown.

In the third chapter the main results obtained on amorphous thin films, showing soft magnetic properties, are reported. After a detailed investigation of the correlation between growth parameters and film properties, these have been optimized for exploiting the thin film as magnetic core in flux-gate and hall sensors.

Chapter four presents the results on Iron oxide nanoparticles, which, after suitable surface functionalization, have been studied as magnetic hyperthermia mediators and for magnetic separation. The mere effect of size reduction is here accompanied by other effects, such as aggregation, nanoparticles interactions, exchange-bias effect in core-shell nanoparticles, which enrich the systems phenomenology.

Finally, chapter five summarizes the results obtained on composite and multifunctional nanostructures, characterized by different functional properties. In particular, the superparamagnetic properties of magnetite nanoparticles are coupled to the semiconducting properties of Zinc oxide tetrapods and Silicon carbide nanowires. At the end of this chapter the results obtained on nanodisks of Ni-Mn-Ga Heusler alloy, which is an intrinsically multifunctional material, are reported.

Contents

Chapter 1

Elements of magnetism

1.1 Magnetic free energy

The dependence of a ferromagnetic material on an external magnetic applied field can be described taking into account the material free energy where different terms sum to give the total free energy, in particular exchange, magnetic anisotropy, magnetostatic and magneto-elastic energies, that originate from different microscopic interactions. The hysteresis loop and the magnetic domains derive from the competition between these different energy terms. In the following section a description of the energy contributions is given.

1.1.1 Dipolar energy

The first type of energy between magnetic dipoles μ_1 and $\mu_2$that are separated by a vector $\vec{r}$ is

$$E_{dipolar} = \frac{\mu_0}{4\pi r^3}\left(\vec{\mu_1}\cdot\vec{\mu_2} - \frac{3}{r^2}\left(\vec{\mu_1}\cdot\vec{r}\right)\left(\vec{\mu_2}\cdot\vec{r}\right)\right) \tag{1.1}$$

where where μ_0 is the vacuum permeability.

As we can see in 1.2 the intensity of energy decreases as r^{-3}, so if we choose typical values such as $\mu_1 = \mu_2 = 1\mu_B$ and $r = 0.2nm$, assuming $\mu_1||\mu_2$ and $\mu||r$ the dipolar energy becomes

$$E_{dipolar} = \frac{\mu_0\mu_B^2}{2\pi r^3} = 2.1\cdot 10^{(-24)}J \tag{1.2}$$

This value is too small to cause ferromagnetic order and now we introduce the exchange energy.

1.1.2 Exchange energy and molecular field

Ferromagnetic materials are characterized by the presence of exchange interaction that gives rise to a long range order of magnetic moments [1].

The exchange interaction has a quantum mechanical origin, that depends on the Pauli principle

and Coulomb interaction. If we take into account a perfect crystal of magnetic atoms, each of them with a magnetic moment $\vec{\mu} = g\mu_B\vec{S}$, in which only the spin part is present, where g is the Landé factor, S is the spin and μ_B is the Bohr magnetron. The exchange Heisenberg Hamiltonian can be written as:

$$H = -2\sum_{i<j} J_{ij}\vec{S}_i \cdot \vec{S}_j \tag{1.3}$$

we consider the case of a ferromagnetic material where the exchange integral is $J_{ij} > 0$.
We can obtain the Weiss's molecular field approximation, by substituting the singular spin with the average value calculated above all the other spins.
Then the equation 1.3 for the spin i becomes:

$$H_i = -2\vec{S}_i \sum_j J_{ij} \left\langle \vec{S}_j \right\rangle \tag{1.4}$$

For this reason we can consider the effect of exchange interaction as an average field given by:

$$\vec{H}_m = 2\frac{\sum_j J_{ij} \left\langle \vec{S}_j \right\rangle}{\mu_0 g\mu_B} \tag{1.5}$$

where μ_0 is the vacuum permeability. This field is called molecular field.
If the exchange integral is considered as $J_{ij} = J = constant$ and the sum is over z nearest neighbors, the field in equation 1.5 becomes

$$\vec{H}_m = 2\frac{zJ \left\langle \vec{S}_j \right\rangle}{\mu_0 g\mu_B} \tag{1.6}$$

In the above expression 1.6 we can obtain the magnetization over N spins as:

$$\vec{M} = N \left\langle \vec{S}_j \right\rangle g\mu_B \tag{1.7}$$

The eigenvalues of Hamiltonian in the presence of the magnetic field H_0 and exchange field H_m are given by

$$E_m = -g\mu_B(H_0 + H_m)m \tag{1.8}$$

where $m = S, S-1, ..., -S$ and the magnetization becomes

$$M = NSg\mu_B B_S(\eta) \tag{1.9}$$

where

$$B_S(\eta) = \left[\left(\frac{2S+1}{2S}\right) coth\left(\frac{(2S+1)\eta}{2S}\right) - \left(\frac{1}{2S}\right) coth\left(\frac{\eta}{2S}\right)\right] \tag{1.10}$$

and

$$\eta = \frac{Sg\mu_B\left(H_0 + H_m\right)}{k_B T} \tag{1.11}$$

As well known from the above theory of the molecular field, we can define the Curie temperature, that results dependent on the exchange integral, as reported in the below formula

$$T_C = \frac{2zJS(S+1)}{3k_B} \tag{1.12}$$

As we can understand there is a competition between the exchange energy and the thermal energy $k_B T$. When the temperature is lower than the Curie temperature the material is ferromagnetic, and exchange energy is higher than thermal energy, so magnetic spins are parallel each other. When the temperature is higher than T_C, the material becomes paramagnetic and thermal energy is higher than the exchange one. The magnetization behavior as a function of temperature for a ferromagnetic material is shown in figure 1.1

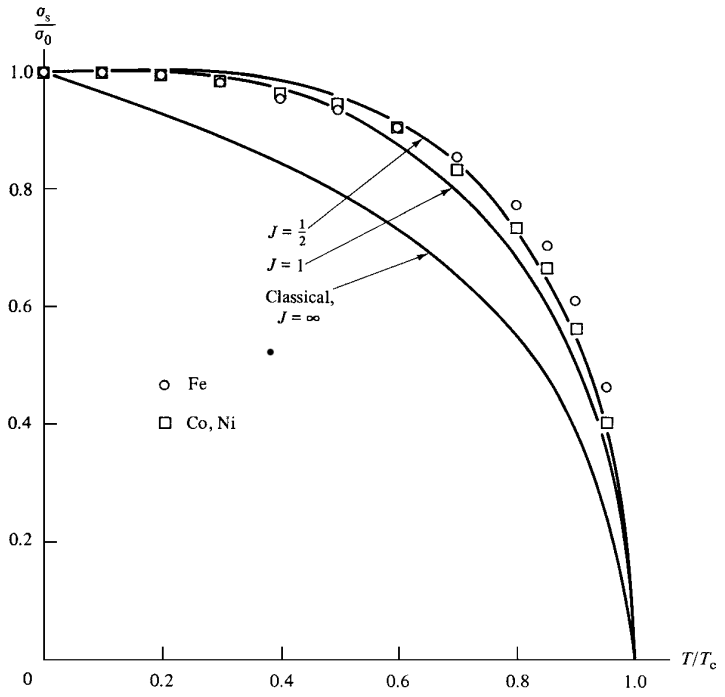

Figure 1.1: Magnetization as a function of temperature for a ferromagnetic material taking into account also the orbital part L, so that $\mu = g\mu_B J$ and $J = S + L$. After [2]

If we consider the spin vectors as classical, the energy becomes:

$$E_{exc} = -2JS^2 \sum_{i<j} cos\varphi_{ij} \tag{1.13}$$

Where φ_{ij} is the angle between the spin S_i and the spin S_j. For a cubic lattice with lattice

parameter equal to a and direction cosines α_1, α_2 and α_3 the formula 1.13 becomes

$$E_{ex} = costant + A_{ex}\left[(\nabla\alpha_1)^2 + (\nabla\alpha_2)^2 + (\nabla\alpha_3)^2\right] \tag{1.14}$$

and the exchange stiffness constant A_{ex} is defined as

$$A_{ex} = \frac{2JS^2c}{a} \tag{1.15}$$

c is a parameter equal to 1 for cubic structure, 2 for *bcc* and 4 for *fcc*.

In the above formula we supposed $J > 0$, i.e ferromagnetic material, while for antiferromagnetic material $J < 0$, in the latter case we can consider the lattice as the sum of two sublattices each being ferromagnetically ordered. In this second case we can define the Néel temperature as the temperature at which the material becomes paramagnetic. The ferrimagnetic material is an intermediate case between ferro- and antiferromagnetism. magnetic moments of the atoms on different sublattices are opposed, as in antiferromagnetism; however, in ferrimagnetic materials, the opposing moments are unequal and a spontaneous magnetization remains. Ferrimagnetic material are characterized by two important temperatures: the compensation temperature T_{comp} which is the temperature at which the magnetizations of two sublattices become equal in modulus and the Curie temperature as defined in the ferromagnetic case (figure 1.2).

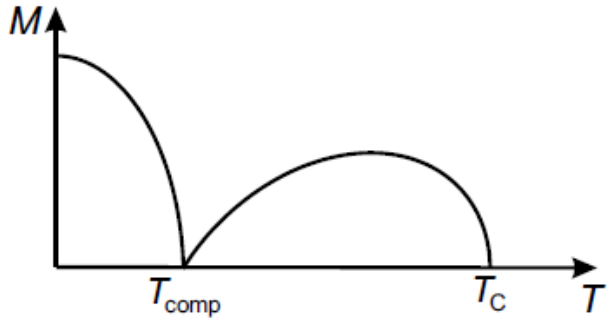

Figure 1.2: Schematic M(T) trend of a ferrimagnetic material [3]

1.1.3 Anisotropy energies

In the last sections we have discussed the energy as a function of the magnitude of the magnetization but we have neglected the energy dependence on the direction of M. In this section we will deal with that magnetic effects which depend on magnetization direction.

The most important anisotropy contributions are:

- Magnetocrystalline anisotropy
- Shape anisotropy
- Induced magnetic anisotropy
- Stress anisotropy
- Surface and interface anisotropy

In the following sections the main contributions are going to be described.

Magnetocrystalline Anisotropy

The experimental results show that a magnetization process can be anisotropic, and that the energy required to magnetize a ferromagnetic crystal depends on the direction of the magnetizing field with respect to the crystallographic axes. The existence of preferential magnetization directions can be described in terms of an energy contribution depending, for a given symmetry, on the orientation of the magnetization vector with respect to the symmetry axes. This is the *magnetocrystalline anisotropy* and its microscopic origin lies in the spin-orbit interaction, coupling the spin to the orbital motion of electrons.
The magnetization direction $\vec{m} = \frac{\vec{M}}{|M|}$ is given by the direction cosine $\vec{m} = (\alpha_1, \alpha_2, \alpha_3)$, with

$$\begin{aligned} \alpha_1 &= sin\theta cos\phi \\ \alpha_2 &= sin\theta sin\phi \\ \alpha_3 &= cos\theta \end{aligned} \tag{1.16}$$

Where θ and ϕ are shown in 1.3

$$\alpha_1^2 + \alpha_2^2 + \alpha_3^2 = 1 \tag{1.17}$$

The magnetocrystalline energy per unit volume e_{crys} can be written as a power series expansion of the components of magnetization:

$$e_{crys} = e_0 + \sum_i b_i \alpha_i + \sum_{ij} b_{ij} \alpha_i \alpha_j + \sum_{ijk} b_{ijk} \alpha_i \alpha_j \alpha_k + O(\alpha^4) \tag{1.18}$$

where e_0 b are constants for a particular material at a particular temperature and are expressed in J/m^3. There is no energy difference for oppositely magnetized systems. Therefore, the energy only depends on the alignment:

$$e(\vec{M}) = e(-\vec{M}) \tag{1.19}$$

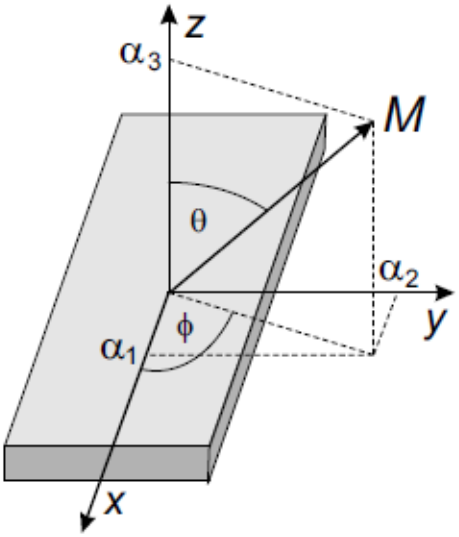

Figure 1.3: Definition of direction cosines. After [3]

that means

$$e(\alpha_i) = e(-\alpha_i) \tag{1.20}$$

For this reason there are no odd terms in the equation 1.21 and it can be written again as:

$$e_{crys} = e_0 + \sum_{ij} b_{ij}\alpha_i\alpha_j + \sum_{ijkl} b_{ijkl}\alpha_i\alpha_j\alpha_k\alpha_l \tag{1.21}$$

For a cubic system the magnetocrystalline energy can be written as

$$e_{crys} = K_0 + K_1(\alpha_1^2\alpha_2^2 + \alpha_1^2\alpha_3^2 + \alpha_2^2\alpha_3^2) + K_2\alpha_1^2\alpha_2^2\alpha_3^2 + \cdots \tag{1.22}$$

where K_i are coefficients called magnetocrystalline anisotropy constants which are functions of the b coefficients of equation 1.18. When K_2 is zero, the direction of easy magnetization is determined by the sign of K_1:

- $K_1 > 0$ the easy magnetization direction is [100] and the hard axis is [111] because $E_{100} < E_{110} < E_{111}$ as in bcc Fe (figure 1.4 and 1.5)
- $K_1 < 0$ the easy magnetization direction is [111] and the hard axis is [100] because $E_{111} < E_{110} < E_{100}$ as in fcc Ni (figure 1.4 and 1.5)

K_1 is negative for nickel and all the cubic ferrites that contain little or no cobalt. In general if K_2 is not zero, the easy direction depends on the values of both K_1 and K_2 [2].

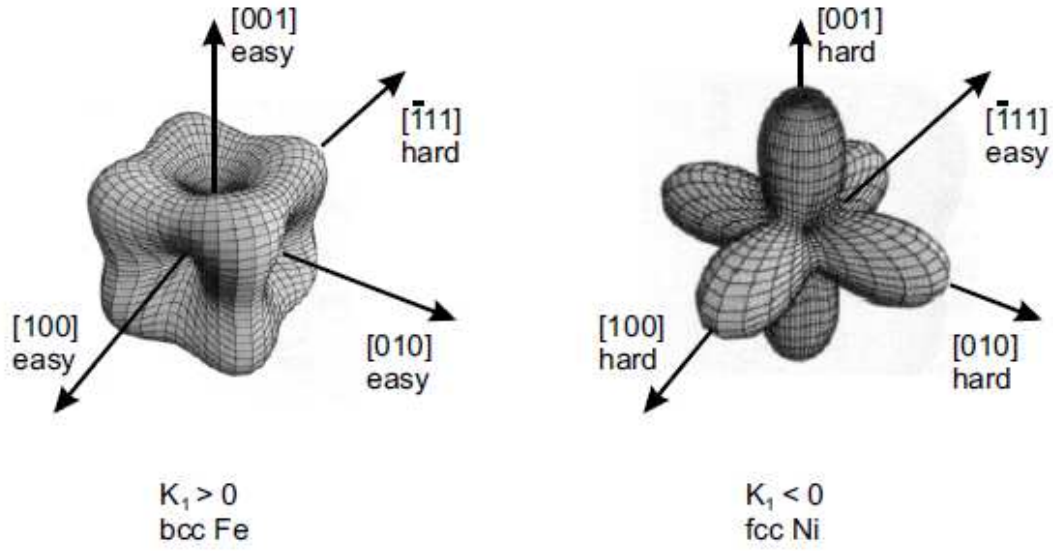

Figure 1.4: Left: Energy surface for cubic symmetry with $K_1 > 0$ (e.g. bcc Fe). Right: Energy surface for cubic symmetry with $K_1 < 0$ (e.g. fcc Ni). After[1]

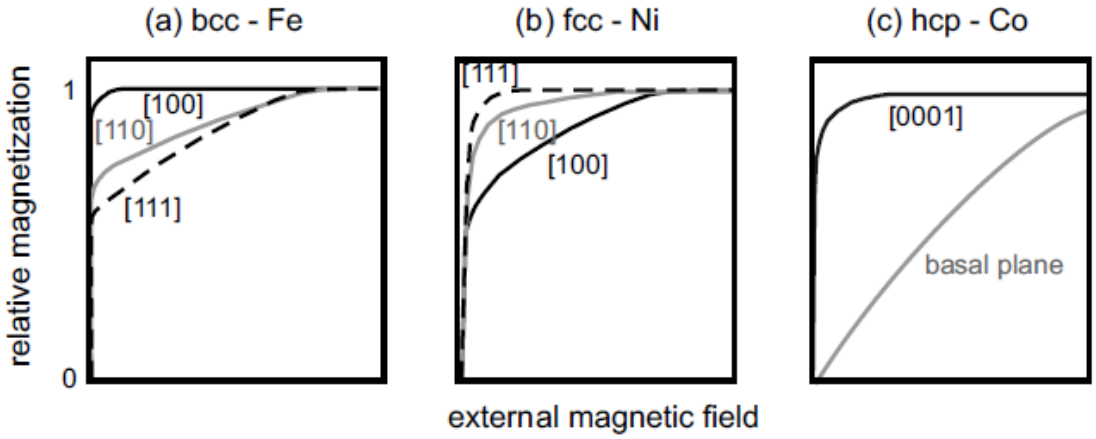

Figure 1.5: Magnetization curves along different crystallographic directions of (a) bcc-Fe, (b) fcc-Ni, and (c) hcp-Co. After[1]

For a uniaxial system with hexagonal symmetry like cobalt, it is convenient to use polar coordinate system and the anisotropy energy density is

$$e_{crys} = K_0 + K_1 sin^2\theta + K_2 sin^4\theta + \cdots \tag{1.23}$$

when $K_1 > 0$ the energy has two minima, one for $\theta = 0$ and the other for $\theta = \pi$ and the system shows an easy axis. While, for $K_1 < 0$ the material is easy plane since it has a plane of easy directions perpendicular to the c-axis. Another minimum condition exists, determined by the ratio between different anisotropy constant terms, under which the easy directions lie

on a cone with angle θ with respect to the c axis and it is called easy cone anisotropy.

Shape anisotropy

The magnetostatic energy is the contribution to the free energy that originates from the long-range dipolar interaction (equation 1.2) between magnetic moments and corresponds to the work required to build up a magnetic body by bringing its magnetic moments, from infinity to their position. With a different point of view, the same energy contribution can be expressed as the potential energy of the magnetized body in the field produced by the itself and it is due to macroscopic shape of sample. A confined sample, in fact, shows poles on its surfaces and these lead to a stray field outside the sample and a demagnetizing field inside.
If we consider the sample as an isotropic rotational ellipsoid (as in figure 1.6) then the demagnetizing field inside the sample becomes

$$\vec{H} = -N\vec{M} \tag{1.24}$$

N is the demagnetization tensor and the stray field energy becomes

$$E_{str} = 1/2\mu_0 \int \vec{M} N \vec{M} dV = 1/2V\mu_0 \vec{M} N \vec{M} \tag{1.25}$$

where V is the sample volume.

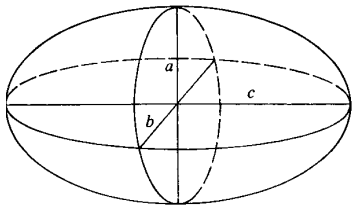

Figure 1.6: Isotropic rotational ellipsoid. After [3]

The tensor N is a diagonal tensor if the semiaxes a, b, and c of the ellipsoid represent the axes of the coordination system, the trace of N equals to 1

$$N = \begin{pmatrix} N_a & 0 & 0 \\ 0 & N_b & 0 \\ 0 & 0 & N_c \end{pmatrix} \tag{1.26}$$

In this system the stray energy (1.25) is

$$E_{str} = 1/2\mu_0 M^2 (N_a \alpha_a^2 + N_b \alpha_b^2 + N_c \alpha_c^2) \tag{1.27}$$

Where α_a, α_b, α_c are the direction cosines with respect to the ellipsoid axes. For a sphere $N_a = N_b = N_c = 1/3$ and the stray energy:

$$E_{str} = 1/2\mu_0 M^2 \cdot 1/3(\alpha_a^2 + \alpha_b^2 + \alpha_c^2) = 1/6\mu_0 M^2 \tag{1.28}$$

For an infinite thin plane $a = b = \infty$ so $N_a = N_b = 0$ and $N_c = 1$, in this case the energy becomes

$$E_{str} = 1/2\mu_0 M^2 cos^2\theta \tag{1.29}$$

θ represents the angle between the magnetization $\vec{M}$ and the z short axis.

Induced magnetic anisotropy

This kind of anisotropy is usually induced in soft magnetic material, that is for materials with low magnetocrystalline anisotropy.
An anisotropy direction can be induced by applying an external magnetic field during the heating of the sample. If the magnetocrystalline anisotropy is low enough, the external magnetic field rotates the magnetization at high temperature. The rapid thermal quenching gives rise to a freezing and an induced anisotropy is caused.
The energy of induced anisotropy per unit volume in an isotropic system can be expressed as

$$e_{ind} = -Kcos^2(\theta - \theta_{ann}) \tag{1.30}$$

where K is the induced anisotropy constant and $(\theta - \theta_{ann})$ is the angle between the magnetization during the measurement and the field direction during annealing.
Another way to induce magnetic anisotropy is the application of a plastic deformation.

Stress anisotropy

The magneto elastic interaction can be described as an interplay between magnetic characteristics and elastic deformation of crystal structure, this effect can be described through two phenomena: magnetostriction that occurs when a magnetic body subjected to a magnetic interaction, becomes spontaneously deformed; the inverse magnetostriction effect that consists in the magnetization alignment along a certain direction when the body is deformed by an external stress (Villari effect). The deformations influence the dipolar energy (form effect of magnetostriction), the exchange energy (volume magnetostriction) and the crystal anisotropy (magneto-elastic anisotropy induced in a strained system). We can expand all of

the energy terms with respect to the tensor of elastic distortion ϵ, the zeroth-order term corresponds to the undeformed lattice, the first-order to the magneto-elastic interaction energy and the second order to the elastic energy. The last term is generally considered independent of the magnetization direction. The expansion is usually stopped at the second term, only the linear elastic limit is considered and magnetoelastic coefficients are supposed to be strain-independent. The anisotropic magnetostrictive strain in the direction of magnetization can be written for an isotropic material by the relation

$$e = \lambda = \frac{3}{2}\lambda_S(cos^2\theta - \frac{1}{3}) \tag{1.31}$$

where $e = \Delta l/l$ is the strain measured at the angle θ relative to saturation magnetization direction and λ_S is the saturation magnetostriction coefficient. If λ_S, is positive, it is easier to magnetize the material in the tensile stress $\epsilon > 0$ direction and it is difficult to magnetize in the compressive direction $\epsilon < 0$, while if $\lambda < 0$ it is harder to magnetize a material in a direction for which $\epsilon > 0$ for which tensile stress is applied and easier to magnetize it in $\epsilon < 0$ compressive stress direction.

Magnetic surface and interface anisotropy

The surface is a very energetic part of the sample due to the broken symmetry. The spins of atoms at the surface are aligned perpendicular to the surface, and in this way they are not aligned to the field direction. In order to rotate them it is necessary to increase the magnetic field intensity. This phenomenon is similar to a local anisotropy. In all the sample this contribution is present but for bulk it is smaller than the other contributions due to volume.

The surface anisotropy intensity increases by lowing size, i.e. when the surface becomes comparable with volume, that is for thin films and nanoparticles.

If the surface anisotropy has an important role, the magnetocrystalline anisotropy constant K_{vol} can be replaced with an effective value:

$$K_{eff} = K_{vol} + K_S S/V \tag{1.32}$$

where K_S is the anisotropy of surface, S is the surface and V is the volume. In the case of a thin film the formula 1.32, after substituting $S/V = 1/d$ where d is the thickness, becomes:

$$K_{eff}^{film} = K_{vol} + 2K_s/d \tag{1.33}$$

the factor 2 is due to the double surface creation in a film (free surface and substrate interface). In a spherical nanoparticle the ratio is $\frac{S}{V} = \frac{4\pi r^2}{4/3\pi r^3} = \frac{3}{r}$, where r is the sphere radius, so the formula 1.32 becomes:

$$K_{eff}^{sphere} = K_{vol} + 3K_s/d \tag{1.34}$$

One very important effect due to interface and surface anisotropies is the *spin reorientation transition* occurring as a function of temperature. The classical example is the Co/Pd multilayer in which there is a dependence of the easy magnetization direction on the Co film thickness d. Considering an uniaxial system the energy is $E = K_1 sin^2\theta$ (see equation) and the easy direction lies in the film plane if $K_1 < 0$ that happens when the shape anisotropy that corresponds to $K_{vol} = K^V$ is higher than K_S, otherwise if the surface anisotropy is higher the direction is perpendicular to the film plane (figure 1.7).

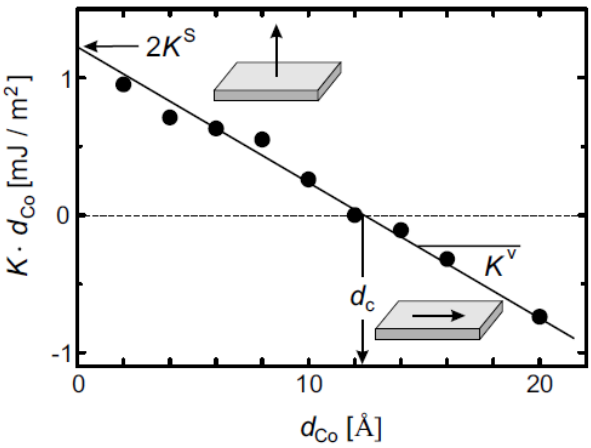

Figure 1.7: Magnetic anisotropy of Co/Pd films as a function of Co thickness. After [3]

As we can observe in figure 1.7 there is a critical transition thickness d_c between the two behaviors:

$$d_c = \frac{2\,|K_s|}{|K_{vol}|} \tag{1.35}$$

If:

$d < d_c$ perpendicular magnetization

$d > d_c$ in-plane magnetization.

1.2 Size effects on magnetic phenomenology

1.2.1 Magnetic domains

A ferromagnetic material is not always spontaneously magnetized, but shows a magnetization only when subjected to an external magnetic field. The absence of spontaneous magnetization was firstly attributed by Weiss to the formation of magnetic domains, that are regions inside the material magnetized in different directions, in this way the net magnetization is zero. The domains are created in order to reduce the magnetostatic energy, and to avoid the formation of magnetic charges on the sample surface.

Without an external field the magnetization vectors of different domains are not parallel in order to have a zero net magnetization and the zone between different domains is called domain wall.

The magnetization value inside the domain reaches the saturation value.

The magnetization process in an ideal crystal consists in a reversible domain wall movement that ends when all the domains are aligned and then the rotation of magnetization is reversible and around magnetic field direction, as shown in curves 1 and 2 in figure 1.8. The combination of the two processes is shown in curve 3 of figure 1.8.

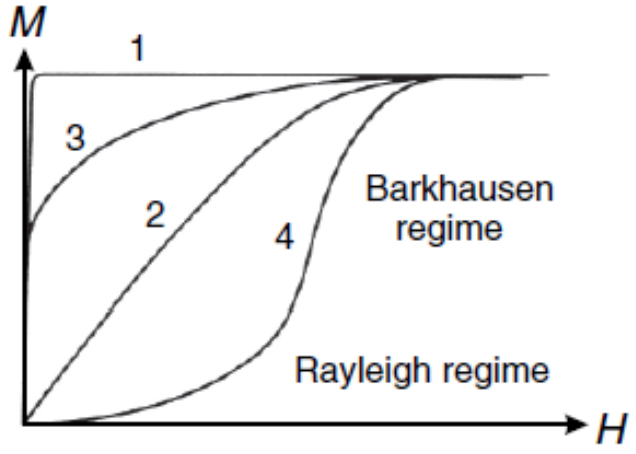

Figure 1.8: Curve 1: Wall movements in an ideal crystal. Curve 2: Rotation processes in an ideal crystal. Curve 3 : Combination of domain wall movements and rotation processes in an ideal crystal. Curve 4: Behavior of a real crystal. After [3]

In a real crystal two different behaviors exist: while at low magnetic field a reversible domain wall motion occurs (Reyleigh regime), at higher fields (Barkausen regime) there are

large jumps of domain walls due to pinning at crystallographic defects (curve 4 of figure 1.8). The fingerprints of this part of hysteresis loop are the jumps that can be observed directly in the hysteresis loop (figure 1.9).

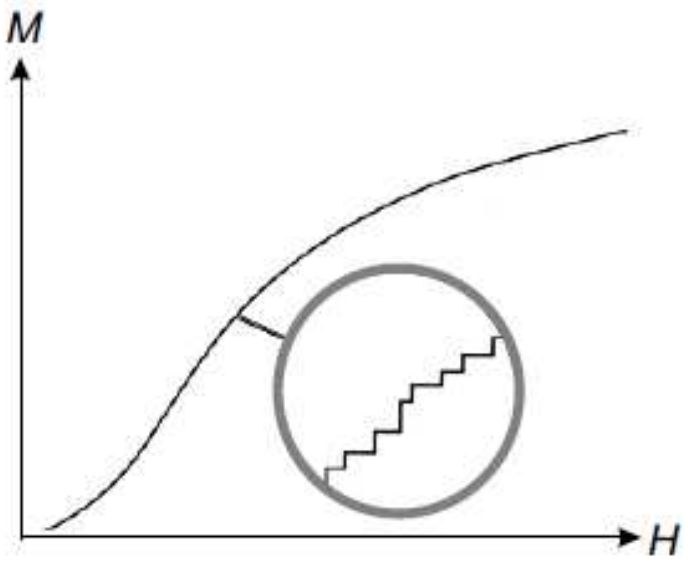

Figure 1.9: Barkausen jumps. After [3]

The domain walls are very important in order to understand the magnetic behavior of a material subject to a magnetic field. The domain walls can be classified based on the angle between the magnetization vectors in two neighboring domains with the wall as boundary:

- 180^0 wall: is the wall between two domains with opposite magnetization
- 90^0 wall: is the boundary between two domains with perpendicular magnetization

We can have the two kinds of walls depending on the crystallographic structure of the ferromagnet.
The fist group can be divided into two cases:

- Bloch wall: the magnetization rotation occurs in a plane parallel to the plane of the domain wall, as shown if figure 1.10
- Néel wall: the magnetization rotation occurs in a plane perpendicular to the plane of the domain wall, as show in figure 1.10

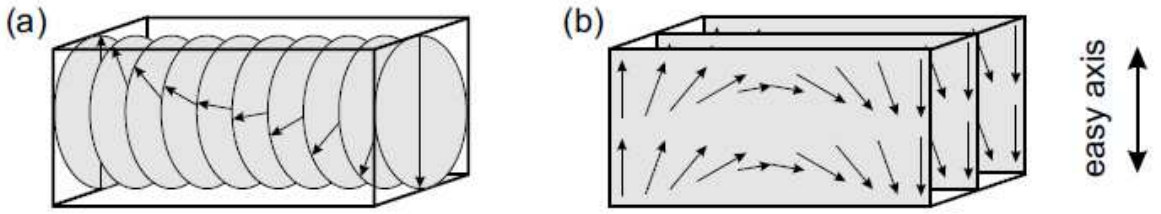

Figure 1.10: Different types of domain Walls: a) Bloch walls, b) Néel walls. After [3]

The Néel walls are dominating walls in thin films, while Bloch walls are dominating when increasing the film thickness. As an example, for iron, Néel walls are stable up to a critical thickness of 43 nm.

The width of the domain walls depends on the balance between different competing energy terms. The easiest case is the Bloch wall in a uniaxial crystal; if $\varphi = \pi/N$ is the average rotation angle between two spins separated by a lattice constant a, the domain wall energy due to exchange is:

$$E_{ex}^{BW} = JS^2 \frac{\pi^2}{Na^2} \tag{1.36}$$

As we can see in the equation 1.36, the exchange effect is to have infinite large walls. The other important term is the anisotropy energy, that for the easiest case of uniaxial crystal can be written for a single spin as: $E_{crys} = Ksin^2\varphi$ and in the Bloch wall becomes:

$$E_{crys}^{BW} = \frac{1}{2} aNK \tag{1.37}$$

The anisotropy energy favors wall with small thickness.
The total energy for the Bloch wall is given by the sum of the two terms in equations (1.36) and (1.37)

$$E^{BW} = JS^2 \frac{\pi^2}{Na^2} + \frac{1}{2} aNK \tag{1.38}$$

The domain wall width is given by the number of spins N that minimizes the energy:

$$N = \pi S \sqrt{\frac{2J}{a^3 K}} \tag{1.39}$$

We can isolate the constant

$$A = \frac{2JS^2}{a} \tag{1.40}$$

and then the width becomes

$$\delta = Na = \pi \sqrt{\frac{A}{K}} \tag{1.41}$$

In this way the free energy density for the wall becomes

$$\sigma = \pi\sqrt{AK} \tag{1.42}$$

In a three dimensional magnetic crystal the system tends to minimize the stray field energy and the domains pattern at the surface changes respect to bulk. These domains close the magnetic flux and they are called closure domains (figure 1.11).
The domains configuration changes with the symmetry of the magnetocrystalline anisotropy.

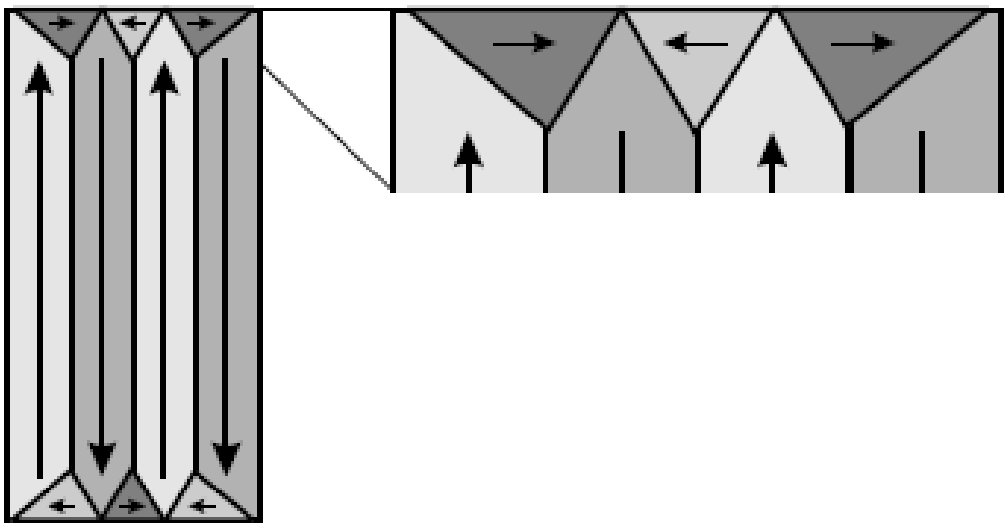

Figure 1.11: Closure domains exhibit a magnetization not parallel to the easy magnetization axis in order to reduce stray field energy. After [3]

1.2.2 Size reduction

If we reduce the size of a magnetic material, the formation of multi-domains is not yet possible, and, as first predicted by Frenkel and Dorfman, a critical size exists [4].
As a first approximation one can consider a spherical particle with diameter d, the domain can exist only if the diameter is higher than the domain wall dimension so if $d < \delta = \pi\sqrt{\frac{A}{K}}$ no domain wall can be present and so the nanoparticle is single domain .
We can take into account a more analytical method which considers the energy needed to create a domain wall in a spherical nanoparticle smaller than the magnetostatic energy of a sphere with two domains separated by a Bloch wall, $\sigma_{DW}\pi r^2 = 4\pi r^2\sqrt{AK}$ in comparison with the magnetostatic energy $E_{MS} = \frac{4}{9}\mu_0 M^2\pi r^3$. The critical radius above which the formation

of multidomain structure is possible is given by [5]:

$$r_c = 9\frac{\sqrt{AK}}{\mu_0 M_S^2} \tag{1.43}$$

The above model is a good approximation if we take into account that the domain wall in low dimension is the same as in bulk system, but this is a good approximation only if the anisotropy is strong enough to maintain the magnetization along the easy axis and surface effects are negligible.

If the anisotropy is low, then we can not consider the above model and we have to consider that the magnetization twist increases the exchange energy. If this exchange energy density cost is equated to the magnetostatic energy density for a uniformly magnetized sphere then we can obtain the critical radius, that is

$$r_c = \sqrt{\frac{9A}{\mu_0 M_S^2}\left[ln\left(\frac{2r_c}{a} - 1\right)\right]} \tag{1.44}$$

where a is the lattice constant, M_S is the saturation magnetization, A is the stiffness constant. The critical radius for low and high anisotropies can be seen in figure 1.12.

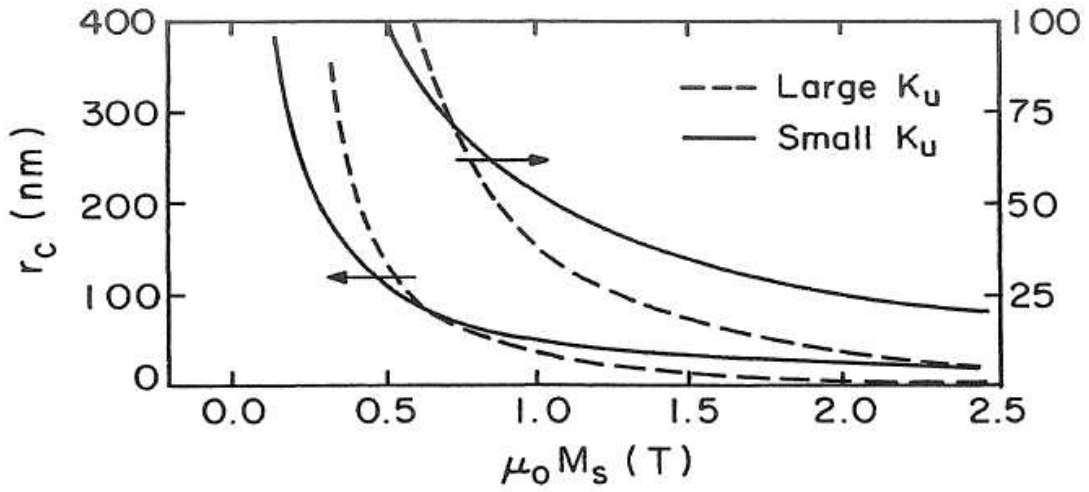

Figure 1.12: Critical radius for two different anisotropies (after [5])

For an exact value of critical radius we have to minimize the complete magnetic energy, but the above simple models are useful to have an order of magnitude.

1.2.3 Stoner-Wohlfarth model

The StonerWohlfarth model is a simple and widely used model for describing the magnetization process of a single-domain particle [6]. The magnetization vector can only rotate in a coherent

way when an external magnetic field is applied. The particle is assumed to have a uniaxial magnetic anisotropy with anisotropy parameter K. It is assumed that the particles are uniaxial and ellipsoidal in shape. The total energy for the prolate spheroid can be written as:

$$E = -Kcos^2(\theta - \theta_0) - \mu_0 H M_S cos\theta_0 \tag{1.45}$$

where θ_0 is the angle between the easy axis and the applied field direction, θ is the angle between M and H as shown in the figure 1.13, M_S is the magnetization of single domain particle and H is the external magnetic field.

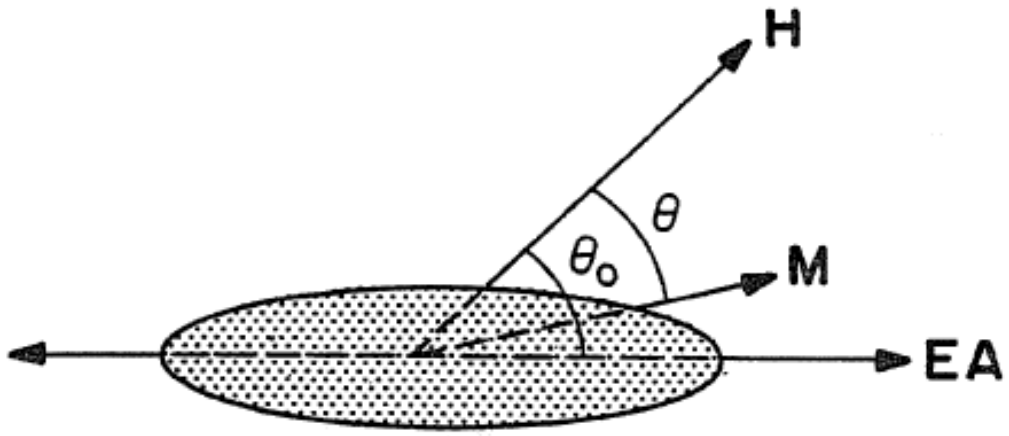

Figure 1.13: Coordinate system for magnetization reversal process in single-domain particle (after [5])

The anisotropy constant can be written as $K = \mu_0 \left[H_A + (N_c - N_a)M_S\right] M_S/2$ where H_A is the easy axis anisotropy term and N_c and N_a are the demagnetization factors perpendicular and parallel to the easy axis (see figure 1.6).
The energy can be minimized as a dependence of θ and the result becomes

$$2Ksin(\theta - \theta_0)cos(\theta - \theta_0) + \mu_0 H M_S sin\theta = 0 \tag{1.46}$$

using $K = \mu_0 H_A M_S/2$ and $h = H/H_A$ then the above equation

$$sin2[(\theta - \theta_0)] + 2hsin\theta = 0 \tag{1.47}$$

and if $m = M/M_S = cos(\theta)$ the solution can be written as:

$$2m(1-m^2)^{1/2}cos(2\theta_0) + 2sen(2\theta_0)(1-2m^2) \pm 2h(1-m^2)^{1/2} = 0 \tag{1.48}$$

The results of the equation 1.48 are shown in figure 1.14

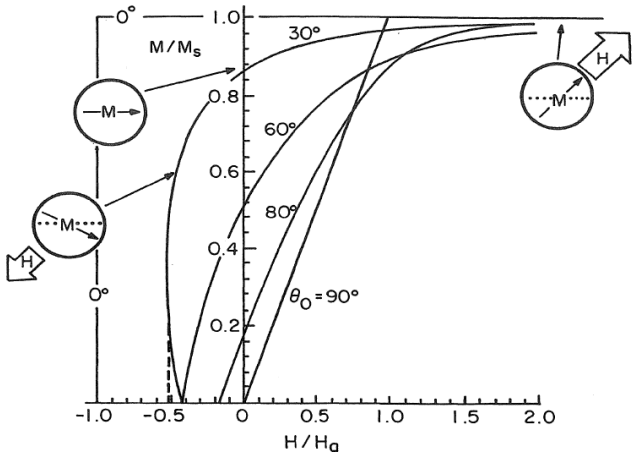

Figure 1.14: Stoner-Wohlfarth solutions (after [5])

The important cases are:

If $\theta_0 = \frac{\pi}{2}$ we have a linear behavior, because we just have a rotation of M in H direction and no coercivity is present.

If $\theta_0 = 0$ we have a square loop.

In the intermediate cases the magnetic field works against the torque due to $\frac{dE}{d\theta}$. The saturation is reached if the magnitude of the external field exceeds the switching field. If the external field is applied towards an arbitrary direction to the easy axis the magnetization is partly reversible and partly irreversible. The important hypothesis of this model is that the magnetization can only rotate with a coherent mode but the magnetization can also rotate inside the nanoparticle as in curling and buckling mode (figure 1.15) [5]. Nanoparticles can, in general, be interacting and the right way to analyze their behavior is the application of the micromagnetic models in which we can take into account all the different contributions.

Depending on nanoparticles interdistances in the assembly, the interparticles interactions can give rise to complex behavior as I will show in the next sections.

1.2.4 Superparamagnetic behavior

If the size of nanoparticle is reduced and the magnetic anisotropy energy becomes comparable with thermal energy k_BT then the thermal excitation causes continual changes in the orienta-

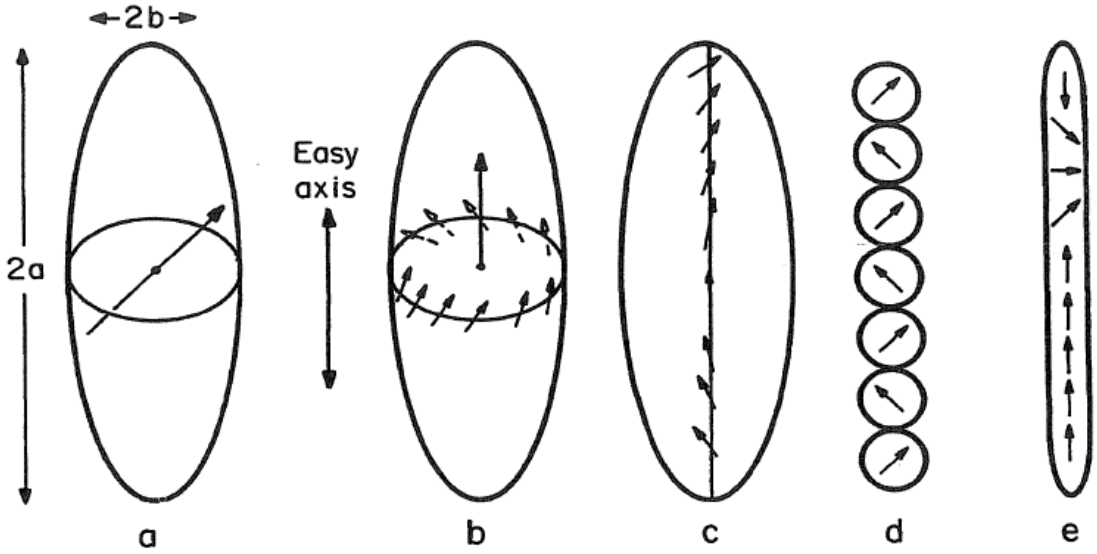

Figure 1.15: (a) coherent rotation; (b) curling; (c) buckling; (d) fanning (in chain of spheres); and (e) domino effect. After [5]

tion of the magnetization for each individual particle which is schematically depicted in figure 1.16.

Let us consider an assembly of uniaxial single domain nanoparticles each with an anisotropy energy barrier $\Delta E_B = KV$ that separates two minima at $\theta = 0$ and at $\theta = 180$, as shown in figure 1.16

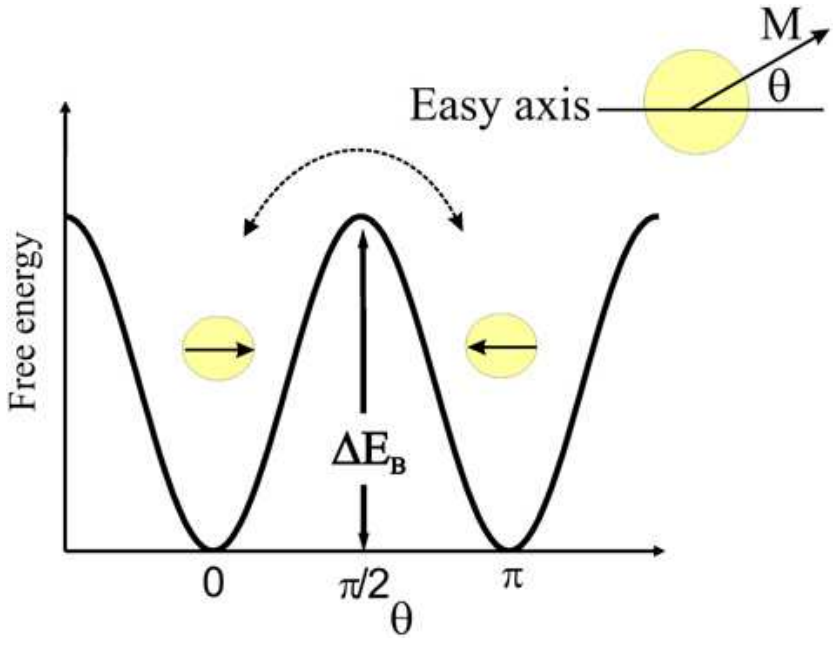

Figure 1.16: Two energy minima for a superparamagnetic nanoparticle. After [7]

If the kinetic energy $E_C = K_B T$ is higher than the barrier, then the magnetization oscillates between the two minima and, in absence of magnetic field no magnetization is still present: this is the superparamagnetic behavior. On the contrary, if anisotropy energy is higher than the kinetic term, the magnetization lies along the easy axis: this is the blocked or ferromagnetic state.
In particular if we are in the case $K_B T > KV$ the magnetization rotates between the two minima with a frequency f which is related to $\tau = (2\pi f)^{-1}$ (the Néel-Brown relaxation) [8, 9]

$$\tau = \tau_0 exp(KV/k_B T) \tag{1.49}$$

where $\tau_0 \approx 10^{-10}$ is the inverse attempt frequency. The equation 1.49 indicates that the superparamagnetic behavior also shows a time dependence. The system is in superparamagnetic state if the measurement time τ_m is lower than τ, for the given set-up; when τ becomes comparable with τ_m then the system is in the ferromagnetic state.
In a temperature dependent experiment, the so called *blocked case* is when $T < T_B$, where the blocking temperature T_B can be obtained from 1.49

$$T_B = \frac{KV}{K_B} ln \frac{\tau_m}{\tau_0} \tag{1.50}$$

Above the transition temperature the magnetic behavior is superparamagnetic.
There are different ways to find the blocking temperature and to understand if the nanoparticles are in the superparamagnetic state at room temperature. One of the most used experiment couples the Zero Field Cooling and Field Cooling measurements: at the beginning the sample is cooled at minimum temperature without an external applied field, then a small field is applied and the magnetization is measured while heating the sample. After this, the sample is cooled down to the minimum temperature with the same field and the magnetization is measured during the heating.
During the Zero Field Cooling the effect is to freeze a random spins configuration: when we apply the field at low temperature the spins have not enough energy to rotate along the field direction, but increasing the temperature the thermal energy increases and anisotropy decreases so the spins start rotating. So we have an increase of magnetization in the field direction, up to the average blocking temperature of the system. Above the blocking temperature the kinetic energy becomes higher than the magnetic energy and the effect is the lowing

of the magnetization.

During the Field Cooling instead the effect is to freeze an oriented spins configuration, and during the increasing of the temperature there is a decrease of the magnetization. The temperature at which the magnetization starts to decrease is the minimum blocking temperature of the nanoparticles assembly and the temperature at which the FC and ZFC curves coincide is the maximum blocking temperature. A characteristic ZFC-FC measurement is shown in figure 1.17

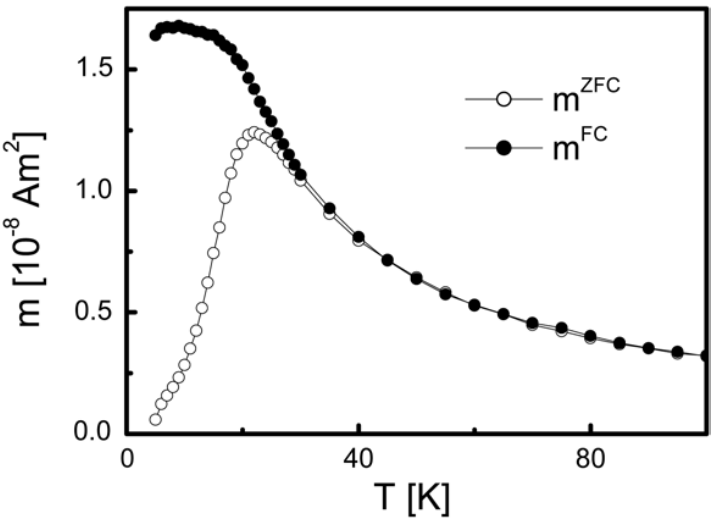

Figure 1.17: Characteristic ZFC-FC measurement of a granular (discontinuous) metalinsulator multilayer systems $Co_{80}Fe_{20}$(tn = 0.5 nm)/Al_2O_3(3 nm) after [7]

In order to define a magnetic system as superparamagnet at room temperature two requirements have to be satisfied. The first is that above a blocking temperature, lower than room temperature, the system does not show magnetic hysteresis. The second requirement is that the magnetization loop has to be temperature dependent, and the curves taken at different temperatures can be superimposed when plotted as a function of H/T.

Similarly to the paramagnetic behavior, the magnetization curve of a superparamagnet can be described by Langevin curve:

$$m = L(x) = coth(x) - 1/x \tag{1.51}$$

where $x = \mu_0 mH/k_B T$.

1.3 Magnetic nanoparticles assemblies

1.3.1 Interaction between magnetic nanoparticles

In nanoparticles systems, different kinds of magnetic interparticle interactions exist and they change with the volume concentration [7] . The magnetic nanoparticles are considered as two magnetic dipoles $\vec{m}_1$ $\vec{m}_2$ at a distance r so the equation 1.2 becomes [10]

$$E = \frac{\mu_0}{4\pi r^3}\left[\vec{m}_1 \cdot \vec{m}_2 - \frac{3}{r^2}(\vec{m}_1 \cdot \vec{r})(\vec{m}_2 \cdot \vec{r})\right] \tag{1.52}$$

The strength of the moments interaction depends on their separation and degree of alignment. Another important interaction is the exchange interaction. If the nanoparticle in the assembly are very close to each other, the exchange interactions play an important role due to the surface spins. If nanoparticles are dispersed in an insulating matrix, superexchange interaction can occur via intermediate atoms or ions. If the nanoparticles are instead in a metal matrix the RKKY interactions are present [5].

The interactions between nanoparticles have different effects on magnetic characteristics of hysteresis loop and on blocking temperature in dependence on the kind of interaction. Their effect is to modify the energy barrier $\Delta E = KV$ because in presence of interactions the reversal of the single particle moment may change all energy barriers in the assembly. For low concentration the interparticle interactions are negligible while for high concentration they can dominate over single particle blocking giving rise to a collective freezing.

Two different kinds of collective states can be identified: the *superspin glass* (SSG) and the *superferromagnetism* (SFM) states. We can have one behavior or the other in dependence on the intensity of interaction strength. In the lower density case the moments of nanoparticles freeze collectively into a spin glass phase below a critical temperature, Tg. If the nanoparticles density increases, so thus the interaction between the particles: a different collective state appears called superferromagnet. In real systems the occurrence of particle sizes distribution and inhomogeneity of magnetic moments, can give origin to a complex behavior.

Superspin glass

The most important characteristics necessary to have a spin glass system are frustration and randomness.

The classical example of magnetic frustration is the triangular lattice with an antiferromagnetic coupling (as shown in figure 1.18) in which there is a geometrical frustration.

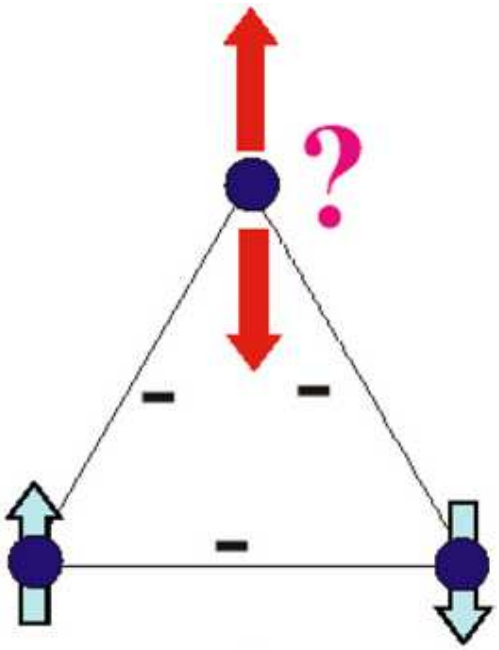

Figure 1.18: Triangular frustrate lattice of spins. After [7]

If nanoparticles have a ferrimagnetic behavior and they are close to each other, a cooperative freezing of magnetic moment can be present below a well-defined temperature Tg (the glass temperature). At high temperatures the behavior is dominated by thermal fluctuations, when the system is cooled to lower temperatures, the independent moments form locally correlated units, denoted as clusters, droplets or domains. When the temperature is lower than Tg the fluctuations in the clusters also progressively slow down. The spin glass ground state is chaotic because the system can jump between equivalent metastable states. In order to observe this behavior the most used method is the ZFC-FC measurement: in FC we can see a minimum at low temperature and a peak in the ZFC that corresponds to the freezing temperature T_f of sample [11, 12]. Another technique used for characterized the system is the susceptibility measurement, and the pick of the real part can be fitted as:

$$\tau = \tau^* \left(\frac{T_m}{T_g - 1} \right)^{-zv} \tag{1.53}$$

where $\tau = (2\pi f)^{-1}$, τ^* is the relaxation time of individual particle moment, Tg is the static spin glass temperature and zv is a dynamic critical exponent [13, 14].

The difference between this behavior and the relaxation due to Néel (equation 1.49) is evident, in fact in the spin glass case the sample shows a broad peak in the ac susceptibility

reflecting a wide distribution of anisotropy energies.

Superferromagnetism

When the interparticles interactions become stronger and stronger the system approaches to a kind of ferromagnetic domain state that is called superferromagnetic state [15]. In this state the atomic moments are replaced by the supermoments of the individual nanoparticles. But this SFM domain state has hardly been shown in nanoparticle systems. In Figure 1.19 we can see the transition from paramagnetic to superparamagnetic and finally to the ordered SFM state.

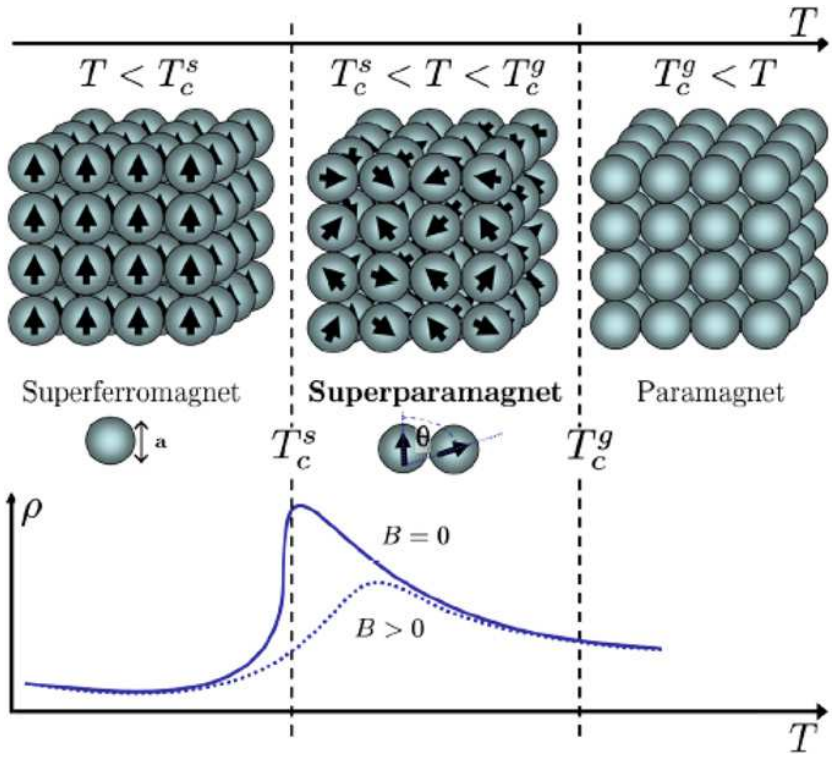

Figure 1.19: Nanoparticles array and passage from superferromagnet to superparamagnet to paramagnet behavior (after [16])

It is very difficult to understand the experimentally observed SFM state, because the preponderant interaction is of dipolar origin, that does not lead to a FM ground state because it is non-uniform in the directional dependence and only in rare cases this behavior is awaited. The first solution of this dilemma was proposed by Kretschmer and Binder, who tried to calculate the ground state of ferroelectrics on a purely dipolar basis but they never obtained a ferroelectric ground states. The SFM systems must be consider as an exchange that has its origin

in a tunnelling superexchange. In order to characterize this state different measurements can be done:dynamic hysteresis loops, Cole Cole diagram, polarized neutrons, aging and memory effects [7].

1.3.2 Surface effects in ferrimagnetic nanoparticles

An assembly of ferrimagnetic fine particles usually shows the features of glassy system [17]. This glassy behavior results from the interplay between finite-size effect and surface anisotropy. In particular the glassy behavior is due to the spin disorder at nanoparticle surface. The fingerprint is the presence of a flattening of the field-cooling susceptibility, the existence of high field irreversibility in the magnetization curves and between ZFC and FC susceptibility, the presence of a shifted loop after FC, the increase in the magnetic viscosity, the occurrence of aging phenomena and the rapid increase of non-linear susceptibility when the blocking temperature is approached from above. Surface effects dominate the magnetic behavior of nanoparticles for size smaller than 2 nm, in fact in this case most of the magnetic spins are located at the surface and the ideal picture of superspin (as described in the superparamagnetic theory) is no more valid. The broken bonds and the defects at the surface layer give rise to frustration if the magnetic interactions strength is strong enough. The surface layer spins are not oriented parallel to each other and the profile of magnetization is not uniform inside the magnetic nanoparticle; the first models describes the surface of the nanoparticle as a dead layer that gives no contributions to the total magnetization. The origin of spin misalignment is still under discussion. Coey [18] highlighted that this behavior is due to the frustration and a complete study was done in this direction. The glassy state of the surface at low temperature $T < T_g$ gives origin to an exchange field acting over the ordered core spins wich could be responsible of the shifting of the hysteresis loop after field cooling, similarly to an exchange-bias. The existence of a frozen state at the particle surface has been shown by different techniques [17]. A micro-magnetic model at atomic scale was proposed by Kodoma and Berkowitz [19], and different magnetic simulations have been done.

In samples with high concentration of nanoparticles with a random distribution of easy axis, the interactions are a supplementary source of magnetic frustration, as already shown. The interplay between the two sources of frustration determinate the state of the system. If the dipolar interactions between nanoparticles are strong, the individual energy barriers coming from intrisic anisotropy of singular nanopartcle can no longer be considered and the energy of

the assembly is the only relevant one. The occurrence of aging phenomena is a clear indication of strong interactions.

One-particle model and surface effect

This simple model is useful to understand the role of surface in nanoparticles [17]. It considers maghemite nanoparticles, even if it can be applied also to other ferrimagnetic nanoparticles. Maghemite has a fcc structure and the spins interact via antiferromagnetic coupling. The Hamiltonian can be written as

$$H/k_B = -\sum_{\alpha,\beta=T,O}\sum_{i,n=1} J_\beta S_i^\alpha S_{i+1}^\beta - h\sum_{\alpha=T}\sum_{i=1}^{N_\alpha} S_i^\alpha \tag{1.54}$$

where $h = \frac{\mu H}{K_B}$ with S and μ the spin value and magnetic moment of Fe^{3+} ion, and consider the Ising model $S_i^\alpha = \pm 1$. We consider a system with a sphere shape, a diameter D and free boundary conditions, in this way we distinguish two regions: the surface formed by the outermost unit cells, and a core formed by a sphere of spins with diameter D_{core}. The different measured magnetization of uncompensated spins is $M_{Unc} = (N_O - N_T)/N_{Total}$ of O octahedral and T tetrahedral sublattices in respect to total spins. In general the total magnetization at a given temperature M_{Total} follows a quasi-linear behavior with $1/D$ indicating that the reduction is proportional to the ratio of surface-to-core spins. This behavior can be simply explained taking into account a surface layer with thickness Δr independent of D. So the dependence of M can be expressed as

$$M(D) = M_{Core} - \Delta M\frac{\Delta r S}{V} = M_{Core} - \Delta M\frac{6\Delta r}{V} \tag{1.55}$$

From the above theory the total magnetization for small particles is completely dominated by surface contributions, and for this reason the ferrimagnetic order is not perfect.
At low temperature the hysteresis loop shape changes in dependence on the surface thickness, in fact, the core has a perfect Stoner-Wohlfarth behavior that in hard direction is perfectly squared loop independent on particle size (figure 1.20), while the presence of surface gives origin to a reversal behavior.

The reversal of surface spins triggers the core spins and the loop has a step-like behavior. The hysteresis loop shape changes with temperatures and with particles size.
In real maghemite samples, the disorder and imperfections cause a distortion of atoms in the spins lattice more evident at the surface. This lattice presents one sixth of randomly

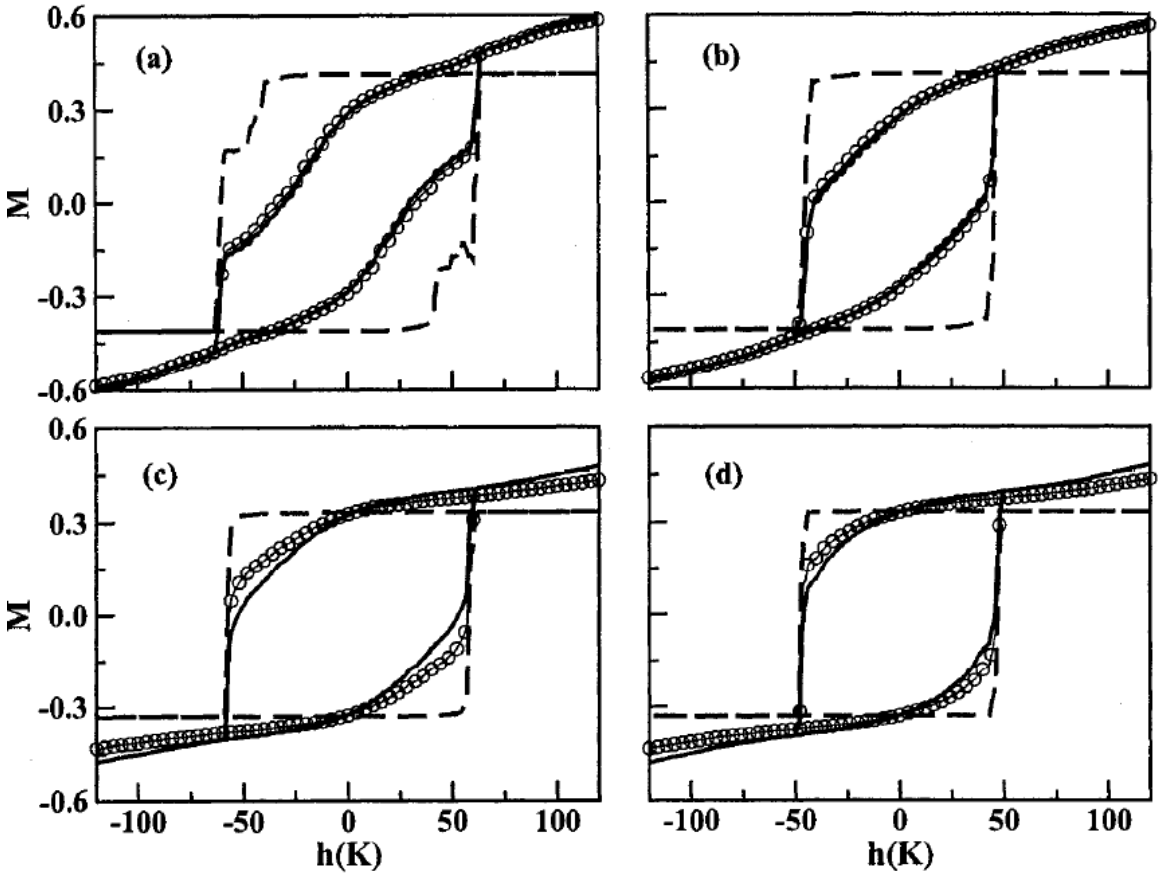

Figure 1.20: Surface, core and total contributes for a) D=3 nm T=20K, b) D=6 nm T=10 K, c) D=6 nm, T=20K from [17]

distributed vacancies on the O sublattice sites and in order to study the effect of disorder we can take these vacancies as if they were randomly distributed. At the surface, for example, we can consider the unit cells with an higher concentration of vacancies, so the coordination of atoms is lower than in the bulk. At high field the M_{core} is higher than the $M_{surface}$ and this difference increases by increasing the defects because the ferrimagnetic order is lower and spins are not aligned to each other. The vacancies act as nucleation center for ferromagnetic domains at surface and an increased coercive field can be observed.

1.4 Exchange bias effect

One very common effect that can be shown in low dimension systems is the exchange bias, and in particular it is shown when a ferromagnetic/ferrimagnetic (FM) thin layer is in contact with an antiferromagnetic (AFM) thin layer. It was observed for the first time in Co fine particles

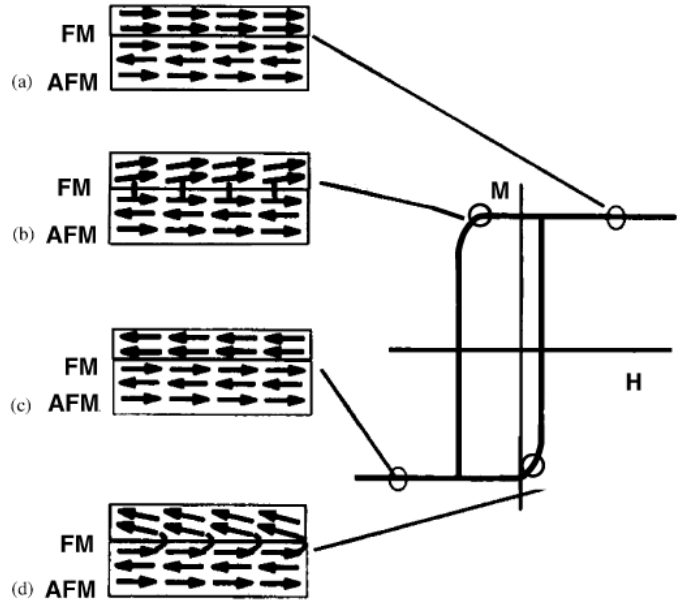

Figure 1.21: Exchange bias effect scheme on an AFM material with high magnetic anisotropy. After [24]

[20]. In the last decades there has been some research in exchange bias in nanoparticles and in thin film systems because of the possibility of an control the FM/AFM presence. In fine particles and in nanoparticles the effect of oxidation, nitration or sulfation of surface can give rise to an antiferromagnetic state and exchange bias effect can be shown. The fingerprint of exchange bias is the shift of magnetic hysteresis loop along the magnetic field axis, after field cooling from above the Néel temperature, T_N, of the AFM and below the Curie temperature T_C, of the ferromagnet. Other important features are an increase of the coercivity, H_C, below T_N after a field cooling procedure and in nanoparticles the unidirectional anisotropy. The physical origin of exchange bias is rather generally due to the coupling between an AFM and FM components at the interface, but the microscopic way in which this coupling translates into exchange bias is more controversial and many models have been proposed to explain it [21, 22, 23]. The exchange bias phenomena can be described as the alignment of the AFM spins parallel to the FM spins occurring at the FM/AFM interface during the field cooling procedure (as shown in figure 1.21).

Indeed the external magnetic field force has to overcome the coupling force between the AFM and FM spins at the interface that exerts an additional torque on the FM spins. Two different opposite limiting cases can be identified, depending on the strength of the AFM mag-

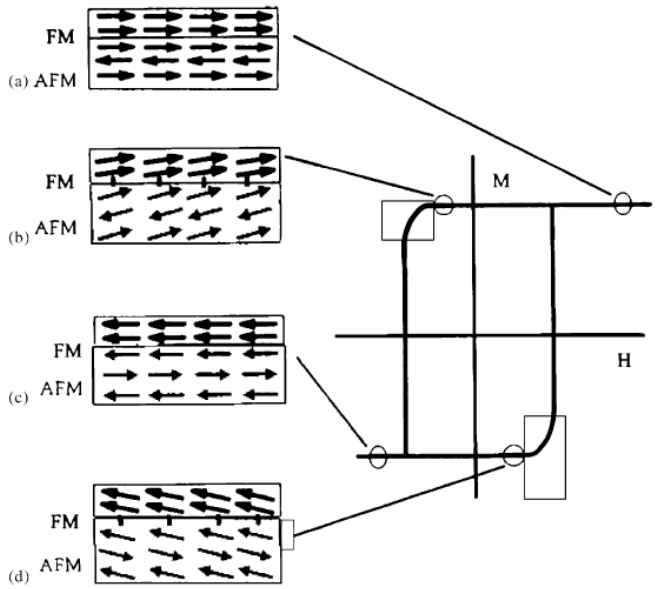

Figure 1.22: Exchange bias effect scheme on an AFM material with low magnetic anisotropy. After [24]

netic anisotropy: if the AFM anisotropy is large, a shift of the hysteresis loop can be observed, while for small AFM anisotropy, the only observed effect should be a coercivity enhancement (without any loop shift). In general, both the effects can be observed simultaneously. If a large magnetic field is applied at a temperature T so that $T_N < T < T_C$, all the spins in the FM will align parallel to H, while the spins in the AFM will remain random. If the sample is cooled down to T_N with the applied field, the first layer of spins in the AFM will tend to align parallel to the spins in the FM, and the other spins in the AFM will orient antiparallel to each other. In figure 1.21 we can see the different stages of an hysteresis loop if the external magnetic field is applied during the cooling. After the field cooling, the spins in both the FM and the AFM lie parallel to each other at the interface, and if a magnetic field is reversed, the spins in the FM rotate, while, if the AFM anisotropy is sufficiently high, the spins in the AFM will remain fixed and they will exert a microscopic torque to the spins in the FM. The magnetic field required to reverse the magnetization in the FM musts be higher than in the case of FM without AFM, in this way the coercive field in the negative field branch increases. If the magnetic field is reversed back to positive values, the rotation of spins in the FM will be easy because the torque due to AFM will favor it and the coercive field in the positive field branch will be reduced. The effect will be a shift of the hysteresis loop along the magnetic field axis.

In the case of low AFM anisotropy the hysteresis loop changes as shown in figure 1.22 and no shift is observed. After the field cooling, the spins in both layers are aligned in the same direction and when the magnetic field is reversed the spins in the FM rotate, so as the spins in the AFM, the AFM structure translates into an enhanced coercivity. the same behavior is shown for the reversal at positive field values and no loop shift is observed.

1.5 Amorphous magnetic thin films

If we reduce instead of all the three dimensions only the thickness we obtain thin films. In this thesis I have studied amorphous thin films that are very interesting physical systems because of the presence of possibility of tune the magnetic anisotropy.
The structure of the amorphous alloy is not completely random, but the atoms are disposed in a short-range order structure similar to liquid state. and the absence of crystalline order coincides with the absence of long-range order and, no magnetocrystalline anisotropy is present. For the above reasons magnetic amorphous alloys are very soft magnetic materials.
The only sources of anisotropy are magnetoelastic, shape and thermomagnetic ones.
There are many different compositions of these materials and their magnetic characteristics change by changing the type of metalloid elements and their content.

1.5.1 Random anisotropy

In the absence of an induced anisotropy the local moments tend to follow the local easy axis that usually is determined by internal stress. The domain walls are wide and the defects are localized, because the structural inhomogeneities have a scale less than 2 or 3 nm and for that there is small pinning of domain walls on defects. For these reasons the permeability can be very large and coercivity can be very low.
The main advantage could be their use in high frequencies applications, in fact, the atomic disorder of amorphous alloys increases the electrical resistivity that means low eddy currents so low high frequencies loss.
The most commonly used model for describing the above magnetic characteristics is the Random Anisotropy [25, 26] , in which we consider the local order as similar to a local crystal-field, which orientation and strength changes with position. The local crystal field energy can be written by a uniaxial anisotropy term, K_{loc}, which fluctuates with a correlation length l, that depends on the local atoms arrangement. The local magnetic moments are coupled with an

exchange interaction that is $A\left[\nabla\vec{m}(r)\right]^2$, these two terms appear in the magnetic energy:

$$E = A\left[\nabla\vec{m}(r)\right]^2 - K_{loc}\left\{\left[\vec{m}(\vec{r})\cdot\vec{n}(\vec{r})\right]^2 - \frac{1}{3}\right\} \tag{1.56}$$

where $\vec{n}$ is the random unit vector that represents the K_{loc} orientation, $\vec{m}(r)$ is the local reduced magnetization.

The orientational correlation length L of the local magnetic moments is another important parameter. The first term of equation 1.56 scales with A/L^2, while the macroscopic anisotropy can be expressed as $K_{loc}(l/L)^{\frac{3}{2}}$. L can be obtained by minimizing equation (1.56)

$$L = \frac{16A^2}{9K_{loc}^2 l^3} \approx \frac{10^4}{K_{loc}^2} \tag{1.57}$$

For 3d elements $K_{loc} = 5\cdot 10^4 J/m^3$ and L becomes $20\mu m$ [5]. If $L >> l$, the effective macroscopic anisotropy is small and the material has soft magnetic properties while if $L \approx l$, the magnetization is preferentially and more strongly oriented in the direction of the local anisotropy and an harder behavior is obtained.

1.5.2 Induced anisotropy in amorphous films

As already shown in the previous sections, it is possible to induce a long range order in an amorphous alloy by field annealing or stress application. The amorphous alloy is heated at a temperature high enough to allow atomic mobility, but below the crystallization temperature. If during heating a magnetic field is applied the local atomic rearrangements result in a long-range correlation with the magnetization direction. When the sample is cooled the magnetization tends to orient in the same direction it had during the annealing. The metalloids, usually present in the alloys, have an high mobility and strong chemical interaction with the magnetic metals and favor magnetization in a specific direction. Uniaxial magnetic anisotropy, as already shown, can be also induced by stress, e.g. in amorphous thin films a stress due to the growth on a substrate.

1.5.3 Weak stripe domains and transcritical loop

The fingerprints of the presence of a perpendicular anisotropy, due to stress presence, are the appearance of stripe domains [27] and a characteristic hysteresis loop called transcritical [28]. The weak stripe domains theory is valid in the case of low uniaxial anisotropy $Q = \frac{K_u}{K_d} < 1$ where K_u is the induced uniaxial anisotropy constant and K_d is the stray anisotropy field constant. Beyond a critical thickness the magnetization starts to oscillate out of the plane

in order to save the anisotropy energy (see figure 1.23), while at the critical thickness the amplitude of the magnetization oscillation goes to zero. Their half period equals the film thickness. The critical thickness is defined as:

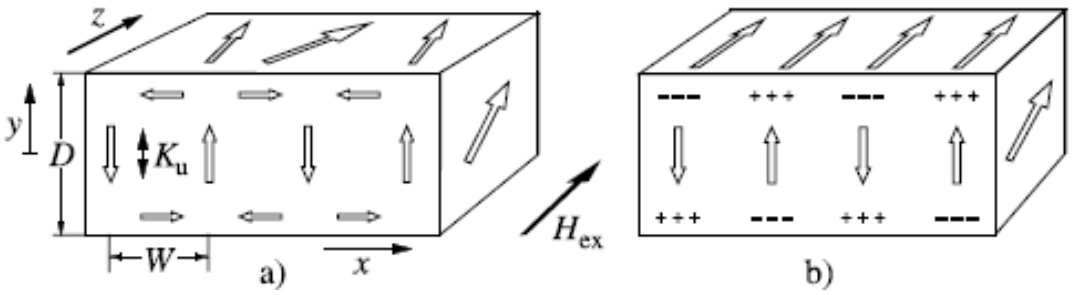

Figure 1.23: a) stripe domains in soft magnetic material and b) hard magnetic material. After [27]

$$D_{cr} = 2\pi\sqrt{A/K_U} \tag{1.58}$$

where A is the stiffness constant, K_U is the induced anisotropy. If we apply an in-plane external field along the magnetization direction, it shifts the critical thickness to larger values:

$$D_{cr} = \frac{2\pi\sqrt{A/K_U}}{1-h} \tag{1.59}$$

where h is the reduced field $h = 1/2H_{ex}J_s/K_u$ with H_{ex} is the external field and $J = \mu_0 M$. Above this critical thickness the hysteresis loop shape is transcritical that corresponds to a two phases magnetization process involving in-plane and out of plane components: the in-plane component is quickly reverses at fields close to the coercive field, then the perpendicularly magnetized stripe domains have a linear approach to saturation, due to the magnetization rotation under the application of an in plane magnetic field (see figure 1.24). We can identify the anisotropy field that is due to the uniaxial stress anisotropy.

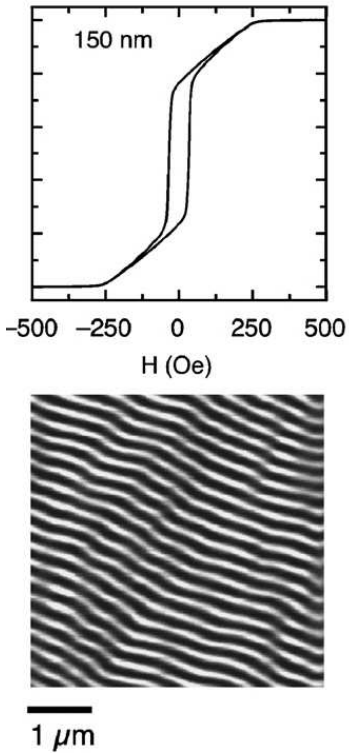

Figure 1.24: Fingerprints of stress presence FeSiB thin films with thickness of 150 nm: transcritical loop and MFM stripe domains pattern. After [29]

Chapter 2

Experimental techniques

In this part of this work I am going to show the main instruments and the analysis techniques used during my activity. In particular I will show the synthesis and the growth technique in the first sections, then the magnetic instruments like magnetometers and the morphological, compositional experimental techniques.

2.1 Sputtering deposition

Thin films can be obtained by different chemical or physical techniques. In particular we use a physical vapor deposition (PVD) technique that consists in a vacuum deposition process where the coated material is passed into vapor phase by physical mechanism, in particular we chose sputtering deposition. Thin films that have been studied during this thesis have been grown by Radio Frequency (RF) Sputtering, and Magnetron Sputtering. These techniques have been chosen for their flexibility for the high control of thickness and for the possibility of controlling the film characteristics. In sputtering the material is called target and it is bombarded with inert gas ions, in our case Ar, that is chosen because it has an atomic mass similar to the metal atomic mass. The chamber in which the target is placed is at low pressure usually $10^{-8} mbar$ and during deposition a dynamical pressure is obtained with Ar introduction and pumping on the same chamber. A potential difference between cathode and substrate is maintained, while in the first sputtering devices the potential difference was continuous and the target was at lower potential than the substrate, now in the radio-frequency sputtering the potential difference changes in sign with periodicity in the radio-frequency range. The Argon is ionized by natural radiation and free electrons are generated. These electrons can not recombine with Ar ions because of the electric field presence. If their kinetic energy is enough they can ionize other ions, giving rise to an avalanche effect. In addition to ionization there is an excitation

process of the gas, and, after the excitation an emission related to spectral lines is present, so a bright region is present. The Ar ions have a lower mobility with respect to electrons and for this reason they shield the electric field near the target, where no excitation of gas is still present and for this reason this zone is called dark space o sheath. A scheme of the behavior is done in figure 2.1.

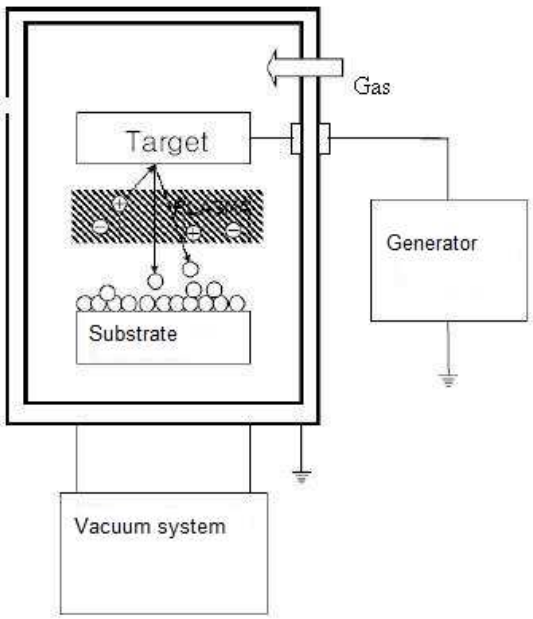

Figure 2.1: Scheme of a sputtering apparatus

The plasma zone is a neutral zone in which positive charges equal negative charges and the only area in which the ionization is possible is near the cathode so the distance between target and substrate musts be higher 2 or 3 times than the sheath width. The argon ions are accelerated to the target, and transfer kinetic energy to the target atoms and if their kinetic energy is enough, that means if it is greater than the binding energy of the atoms that is in the range of 5 to 10 eV, the atoms of material are removed. The Ar ions are neutralized during the impact and rebound on target surface. The neutral atoms of material are removed and have a kinetic energy equal to 3-10 eV, so they arrive to the substrate with an energy of 1-2 eV, enough to create a film with good adhesion. If the target is a single crystal then the atoms follow specific directions that depend on the crystallographic directions.

Two parameters have to be taken into account in a sputtering process: the minimum energy that we must transfer to the atoms in order to have the sputtering effect and the yield that is

defined as the average number of target atoms ejected per incident particle.
Radio frequency techniques are usually employed, such as: RF sputtering and magnetron sputtering are used instead of DC sputtering in order to avoid the charge accumulation on target surface also allowing to sputter nonconducting targets. Indeed in a DC apparatus it is not possible to deposit an insulating material because on the target surface a negative charge will accumulate, which causes a potential negative with respect to the plasma. If a radio frequency difference of potential is applied to the electrodes with a frequency of 13.56 MHz, they reverse their cathode-anode polarities each half-cycle. At high frequency the positive ions do not have enough time to migrate to negative charge so that at each polarity inversion there is an increment of negative charge on the walls. The target can be represented as the walls that are at a negative potential with respect to plasma, and, for this reason, it is bombarded by positive ions. During each cycle for a short time it is positive ,and during this time, the negative current compensates the positive in order to avoid a charge accumulation. In order to avoid that the accumulation of charge changes the voltage a matching network is used to match the capacitive impedance of the load and the power supply. The substrate electrode is much larger than the target one in order to have an asimmetry that is necessary to avoid continually sputtering on both target and substrate. The magnetron sputtering allows to work at lower pressures and higher deposition rates compared to the DC technique. In this case a magnetic field is applied parallel to the target surface and, in this way, the secondary electrons responsible of the discharge sustenance are submitted to a Lorentz force and cover a longer path close to the target surface that permits a better ionization process. In this thesis the sputtering apparatus is formed by a main chamber and a load-lock useful for the substrate loading. In the load-lock a vacuum of $10^{-5} - 10^{-6}$ mbar is done by a turbomolecular pump, lower than the vacuum of the main chamber that is around $2 - 3 \cdot 10^{-8}$ mbar reached by a cryopump. The main chamber is separated by a throttle valve from the cryopump and during the sputtering process it is open for a 20% while the flux of Ar is controlled through a fluximeter and, in this way, a dynamical equilibrium of pressure is possible, allowing to operate in clean conditions during the sputtering process, but also avoiding the saturation of the cryopump by the sputtering gas. The transfer of sample from the load-lock to main chamber is possible only when argon is present in the main chamber and the maximum vacuum is present in load-lock in order to have a very clean atmosphere and a flux of gas in direction of load-lock. They are connected by means of a guillotine valve. In the main chamber there

are three targets in vertical position and the substrate can oscillate in front of them thanks to a coaxial cylindrical support which rotates controlled by a motor with a feedback obtained by an optical encoder. Each target has a matching network and and independent power supply, so they can be switch together or alone. The amplitude of oscillation, the speed and the time are set up by a software. The substrate can be heated at temperatures up to 600°C by a heater that is in the back side of the substrate-holder and the real temperature can be read by a thermocouple put on the substrate before the deposition. After heating, the substrate can be cooled down to room temperature with a flux of compressed air on its back side. The rate of growth was controlled by means of a calibration samples in different conditions. The calibration samples are grown on silicon with native oxide and after a specific number of oscillations at a specific speed we obtain the thickness of sample by an alpha-step profiler after having etched a part of film. The important parameters to be controlled in a deposition process are the power and pressure. The rate grows linearly with power and has a maximum at a specific pressure that depends on target material.

2.2 Chemical synthesis of nanoparticles

While for obtaining thin films we have used a physical technique, the magnetite nanoparticles have been obtained by means of chemical technique. The chemical techniques are better than physical ones if a great amount of material is needed and for the application this is an important requirement. The nanoparticles must satisfy two important requirements: the size monodispersion and the absence of aggregation. These conditions can be obtained through two different chemical syntheses, co-precipitation and thermal decomposition, both of them give rise to a rapid nucleation and a low diffusion that means an high control of size distribution [30].

Co-precipitation

The co-precipitation method is very used in order to obtain big amount of nanoparticles and it consists in the introduction in a basic solution in water salts of Fe^{II} and Fe^{III} in a stoichiometry ratio and the reaction can be written in the following way

$$Fe^{2+} + 2Fe^{3+} + 8OH^- \rightarrow Fe_3O_4 + 4H_2O \tag{2.1}$$

The average size of the obtained nanoparticles and their composition depend on the type of used salts, on the ratio between the ions Fe^{2+} and Fe^{3+}, on the temperature of reaction,

on the pH and on the atmosphere. Nanoparticles obtained through this technique tend to precipitate, to form aggregates and to oxidize in maghemite, in order to avoid these processes a surface coating can be added, during or after the synthesis.

Thermal decomposition

The second chemical synthesis is the thermal decomposition from low boiling organometallic precursors, in presence of surfactants that work like surface stabilizers. These methods have several advantages in particular the precise control of size and shape, an high crystallinity and a narrow particle size distribution. The usually precursors are $Fe(acac)_3$ or $Fe(CO)_5$ [30] while the surfactants can be acid oleic or oleilammine, in 1-hexadecane or trioctylamine [30]. The important parameters to be controlled are: the ratio between oragnometallic precursors and surfactants, the reaction temperature, the synthesis procedure, the atmosphere. The obtained nanoparticles are dispersible in polar solvent and in order to use them in biomedical application is necessary to be dispersible in water and this can be possible through surface silanization and polymer or micelle coating.

2.3 Morphological and structural characterization

The main techniques used to identify the morphological and structural characteristics of the sample are the same for nanoparticles and films and are techniques with a spatial resolution of few nanometers.

2.3.1 X-ray Diffraction

X-ray diffraction is one of the most used technique able to identify the structure, the composition and physical properties of material, and thin films or powders. It is based on observing the scattered intensity of an X-ray beam hitting a sample as a function of incident and scattered angle [1]. The photon energies of X-ray is in the range of 100 eV - 100 keV, but for diffraction the wavelength has to be comparable with the size of atoms and interatomic distances, so only short wavelength x-rays in the range of a few angstroms to 0.1 angstrom that corresponds to 1 keV to 120 keV are used and the targets used in x-ray tubes are Cu and Mo which emit at 8 keV and 14 keV. The scattering x-ray process can be elastic or inelastic, in the first case it is called Thompson Scattering while in the second case is called Compton Scattering. In the elastic process there is no moment change while in the inelastic process there is a change of

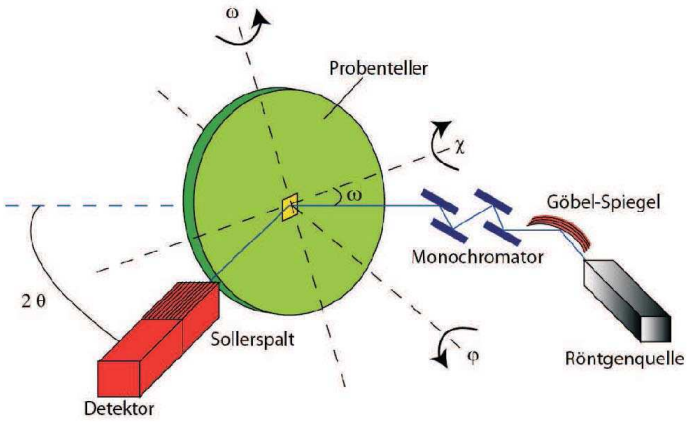

Figure 2.2: XRD difractometer scheme [31]

the moment and of wavelength of the incident wave. The diffraction is an elastic process, in fact we can see a variation of intensity of scattered wave in dependence on incident angle indeed if the atoms are arranged in a periodic lattice there are sharp interference maxima peaks with the same symmetry as in the distribution of atoms and, by the diffraction pattern, it is possible to have informations about the distribution of atoms in a material and the position of peaks depends on the atomic distances. For a given set of lattice parallel planes and an inter-plane distance of d, the condition for diffraction is given by the Bragg's law

$$n\lambda = 2dsin\theta \tag{2.2}$$

where θ is the incident angle, λ is the wavelength and n is an integer that represents the order of the diffraction peak. A diffractometer is made up of different parts: the x-ray source, a monochromator, the sample holder and the detector (as shown in figure 4.15). Usually a diffraction measurement is done in $\theta - 2\theta$ configuration that means that detector is moved to the same angle of incident x-ray. The used instrument is a Brucker AXS D8 and Phillips XPert high resolution X-ray diffractometers and an adding element is present as shown in figure 4.15 , the mirror, that permits to have an incident monocromatic ray without loose the intensity.

2.3.2 Trasmission Electron Microscopy

Trasmission electron microscopy (TEM) is one of the most important experimental technique used to have information about structure, morphology and composition of nanostructures. An electron beam is the investigation probe and its wavelength depends on acceleration. When

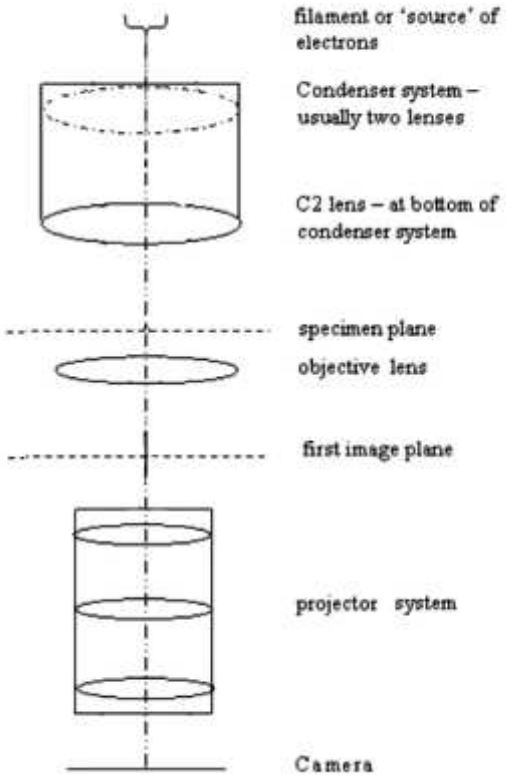

Figure 2.3: Trasmission Electron Microscopy simplified scheme

electrons interact with a sample many different signal can be produced either reflexed: Auger electrons, backscattered electrons, secondary electrons, characteristic x-ray, visible light; or transmitted: elastically scattered electrons, inelastically scattered electrons; bremsstrhlung x-ray. From these rays one can have information about the specimen under study. In particular we are interested in elastic process: small angle elastic electrons that give informations about the structure, while the high angle elastic electrons are proportional to the atomic mass Z and give information about the composition (EDS). Also inelastic electrons are very important because give complementary informations. The characteristic x-ray are produced from the decay of the excited electrons and are used by (XEDS).

A typical TEM apparatus is shown in figure 2.3, we can see several parts that correspond to a typical configuration:

- two or three condenser lenses to collimate the electron beam and to reduce the divergence
- the samples is in a sampleholder position able to rotate, the sample must be sufficient

thin in order to permit the transmission of electrons

- downline of sample there are objective, intermediate and projector that create the image of sample

The objective lens is on the back focal plane of sample and allows the transmitted beam or a diffracted beam to contribute to the image formation. It is possible to select two ways for obtaining the images: phase contrast or amplitude contrast. In the first case the images are obtained by selecting only one electron beam between the transmitted (bright field BF) or the diffracted (dark field DF). In the second case the images are obtained by recombining the transmitted and diffracted beams.

High Resolution TEM

The High Resolution TEM (HRTEM) images can be obtained by means of phase contrast and in particular one transmitted beam with several diffracted beams are analyzed. HRTEM is a very sensitive and interesting technique and it depends on thickness of sample and also on the optical focus, for the second reason in order to have a good imaging it is important to have an high performance microscope that means high stability of column and low spherical aberration.

Scanning TEM

The Scanning TEM (STEM)mode is very useful to have a large area information of sample. In this case the electron beam scans the surface and its position is controlled by a coil. The electrons that have interacted with sample are collected and their intensity is reported as a function of position in order to have a complete image of the sample on a scanning area. The STEM detector is placed under the sample in the focal plane of the objective lens and it consists of a series of concentric rings placed on optic axis that are able to integrate the signal. They are divided in Bright Field and Dark Field. The higher resolution can be obtained by means of a HAADF (High Angle Anular Dark Field), is named *Z-contrast* because the high angular scattering electrons, as already told, have a dependence on the Z. The intensity of the formed image depends on Z, the bright part corresponds to high Z while dark part to small Z material. In STEM modality other two important techniques are possible Electron Energy Loss Spectrometry (EELS) and Electron Dispersive X-ray Spectroscopy (EDXS).

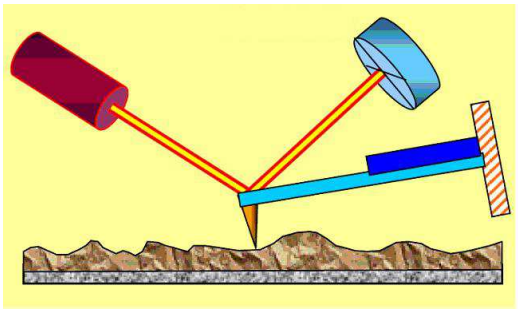

Figure 2.4: Representation scheme of a AFM system. The laser light is reflected by a cantilever under which a tip is put. The forces between the surface and tip give rise to a bending on the cantilever that is registered as a variation in diode signal.

Energy Dispersive X-ray Spectroscopy

The X-ray emission is originated from the inelastic process of electron scattering and two types of x-rays are originated: characteristic x-rays that give the chemical compositional informations, and the bremsstrahlung that are due to deceleration. The electronic beam has an high energy and for this reason interacts with inner shells of electrons, and if the given energy is higher than the ionization energy, the electron is expelled and a vacancy is obtained and an outer electron goes to occupy this position and x ray is emitted. The detector used for this kind of measurement is a solid state detector usually based on Silicon doped with Lithium.

Electron Energy Loss Spectroscopy

In this technique the energy distribution of electrons that have passed the sample have been analyzed. We can have information about chemical and electronic structure of sample and for this reason is considered as complementary to EDXS because it is able to identify light elements that are not obtained through EDXS.

2.3.3 Atomic Force Microscopy

The atomic force microscopy is a very useful technique used to have informations on the surface morphology of the sample and is used for very different samples. A laser illuminates the surface of a cantilever under which a tip is present (see figure 2.4) that is the physical fulcrum of the system.

The force between the tip and the sample surface gives origin to a deflection and by measuring this deflection we can evaluate the interaction between the two elements. The

reflexed ray on the cantilever is acquired by means of a set of four photodiodes and from the difference between them we can obtain the lateral bending. The cantilever position is controlled by the elongation of a piezoscanner. The tip interacts with samples through different forces as ionic repulsion or Van der Waals. Two possible measurements can be done: in contact mode or in tapping mode. In the first case the tip is in contact with the surface and the variations in force are in the range of repulsion force, while feedback is on the bending. The piezoscanner extends in order to maintain the force constant and its signal corresponds to morphology. In tapping mode the tip is vibrating near the surface and the force causes a variation of oscillating frequency that causes a variation in the amplitude of vibration. The feedback is on vibration amplitude and the signal given by piezoscanner corresponds to morphology. In this thesis the surface morphology has been investigated by a Dimension 3100 Atomic Force Microscope equipped with a Nanoscope IVa controller (Veeco Instruments).

2.3.4 Dynamic Light Scattering

DLS is a very useful technique to have information about the dispersibility of nanoparticles and their behavior in a solvent. DLS is used in many different field from chemistry, to physics, to biology. A very diluted colloidal dispersion of nanoparticle is usually needed. The nanoparticles are considered as non interacting and their position depends only on Brownian motion, due to the bombardment by the solvent molecules that surround them and the speed at which the particles are diffusing. This measurement can be done by measuring the rate at which the intensity of the scattered light fluctuates. The autocorrelation function, given by the intensity at two different times (see equation 2.3), is measured and depends on the size distribution of nanoparticles.

$$G(\tau) =< I(t)I(t+\tau) > \tag{2.3}$$

where $G(\tau)$ is the autocorrelation function after a time τ of scattered intensity $I(t)$. A correlator is used in order to obtain the autocorrelation function, it is designed to measure the degree of similarity between one signal with itself at different times, in this way, for a randomly fluctuating signal, the correlation depends on time, in fact if the intensity of signal at time t is compared to the intensity a very small time later $t + \delta t$, there is correlation, while if it is compared with $t \to \infty$ no correlation can be observed. Small particles cause the intensity to fluctuate more rapidly than the large ones so there is a dependence of signal correlation on

particles size. Through DLS we measure the autocorrelation function normalized g^2given by

$$g^2(t) = \frac{I(t)I(0)}{I(0)I(0)} \tag{2.4}$$

that following the Einstein theory and in the hypothesis of a monodispersed nanoparticles is given by

$$g^2(t) = 1 + exp(-q^2Dt) \tag{2.5}$$

where: $q = \frac{4\pi n}{\lambda} sin\frac{\theta}{2}$ is the scattering vector where θ is the scattering angle, λ is the wavelength of radiation, n is the diffraction index of the medium. D is the translational diffusion coefficient:

$$D = k_B T/6\pi\eta R \tag{2.6}$$

where R is the hydrodynamic radius, T is the temperature, η is the viscosity and k_B is the Boltzmann constant. From the above theory we can understand that by fitting the signal we can obtain the hydrodynamic radius for the nanoparticles.

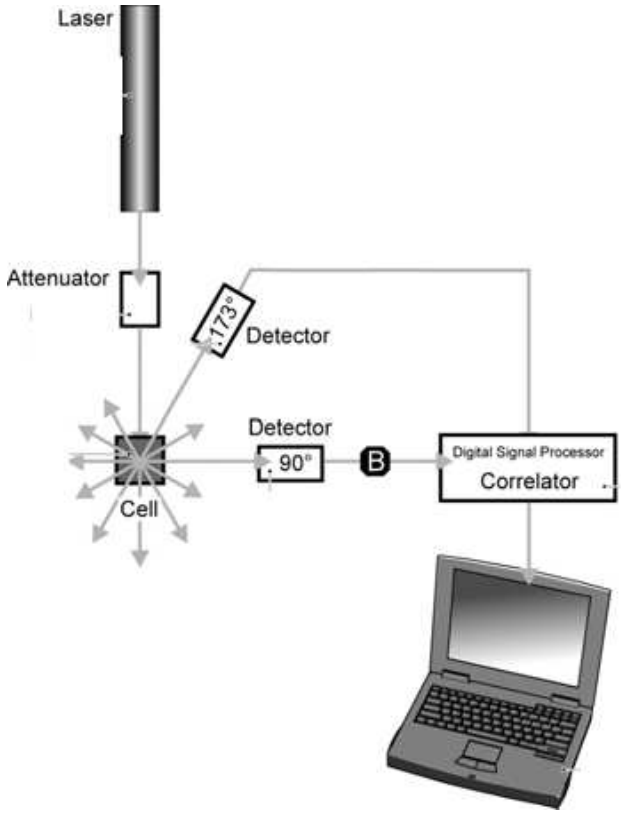

Figure 2.5: Dynamic light scattering typical configuration

A typical dynamic light scattering system is shown in figure 2.5, it comprises: a laser providing a light source to illuminate the sample contained in a cell, an attenuator used to

reduce the intensity of the laser source and hence reduce the intensity of scattering; a detector used to measure the scattered light that can be positioned at either 173 or 90 degree (in our instrument is at 90). For samples that do not scatter much light,then there is a correlator that compares the scattering intensity and it is interfaced with a pc.

2.4 Magnetic characterization techniques

The magnetic characterizations are important for this thesis and here I am going to describe the main instrument used, in particular magnetometer VSM (Vibrating Sample Magnetometer), AGFM (Alternating Gradient Magnetometer) and SQUID. Other two techniques have been used: MFM (Magnetic Force Microscopy) that have been used for thin magnetic films in order to obtain the magnetic domain pattern and the TMA (Thermo-magnetic analysis) that is useful to see the phase transitions as a dependence of temperatures and the present phases.

2.4.1 Vibrating Sample Magnetometer

Vibrating sample magnetomer is based on magnetic induction [32], indeed the sample is vibrating perpendicular to a static magnetic field H_{st} generated by an electromagnet. The scheme of instrument is reported in figure 2.6

The motion of sample induces for Faraday's law an electromagnetic force in the pick-up coils that can be written as:

$$V = -NA\frac{dB}{dt} \tag{2.7}$$

where N is the number of windings, A is the transversal coil area, B is the magnetic induction. This signal is proportional to magnetic moment of sample if we consider it as a point with a magnetic moment m. The magnetic induction at the pickup coils follows the equation:

$$B = \mu_0(H_{st} + m \cdot f(z)) \tag{2.8}$$

the signal changes in the time dt only because of the variation of B done by the oscillation of m (f is the function of the m position) and we have the equation

$$V = -\mu_0 NAm\frac{df}{dz}\frac{dz}{dt} \tag{2.9}$$

as shown in equation 2.9 the voltage is proportional to the magnetic moment of the sample. The signal is amplified thank to a lock-in amplifier that increases the signal to noise ratio in order to have an high sensibility. The instrument used in this thesis is a LakeShore VSM with

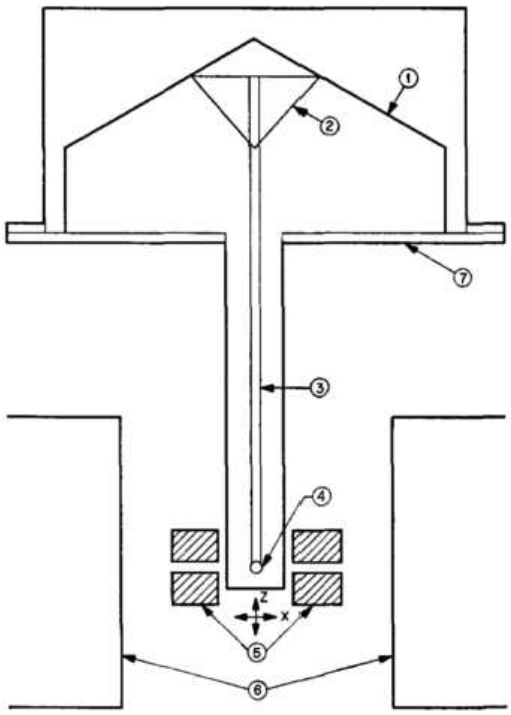

Figure 2.6: Vibrating Sample Magnetometer scheme: 1) oscillation control, 2),4) support, 3) beam on which the sample can oscillate, 4) sample, 5) pick-up coils, 6) poles of electromagnet

a sensibility up to 10^{-3} *emu* and an applied field up to $2\,T$, the magnetic field is measured by means of an Hall probe. A closed loop helium cryostat is present and permits temperature measurements from 28 K to 380 K.

2.4.2 Alternating Gradient Magnetometer

The alternating gradient force magnetometer (AGFM) is a very sensitive magnetometer and it is based on a force measurement. It has a sensibility up to 10^{-8} *emu*, it is able to measure with a relative error of 2%. The magnetic field is up of 2T and applied by means of an electromagnet as can be seen in figure 2.7 and it is measured by an Hall probe. A magnetic alternating field gradient $h = hsin(\omega t)$ is applied thanks to two coaxial coils [33] in which the currents flow in opposite directions in a first gradient configuration and it is superimposed to a fix magnetic field (see figure 2.8). The sample is placed on a quartz beam connected to a piezoelectric element. This beam has a vibrating sample from 100 to 1000 Hz and when the sample is present it changes the resonant frequency. On the sample a force proportional to

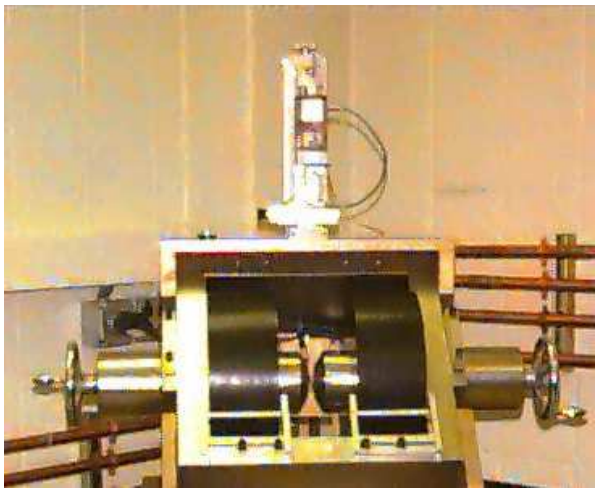

Figure 2.7: AGFM instrument photo

the magnetic moment and to the gradient field intensity is present:

$$\vec{F} = \vec{\nabla}(\vec{m} \cdot \vec{h}) \tag{2.10}$$

We consider as x the direction of field application and as z the sample holder (as shown in figure 2.8)

$$\vec{F} = m_x \frac{dh_x}{dx} \tag{2.11}$$

This force causes a deflection on the beam that is felt by piezo element and the difference of potential is proportional to the force $\vec{F}$ and at the same frequency of the applied gradient field. In order to have an higher signal to noise ratio, a lock-in amplifier is used and the field frequency is fixed near the resonance frequency of the system. The instrument used in this thesis is a Micromag MODEL 2900 Princeton Misurements Corporation.

2.4.3 SQUID Magnetometer

The SQuID (Superconducting Quantum Interference Device) magnetometer is one of the most sensitive device for the detection of magnetic moment. It is able to perform measurements in a large range of temperatures and fields up to several Tesla. The sensitive element is a SQuID sensor that consists in a superconducting ring interrupted by two Josephson junctions, i.e. two thin insulating layers (see figure 2.9).

If a current flows through the the ring, it divides so that equal currents pass through each of two Josephson junctions, but when a magnetic external field is present it generates a voltage

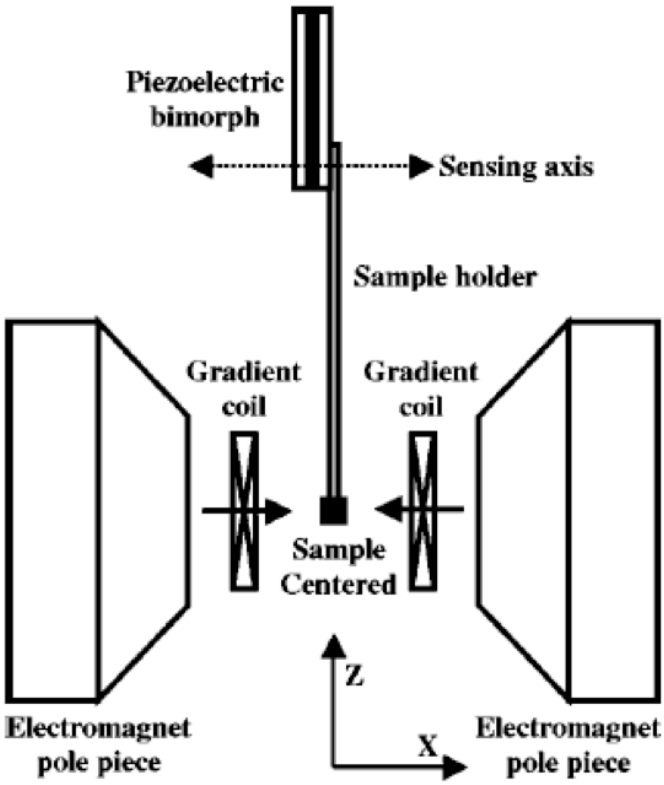

Figure 2.8: Scheme of AGFM instrument

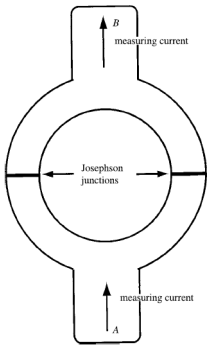

Figure 2.9: SQuiD sensor scheme. After [2]

and a current in the ring, according to Faradays Law and this induced current adds to the current in one junction, and subtracts in the other. In this way there is a voltage step that corresponds to the passage of a single flux quantum across the boundary of the ring given by the equation

$$\phi_0 = \frac{h}{2e} = 2.07 \cdot 10^{-15}\, Tm^2 \tag{2.12}$$

The magnetic flux through this ring is converted to an electrical voltage. This magnetic flux

is generated by the movement of the sample in an area where a constant field is applied, usually by means of superconductor. Thanks to a lock-in amplifier the signal to noise ratio is increased. The magnetometer used in this thesis is a DCSQUID models from Quantum Design, the maximum applied field $5.5T$.

2.4.4 Thermo-magnetic Analysis

Thermo magnetic analysis is an home made technique, useful to obtain informations about the present phase or the variation of the proprieties of a material with the temperature. It consists in applying through a coil a small field up to 100 Oe at a frequency of 250 Hz. The signal is detected by pick up coil and it is proportional to susceptibility. Thanks to an heater the temperature can be changed up to 1000°C and permits to observe the variation of signal as function of temperature. The temperature variation is measured directly on the sample by means of a thermocouple. The signal is amplified thanks to a lock-in amplifier and is related to temperature variation.

2.4.5 Magnetic Force Microscopy

The magnetic force microscopy is a scanning probe microscopy technique and it is very useful to have information about the domains pattern of the magnetic film, but it can be also used to identify magnetic domains in nanostructures if they are enough big to have magnetic domains. The magnetization perpendicular to the film plane can be measured by means of a tip with a coating of $Co - Cr$ used in an interleave non contact mode. The tip oscillates and scans each line of the sample surface, two times while oscillating: during the first time the morphology is identified, and during the second time it oscillates at a fixed distance of 20-50 nm, in order to eliminate the morphologic contributions and to sense only to magnetic forces.

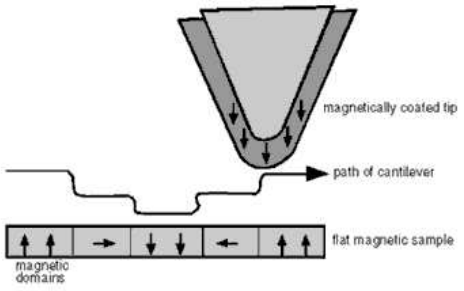

Figure 2.10: MFM measurement scheme, the tip is vibrating over the sample

The tip can be considered as a magnetic dipole and its interaction with the sample can be

written as:

$$F_{mag} = \mu_0 \int_{V_P} m_p \frac{\partial H_z}{\partial z} dV \tag{2.13}$$

where m_P is the tip moment aligned in z direction, H_z the field out of sample.

The phase shift ϕ of the cantilever oscillation is related to the force F given by equation 2.13 experienced by the tip due to the magnetic stray field H:

$$\phi = -\frac{Q}{K}\frac{\partial F_z}{\partial z} = -\frac{Q}{K}\frac{\partial^2 H_z}{\partial z^2} \tag{2.14}$$

where Q is the quality factor of the oscillation, K is the force constant of the cantilever and z the distance between the tip and the sample. Two different contrasts can be identified in a MFM signal corresponding to the opposite out-of-plane components of the magnetization vector. In this thesis the domains pattern has been investigated by a Dimension 3100 Atomic Force Microscope equipped with a Nanoscope IVa controller (Veeco Instruments).

2.4.6 Magnetic hyperthermia apparatus

A magnetic hyperthermia measurement consists in applying a magnetic radio frequency field typically lower than 1000 Oe at a colloidal solution of nanoparticles. The field is applied by means of a coil placed around a dewar inside which there is the sample. This cryostat that guarantees an adiabatic measurement is made of glass and has an internal sleeve in which a vacuum of 10^{-6} $mbar$ is obtained thanks to a turbomolecular vacuum pump. A scheme

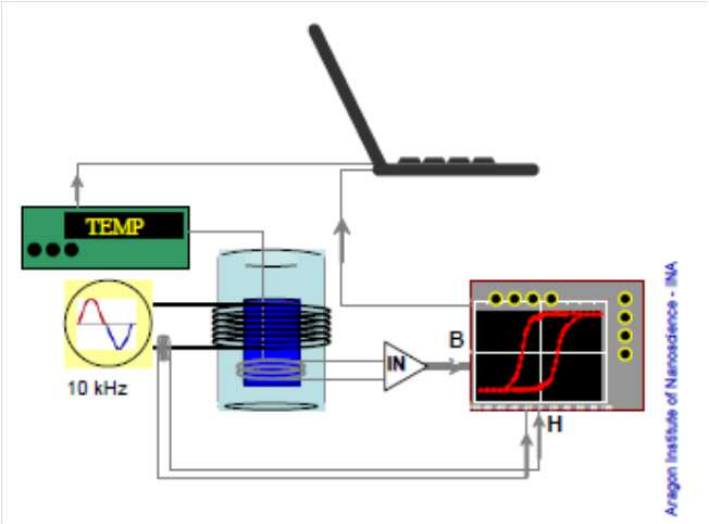

Figure 2.11: Scheme of an hypethermia setup instrument

of the instrument is shown in figure 2.11, in which there is also a pick up system to obtain

the variation of hysteresis loop as a function of the applied field. In our instrument, for the moment, we do not have this possibility. The variation of temperature in dependence of time is measured by means of a fiber optical thermometer in order to avoid the coupling of signal with the radio frequency. Knowing the nanoparticles concentration we can obtain the value of the specific absorption rate (SAR). In this thesis an ac field applicator (nanoScale Biomagnetics DM100) has been used with maximum fields up to 300 G and frequencies up to 430 kHz.

Chapter 3

Amorphous magnetic thin films

3.1 Introduction

In the last decades, the request of miniaturization of devices has caused an increased interest in thin magnetic films, in particular for the possibility of their direct integration. Many different kinds of sensors are based on magnetic materials [34], for example flux-gate sensors use magnetic material as flux concentrator [35].

In particular amorphous and nanocrystalline magnetic materials have been studied for their soft magnetic properties and for the possibility of tune their coercitivity and anisotropy by means of heat treatment [36] also obtained with joule-heating [37].

They are used as sensing elements in sensors of magnetic fields, stresses and position [35, 38] and as power cores for transformers [39]. In the last years these materials have been studied in form of thin films for soft underlayers for perpendicular recording [40, 41], free layers in magnetic tunnel junctions and spin valves [42] and for the incorporation in an on-chip inductor in order to increase quality factor Q and inductance density[43, 44].

The control of magnetic and physical characteristics is very important in order to obtain an efficient device.

Many different compositions exist and were tested during the past years for the device integration [45]. Our idea is to use a commercial amorphous alloy VITROVAC 6025X usually used in form of ribbon[46]. We would like to obtain it in thin film and to study the dependence of structural, morphological and magnetic characteristics to the growth parameters in order to improve the material behavior as flux concentrator in hall sensor and fluxgate sensor. This work has been done in collaboration with group of Dr. Morelli (STMicroelectronics). We chose VITROVAC composition after a complete and exhaustive study of existing literature

because it is a zero-magnetostriction material, with high saturation magnetization 0.58 T[46], high Curie temperature 200° C [46], high crystallization temperature 530° C [46] and very high magnetic permeability 100000 [46].
This last crucial property can obtained by lowering the anisotropy and for this reason we grew an amorphous alloy and we studied the dependence of stress anisotropy on the growth parameters.

3.2 Magnetic sensors

Hall sensor with magnetic material

Hall sensors are widely used as magnetic field detectors, and they are able to identify the presence of a magnetic field Bz perpendicular to the plane. An integrated Hall cell is generally obtained with four contacts of n-type well in a p-type silicon substrate [47],[48]: two opposite contacts along the x-axis are used to inject a bias current I_{bias} hence we can identify between the other two contacts along y-axis an Hall voltage V_H (equation 3.1) proportional to the magnetic field normal to silicon surface B_Z (see figure 3.1).

$$V_H = \frac{-S_H G}{ned} B_Z I_{Bias} \tag{3.1}$$

where $n$is the doping concentration, d is the thickness of the n-well respectively, G is a geometrical correction factor, S_H is the scattering factor of silicon usually 1.15. From the above formula 3.1,for increasing the signal to noise ratio, Hall cells must have a lateral dimension smaller than the diffusion layer thickness. Therefore, electrons are forced in a XY plane so their path is influenced only by the Z component of the magnetic field. In order to obtain

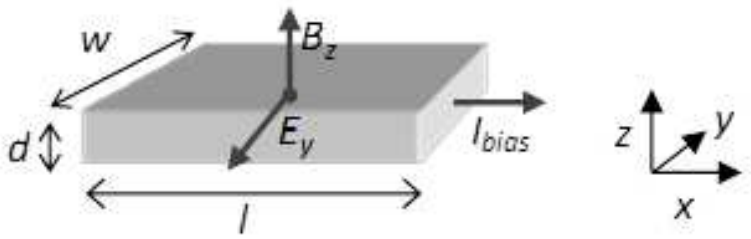

Figure 3.1: Single Hall cell

the other two components of the magnetic fields B_x and B_y that are parallel to the surface, usually a ferromagnetic material with soft magnetic characteristic is used for bending the parallel components towards the normal direction. This magnetic concentrator is a disk with four

groups of Hall cells that are located at its edges along the X and Y directions (see figure 3.2) The magnetic flux converses at one edge and diverges at the other, in this way, the Hall cells experience a magnetic field component upward at the flux convergence side and downward at the flux divergence. A proper signal treatment will twice the Hall output reducing the impact of a common-mode z-axis magnetic field. Therefore it is possible to integrate into the same chip a three-axis magnetic sensor: the XY axes by means of four Hall cells with magnetic concentrator and the Z axis with one group of Hall cells. In order to increase sensitivity we

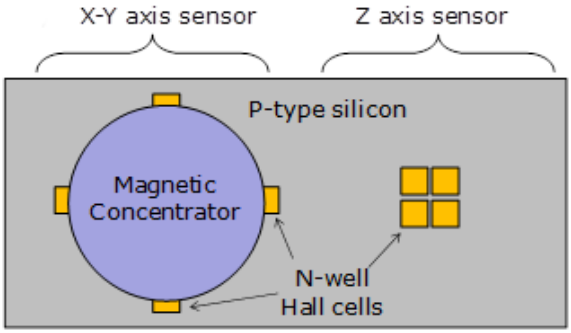

Figure 3.2: 3D Hall sensor scheme

need to control the geometrical parameters of concentrator as: thickness, distance from Hall cells (silicon), shape and profile. The thickness can be controlled through the deposition, the distance from silicon is given by the thickness of dielectrics of metal interconnections, the shape is defined by the lithography process and the profile is the results of the beneath dielectrics morphology.

Flux-gate sensor

A Fluxgate sensor is a directional device able to measure a magnetic field parallel to its magnetic core [49]. It consists of two coils: a primary (excitation) and a secondary (sensing) coil, that are around a soft ferromagnetic core (figure 3.3). The excitation current I_{exc} flows in the primary coil and produces a field that periodically saturates the soft magnetic material core. When an external magnetic field is present even harmonics appear in the voltage V_{ind} that is induced in the secondary coil. Without an external magnetic field, only odd frequencies f, 3f, 5f, 7f ecc.., are present because of symmetry in the transfer function that is broken if a magnetic field is present.

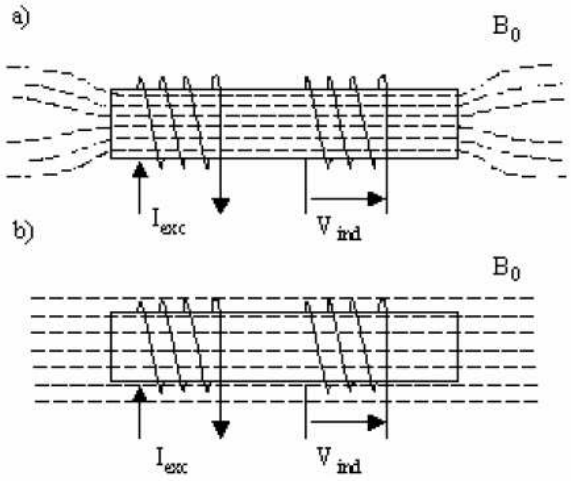

Figure 3.3: Fluxgate a) without saturated core, b) saturated core

The voltage in the secondary coil is simply given by the Faraday law

$$V = \frac{-d\phi}{dt} = -N_{sens} S \frac{dB(t)}{dt} = -N_{sens} S \frac{d}{dt}\left(\frac{\mu N_{exc} I_0 sen(2\pi f_{exc} t)}{l}\right) \tag{3.2}$$

where where N_{sens} is the number of turns of the sensing coil, N_{exc} is the number of turns of the excitation coil, S is the cross section of the sensing coil, l is the length of the excitation coil, μ is the magnetic material permeability and $I_0 sin(2\pi f_{exc} t)$ is the excitation current. In the last decade many efforts have been devoted to the miniaturization of devices and their integration with CMOS technology, new topologies of planar integrated micro-Fluxgate have recently been presented [50],[51]. Very interesting is the differential single axis planar Fluxgate magnetic sensor (shown in figure 3.4). The ferromagnetic core is over the diagonal of the excitation coil and if no external magnetic field is applied, the two sensing coils, connected in antiseries, show an output voltage that ideally is zero. When a magnetic field is applied and parallel to the core the magnetization in one half of the core is in the same direction of magnetic field, while the magnetization of the other half it is in the opposite direction, for this reason, there is a difference of voltage in the two coils. The planar geometry of sensor (figure 3.4), gives the possibility to the direct integration of material.

3.3 Soft magnetic materials

Soft magnetic materials can be used for applications in which an high magnetic permeability is necessary $\mu = \frac{B}{H}$. The hysteresis loop is very narrow that means low coercivity field and high saturation magnetization.

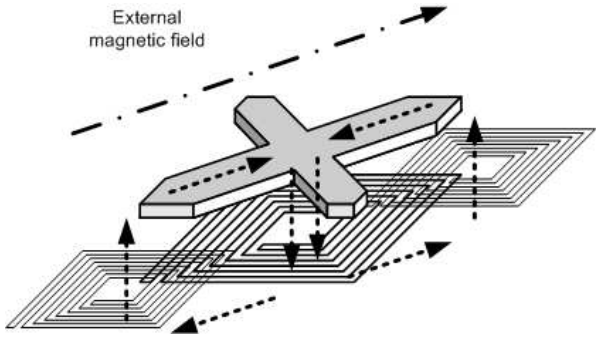

Figure 3.4: Planar fluxgate sensor geometry

Their main use is as magnetic core in transformers, motors, inductors and generator, where the main problems to solve, are the energy losses: due to eddy currents, acoustic losses due magnetostriction, hysteresis losses (in particular at high frequencies). These problems can be reduced by reducing the core thickness, increasing resistivity and decreasing grain dimensions and magnetostriction. The initial rotation of moments gives rise to the following equation for the magnetic permeability:

$$\mu_i = \frac{M_S^2}{\mu_0 \langle K \rangle} \tag{3.3}$$

where M_S is the magnetic saturation of the material. $\langle K \rangle$ is an effective anisotropy constant that takes into account all the anisotropy terms.
The coercivity is correlated to initial magnetic permeability because both of them depend on anisotropy constant. The coercivity field grows with anisotropy, while the permeability lowers.

3.3.1 Main materials

The most used and studied magnetic materials are shown below [5]:

- *Iron and Iron-Silicon*: The first magnetic material used for these applications is the iron. It has an high saturation value $B_S = 2.2T$, a cubic crystalline structure with an anisotropy constant, $K_1 = 4.8 \cdot 10^4 J/m^3$ and low magnetostriction values $\lambda_{100} = 21 \cdot 10^{-6}$ and $\lambda_{111} = -20 \cdot 10^{-6}$.

  The magnetocrystalline anisotropy is lower if a policrystalline material is used.

  If the material has high magnetostriction then localized strains can be present in particular directions that become pinning centers for walls.

  Also magnetic and compositional defects can be present and can give rise to local strains and pinning centers for walls. The principal impurities are: carbon, oxygen, nitrogen.

These defects usually are interstitial in the crystalline structure and can be removed by means of thermal annealing in inert atmosphere as argon.

The magnetic behavior usually is characterized by observing their magnetic characteristics by changing the frequencies and field typical of the device in which they are going to be used. In order to increase resistivity, silicon and aluminum are added in the crystal structure. In this way the anisotropy is lowered but also the saturation value.

The grains size must be controlled, in fact if it is too big, high dissipation currents can be present, instead if the grains are small we can have higher pinning points and hysteresis losses. If silicon and aluminum are both present in composition we obtain the *Sendust* $Fe_{1-x-y}Si_xAl_y$ where x=10% and y=5%.

- *Iron-Nickel (Permalloy)* The more three important compositions are:

  1. 78% Ni and 22% Fe. The magnetostriction and magnetocristalline anisotropy are very low. It is used in applications in which high initial permeability is necessary.
  2. 65% Ni and 35% Fe. It is easy to induce an anisotropy in it just by an annealing in magnetic field.
  3. 50% Ni and 50% Fe. It has very high saturation magnetization $B_S \approx 1.6T$ and a good answer to external magnetic field annealing.

  Ni-Fe compounds have an high Curie temperature, over $400°C$ and this is a good characteristic for their application. They are usually used in ribbon form, even if their application in thin film form is also studied and proposed.

- *Iron-Cobalt (Permendur)* $Fe_{0.5}Co_{0.5}$ has BCC crystalline structure, high saturation magnetization $B_S \approx 24kG$ and low magnetocrystalline anisotropy $K_1 \approx -1\ 10^5 J/m^3$. The magnotostriction is $\lambda_{111} = 25\ 10^{-6}$ and $\lambda \approx 150\ 10^{-6}$ and for a policrystalline material has an average value of $\lambda_S \approx 60\ 10^{-6}$. The magnetic anisotropy can be reduced by introducing vanadium that increases also the ductility, increases the resistivity, and improves the frequency behavior.

- *Soft Ferrites* They are characterized by low anisotropy, the generic composition is $MOFe_2O_3$ where M can be nichel, cobalt or zinc. Another group is $[M, Zn]Fe_2O_4$ where M can be cobalt, nickel or manganese.

  Their main use is the high frequencies applications.

- *Nanogranular material* For high frequency application, in order to decrease the losses, new materials have been studied as for example granular materials in which nanoparticles of Co, Ni, Fe, are embedded in a isolating matrix typically SiO_2, Al_2O_3 . This class is very promising because of the possibility of reducing eddy currents thanks to the nanogranular size, and by changing the distance between nanoparticles the magnetic behavior can be change by changing from exchange to dipolar coupling. The typical growth technique is reactive sputtering.

- *Metallic glass* Amorphous magnetic alloys are obtained through the rapid quenching from the melt, that precludes the formation of a crystalline order. In order to stabilize the glassy state, it is necessary to have some elements in the composition that are glass formers such as boron, carbon, silicon, or phosphorus [5].
  They can be based on 3d transition metals or on rare-earth metals. In the 3d case, the alloy is formed with metalloid such as boron, phosphorus and silicon which content is $15 < x < 30$ at %; or alternatively with transition metals of 4d or 5d type (Zr, Nb, Hf) with a content in the range 5-15 at %. Rare-earth metals can be stabilized by alloying with transition metals and metalloids: the transition metal content is in the approximate range 10-25 and the metalloid content is from 0 to 10 at %.
  We focus our attention on 3d- amorphous compounds.

  The main features of a magnetic amorphous alloy are the saturation moment, the magnetostriction, the Curie temperature and crystallization temperature. Usually the Curie temperatures of most cobalt-rich metallic glasses is higher than the crystallization ones, so it increases with the decreasing of metalloid content so as the magnetic moment. In structure there is not long range order and, for this reason, they have no magnetic crystalline anisotropy. Their resistivity is high if compared with Si-Fe o Fe-Ni, and for this reason they have a better behavior in frequencies applications.
  A very studied composition is Fe-Co-B with lower than 20% of B, it has a saturation up to 19.6 kG and it is mainly used in device in which an high magnetic induction is necessary.

  Another composition is Fe-B, its saturation is 16 kG,crystallization temperature 400-450°C, and it is used at low frequencies.
  There are many different compositions based on Fe-Co- and respect to policrystalline

materials, have higher resistivity and lower anisotropy.

3.4 Materials preparation

One of the material studied in this thesis is VITROVAC $(Co, Mo, Fe)0.87/(Si, Nb, B)0.13$. Boron, silicon and molybdenum create the amorphous structure while cobalt and iron are the magnetic materials. This material is usually used as ribbon and niobium improve the mechanical characteristics and lowers grains size. The material has: high permeability up to 10000, low coercivity (< 1 Oe), low grain size.

There are many possible compositions in order to obtain metal glasses [45]. In order to simplify the composition we decide to study other soft magnetic materials with less elements in the composition: $(Co, Fe)_x(Si, B)_y$ with $x = 0.1 - 0.9$ and $y = 1 - x$ and a greater presence of Cobalt in order to have low magnetostriction.

Ferromagnetic films of different thickness from 100 to 1000 nm were grown through sputtering on silicon substrate with thermal oxide (500 nm) and with an adhesion under-layer of Titanium or Tantalum with nitrogen 25 nm compatible with industrial sensor production. The films were produced from bulk massive targets by two different sputtering machines: an RF sputtering (available in IMEM laboratories) and a magnetron sputtering (available in STMicroelectronics laboratories). Even though the two sputtering machines have very different characteristics, pressure of sputtering gas (argon) was chosen as common growth parameter. Sputtering parameters were varied in order to obtain best magnetic, morphological and structural films characteristics.

In RF sputtering two different pressures were utilized: $3 \bullet 10^{-3}$ mbar and $1.4 \bullet 10^{-2}$ mbar. These pressures were chosen because they were used in the past for metallic thin films growth with stable discharge and growth process and resulting films had good adhesion to substrate [52, 53]. The voltage applied between target and substrate was varied between 900 to 1500 V and power was varied from 40 to 160 W. The growth rate changes from 2.3 to 6 nm/min.

In magnetron sputtering the highest pressure was used and power was varied form 1000 to 3000 W. The rate is approximatively 10 times higher than the rf sputtering ones.

3.5 Physical characterization

XPS (X-ray Photoelectron Spectroscopy) analysis was used to obtain film composition.

TEM (Transmission Electron Microscopy) and GIXRD (Glacing Incidence X-ray Diffraction)

analyses were used to have informations about the structure of samples.

The samples morphology was studied by atomic force microscopy AFM performed in tapping mode by a *Dimension 3100* scanning probe microscope equipped with a *Nanoscope IVa* controller *Veeco Instruments*.

The room temperature magnetic properties and magnetic microstructure of the samples were investigated by alternating gradient force magnetometry AGFM and magnetic force microscopy MFM in order to observe perpendicular magnetic signals. Magnetization curves of the samples were measured by AGFM with magnetic field parallel to the film plane.

3.5.1 Structure, morphology and composition

XPS highlights a composition rich in cobalt, similar to the massive target in the range of experimental error.

Both the analysis, TEM and XRD shows amorphous behavior. TEM diffraction pattern as shown in Figure 3.5 , highlights a diffuse ring corresponding to an amorphous structure. The present spots correspond to Titanium underlayer structure that is crystalline with a very good orientation on silicon substrate.

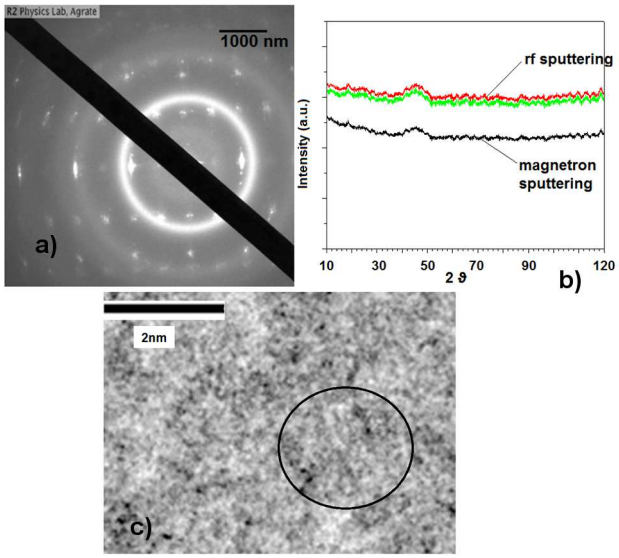

Figure 3.5: a) TEM diffraction pattern characteristic of analyzed samples, b) X-ray Diffraction pattern c) High Resolution TEM (HRTEM) image, the highlighted zone is a coherence phase signal that could correspond to a crystal grain with 2 nm average size.

The high resolution TEM images (Figure 3.5) indicates the presence of a coherent phase with size lower than 2 nm. The amorphous pick observed through GIXRD at 45° is equiv-

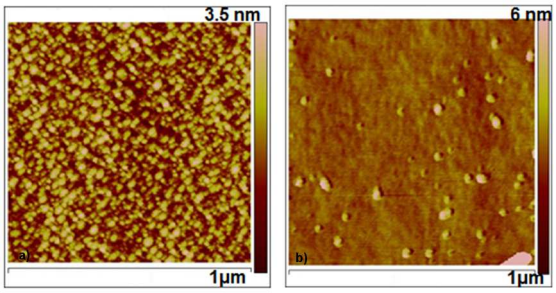

Figure 3.6: AFM signal, left: 100 nm sample grown through rf sputtering P= $1.2 \cdot 10^{-2}$ mbar V=1500 V (150 W), right: 100 nm sample grown through rf sputtering $P = 3 \cdot 10^{-3}$ mbar V=1500 V (150 W)

alent to a Cobalt based structure compatible with a Bernal poliedral [5]. No variation in amorphous behavior is shown in dependence of thickness neither on tested growth parameters in both sputtering systems and we do not observe the presence of columnar growth. The most interesting aspect is the variation of the surface morphology in dependence on the films thickness and growth characteristics. In agreement with classical models [54, 55] we observed a variation of roughness and of grains size through AFM measurements. The most evident difference is between samples that were grown by rf sputtering at the two different pressures. In Figure 3.6 two different 100 nm thick sample grown through rf sputtering at the same power 150 W and at two different pressures are shown. The one grown at lower pressure has an average grain size inferior to 25 nm and a roughness inferior to 0.5 nm, while the one grown at the highest pressure has grains size between 30-60 nm and roughness near 1 nm.

At high thickness the roughness rises and the surface becomes more inhomogeneous: there are more grains aggregates and not uniformly distributed. As example in (Figure 3.7) we can see the AFM surface of two different samples grown at 1200 V (100 W), at the highest pressure, with thickness of 200 nm and 1000 nm. The roughness of the thinnest sample is 0.9 nm with a grains average size of 45 nm, while in the thickest one, the average grain size is 1.8 nm and the average grain size is 90 nm.

The samples grown through magnetron sputtering do not show even though they are grown at high powers, significant differences from samples grown through rf sputtering. As we can see in (Figure 3.8), the morphology of the two different samples is very similar, in fact the grains size in rf sputtering sample changes from 30 to 60 nm, while in magnetron one the grains change from 30 to 100 nm, the roughness of the two samples are very similar: 1.2 nm and 1.4 nm respectively.

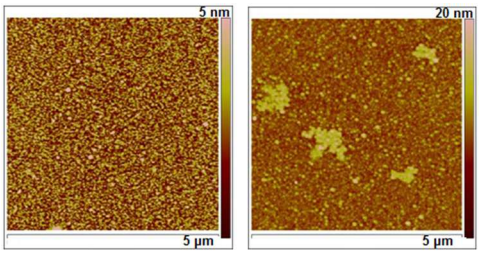

Figure 3.7: AFM signal, left: 200 nm sample grown through rf sputtering P= $1.2 \cdot 10^{-2}$ mbar V=1200 V , right: 1000 nm sample grown through rf sputtering P= $1.2 \cdot 10^{-2}$ mbar V=1200 V

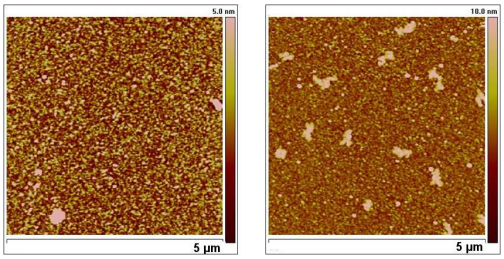

Figure 3.8: AFM signal, Left: 400 nm sample grown through rf sputtering P= $1.2 \cdot 10^{-2}$ mbar power 100 W , right: 400 nm sample grown through magnetron sputtering P= $1.2 \cdot 10^{-2}$ mbar power=1000 W

3.5.2 Magnetic properties and domains

There are two very different behaviors, the samples grown through sputtering rf. show very soft magnetic characteristics. In these samples there are not any kinds of dependence on morphologic characteristics neither on experimental growth parameters.

We observe an anisotropy of magnetic loop in film plane (figure 3.8) that depends on the direction of oscillation of substrate in front of target and it is probably related to a presence of texture in atoms induced by the direction of atoms that arrive on the substrate. The oscillation gives rise to a non-perpendicular flux that gives rise to an induced uniaxial stress anisotropy, that corresponds to a modification of the short range order [56, 57].
In samples with thickness of 100 nm we observe the presence of a very small perpendicular MFM signal Figure 3.10, that in thicker samples is not evident, perhaps this fact could be attributed to the higher surface roughness. These lines could correspond to ripple structure [27] which reflects the irregular polycrystalline-amorphous short range anisotropy nature of the films and its characteristic texture. A further confirmation is done by the presence of a pinning of domain wall due to the presence of a grain (Figure 3.10). Their orientation is

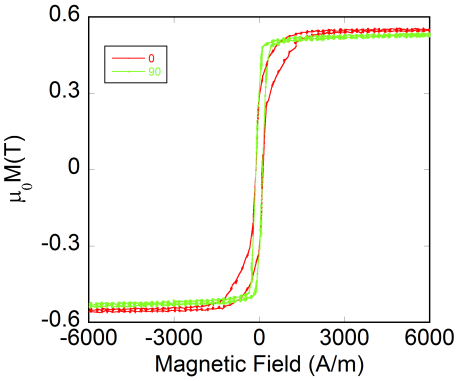

Figure 3.9: Hysteresis loop of 100 nm sample grown through rf. sputtering, in particular we observe an anisotropy in the film plane

probably related to the texture that we observed even in the in plane hysteresis loops.

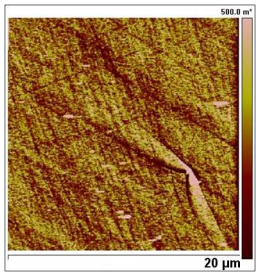

Figure 3.10: MFM domain pattern of 100 nm sample grown through rf. sputtering, in particular we can observe a domain wall pinning

Their configuration changes with sputtering growth characteristics: at highest pressure the lines density and periodicity lower with the increment of tension; at lowest pressure the lines are parallel and regular.

Samples grown through magnetron sputtering (at STMicroelectronics) show, instead, another kind of magnetic behavior. The loop shape is transcritical [58] and evidences the presence of a strong MFM perpendicular signal (figure 3.11).

The bright and dark contrasts in MFM signal are due to magnetization directed up or down of the film plane (Figure 3.11).

The magnetic coercive fields and the saturation fields are higher than ones obtained in samples grown through rf. sputtering.

In soft magnetic materials this kind of loop shape is generally due to the presence of columnar growth, to the presence of crystalline phase or to the stress induced during the film growth

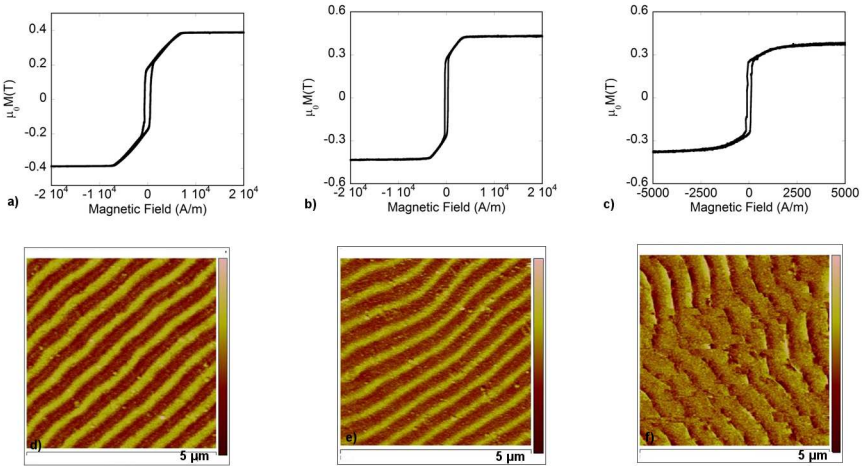

Figure 3.11: Magnetic behavior of 400 nm films grown through magnetron sputtering a) magnetic hysteresis loop of sample grown at 1000 W and corresponding MFM signal d), b) magnetic hysteresis loop of sample grown at 2000 W and corresponding MFM signal e), c) magnetic hysteresis loop of sample grown at 3000 W and corresponding MFM signal f)

[27]. We can exclude the first two hypotheses by the morphological and structural analyses so we can attribute this kind of transcritical loop shape to the presence of an induced magnetic anisotropy perpendicular to the film plane [59].

The loop shape changes with growth parameters in particular, the coercivity and saturation field lower increasing the power as we can see in Table 3.1. This behavior is due to the change

Power (W)	$H_C(A/m)$	$H_S(A/m)$	$\mu_0 M_S(T)$
1000	611 ± 18	7000 ± 200	0.40 ± 0.04
2000	333 ± 10	3500 ± 100	0.43 ± 0.04
3000	107 ± 3	2200 ± 200	0.40 ± 0.04

Table 3.1: Magnetic hysteresis loop characteristics of samples grown through magnetron sputtering in dependence of growth parameters.

of stress induced during the film growth, that probably decreases by increasing the power.

A deeper investigation can be done by studying the domain pattern in samples never magnetized show a characteristic stripe domains geometry [27]. The periodicity of stripes and their dimension depend on growth power and on shape of hysteresis loop while their orientation could be related to a deformation of substrate (as other authors report [60, 61]), even if no anisotropy in the in plane hysteresis loop is shown. As we can see in Figure 3.11 the power increment decreases the stripes size and at high power, corresponding to 3000 W, the magnetic MFM signal becomes less strong and the shape of stripe less evidence.

The effect of power is, in our opinion, similar to the effect of temperature that as many authors report [29] relief the stress in both during [62] and after the film growth [29].
We grew a sample of 1000 nm thickness in the condition of minimum stress, that is at 3000 W, as it is shown in Figure 3.12, there is an increment of the coercivity in hysteresis loop because there is an increment of stress with thickness[27, 62]. The MFM domains pattern changes shape and return similar to the pattern shown in lower power sample (see figure 3.11).

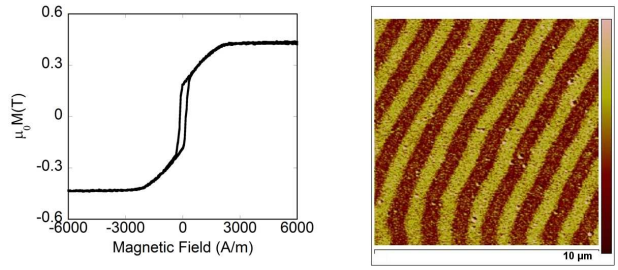

Figure 3.12: Magnetic behavior of 1000 nm film grown through magnetron sputtering: hysteresis loop at room temperature and corresponding MFM domain pattern

3.6 Discussion and micromagnetic model

All the obtained samples are amorphous and have a composition similar to the bulk massive target. In agreement with classical models we observed an evolution of surface morphology with sputtering parameters. While at low pressure the surface morphology is very flat and uniform, at higher pressure the surface is made of separated grains with open edges. This situation is due to the adsorption of inert gas on substrate and to the scattering of material atoms with inert gas ions and atoms that gives rise to a non perpendicular flux [54, 55]. The effect of power is similar to effect of temperature. In fact at low pressure its effect is to increase mobility of atoms on substrate surface, because their kinetic energy is proportional to the power applied between target and substrate. At lowest pressure the effect of the power increment is to lower the roughness, indeed the surface mobility increases and permits to obtain a very flat surface.
At highest pressure instead, the power increment increases also the kinetic energy of ions that can implant in substrate and create a less uniform surface. In this way the effect of the increase of power is opposite respect to the behavior at lowest pressure. The thickness rise makes the roughness bigger because the effect is amplified. The effect of rate is not very important in fact we observed a similar behavior even in magnetron and rf sputtering. The high power

in magnetron sputtering does not change the morphology very much, we observed the same behavior as in rf sputtering, with an increase of grain and on roughness.

The magnetic characteristics are influenced by the micro-stress induced during the film growth [63, 64]. In thin films the stress can be intrinsic or thermal, the first is induced by the growth characteristics and the second by the difference of thermal expansion between film and substrate [54, 55]. We grew films at room temperature and for that reason the most important contribute is the internal stress that can be compressive or tensile and is localized at the interface between magnetic film and substrate, its magnitude depends on many parameters, in our study we have highlighted the dependence of stress on rate, and on power.

The tensile stress in soft magnetic film with negative magnetostriction (as in our case) can give rise to the presence of an anisotropy therm perpendicular to the film plane.

In this case there are two different anisotropy terms:

the shape anisotropy that tends to orient the moments in the film plane

$$K_D = \frac{\mu_0 M_S^2}{2} \tag{3.4}$$

where M_S is the saturation magnetization.

the second term is the stress anisotropy that makes the magnetization oscillating out of the film plane

$$K_\perp = \frac{\mu_0 H_S M_S}{2} \tag{3.5}$$

where Hs is the saturation field (by applying the field parallel to the film plane) that as shown is dependent on experimental characteristics that is on the stress presence and magnitude.

The weak stripe domain pattern origins in the case in which the ratio Q between the two anisotropy constant is less than 1 but the thickness is higher than the critical thickness defined in equation (1.58). This thickness depends significantly on the growth parameters and on the sputtering apparatus.

One of the main differences between the two sputtering instruments is the growth rate, in fact in rf sputtering it is lower than in magnetron one. From classical model [54, 55] we know that rate increment gives rise to a tensile stress. From the magnetic analysis of the two classes of samples we think that: the samples obtained by magnetron sputtering are in a situation of tensile stress while the one obtained by rf sputtering are in situation of less tensile stress or of compressive stress [54, 55].

We know that porous structure so as the pressure increase tends to produce tensile stress. So

observing the change in structure from low pressure to high pressure in rf sputtering we think that while at low pressure the stress is compressive, at high pressure the stress is tensile but probably is not sufficient to give rise to a rotation of magnetization out of film plane.
For that reason the observed MFM signal is a very low signal that corresponds to an in plane pattern domains. This configuration of lines can correspond to domain walls between in plane domains.
In high rate magnetron sputtering the hysteresis loop corresponds to a transcritical loop shape. The effect of tensile stress, in this case, is enough to change the direction of magnetization out of film plane. This component changes with applied power, in fact we think that the power increase has the same effect of the increase of temperature and, in that way the stress decreases.
The domain patterns that could be seen from MFM change in intensity and geometry.
For all the powers used we can consider the critical thickness value, that is the thickness above which the oscillation of magnetization out of film plane it is possible.
The critical thickness is obtained and changes from 189 nm in the case of 1000 W power to 268 in 3000 W.
This result is in agreement with experimental one.
Also the periodicity of the domain change from 540 nm for 1000 W to 630 nm for 3000 W as if the variation is mainly due to the change in stress.
The variation of stress with thickness is highlighted on the samples grown at 3000 W in this case the stress increases with thickness, but the critical thickness does not change because the saturation field does not change. There is a change in MFM domain pattern with an increment of periodicity.
An heat treatment at 400°C was done on 1000 nm sample shown in figure 3.12. After the thermal treatment, the stress is released and the magnetization lies in the film plane. The corresponding hysteresis loop does not show the transcritical loop, as shown in figure 3.13, nor a MFM signal.

3.7 Sensors and material integration

After the complete study done and described in the precedent paragraphs the material growth was direct integrated in silicon production lines, but after all the steps needed for the sensor production the magnetic characteristics were analyzed. In particular we observed a conserva-

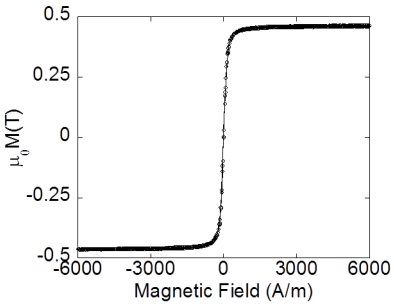

Figure 3.13: Film hysteresis loop after heat treatment at 400°C

tion of soft magnetic characteristics even after all the steps as lithography and metallizations. In figures 3.14 3.15 we can observe the two sensors geometry: Hall sensor Figure 3.14 and fluxgate Figure 3.15. The material is directly integrated in the sensors.

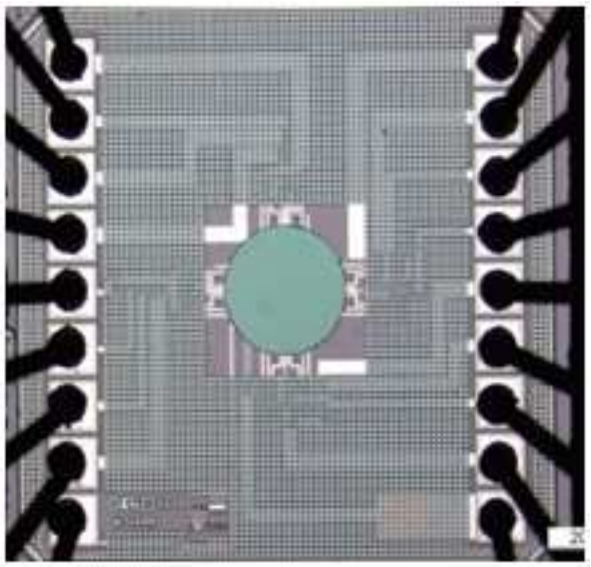

Figure 3.14: Photography of the Hall sensor

The two sensors behaviors with magnetic materials were tested and the results are shown in the Figure 3.16 and in the Figure 3.17

As we can see in Figure 3.16 a preliminary characterization of the Fluxgates prototypes shows a sensitivity larger than the simulated one. A linear behavior is observed until high bias currents of 15 mA that is sufficient for fluxgate range.

The Hall sensor behavior does not depend on frequencies and the losses are less important. In figure 3.17 the behavior of sensor output for different bias currents is shown. The Hall signal was processed with a proper instrument amplifier with an amplification of 500 and a chopping

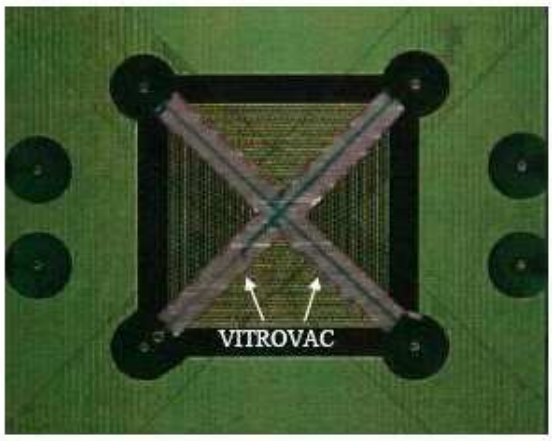

Figure 3.15: Photography of the fluxgate sensor

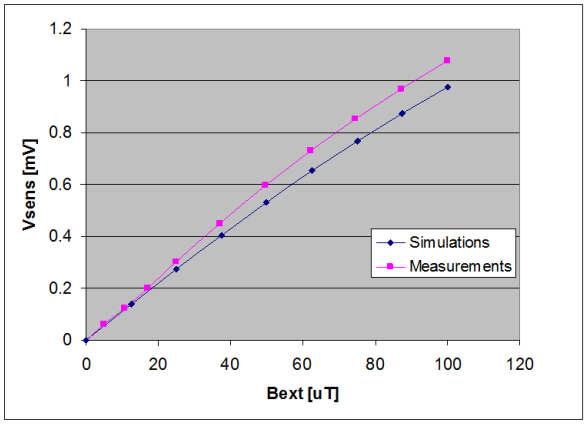

Figure 3.16: Fluxgate sensor behavior with magnetic material

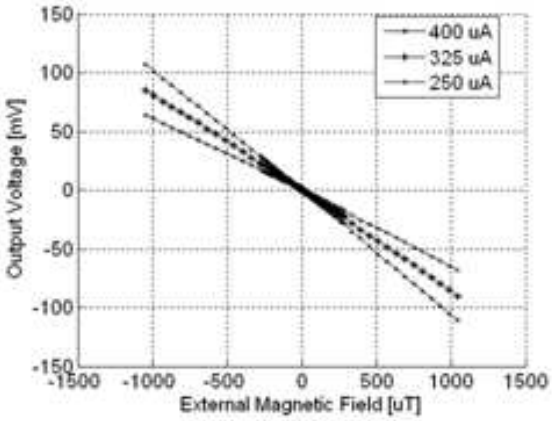

Figure 3.17: Hall sensor behavior for X applied magnetic field and changing bias currents

technique. The sensor shows a linear response with maximum output voltage of 900 mV in the range of 45 A. The saturation is reached with a magnetic field of 2 mT at about 50 A. The effect of material is to amplify the signal by a factor 10.5.

Chapter 4

Magnetic nanoparticles

4.1 Introduction

During the last years many efforts have been devoted to the study of magnetic nanoparticles (MNPs) and nanosystems to be used as active elements in biomedicine [65] [66]. Magnetic MNPs can be used in both *in vitro* and *in vivo* applications. They can be used in *in vitro* application for the magnetic separation, due to the possibility of functionalizing the MNPs surface and, in this way, separate chemical and biological entities or manipulating cells [67, 68, 69, 70]. Magnetic separation has opened the way for new kinds of micro-sensors and lab-on-a-chip [71, 72, 73, 74, 75], in which MNPs can be isolated through a local field or manipulated by magnetic wall movement. In the *in vivo* applications they can be used as contrast agents for magnetic resonance technique [76] or other kinds of magnetic imaging, as for example magnetic particle imaging, in which the non linearity of magnetic hysteresis loop is exploited [77]. They can be used as magnetic nanovectors for delivery a drug loaded on MNPs surface; in this case they are attracted toward a specific body part and there immobilized by the application of a local magnetic field gradient that can be applied externally or through an internal stent [78, 79, 80]. Finally MNPs can be used as magnetic actuators for magnetic hyperthermia for new cancer cure [81, 82]. In this chapter I am going to show the main results we have obtained on MNPs systems with properties optimized for different applications.

4.2 An overview of biomedical applications

A brief overview of the most common applications of MNPs precedes the results presentation. In particular we have studied MNPs for magnetic separation and hyperthermia.

4.2.1 Magnetic separation

After being suitably functionalized MNPs are dispersed in a fluid containing the chemical or biological entities to be separated or analyzed. If we apply a magnetic field gradient by a conventional magnet, the MNPs are separated, and then the supernatant can be removed (see figure 4.1). This method has slow accumulation rates and to increase the separator efficiency

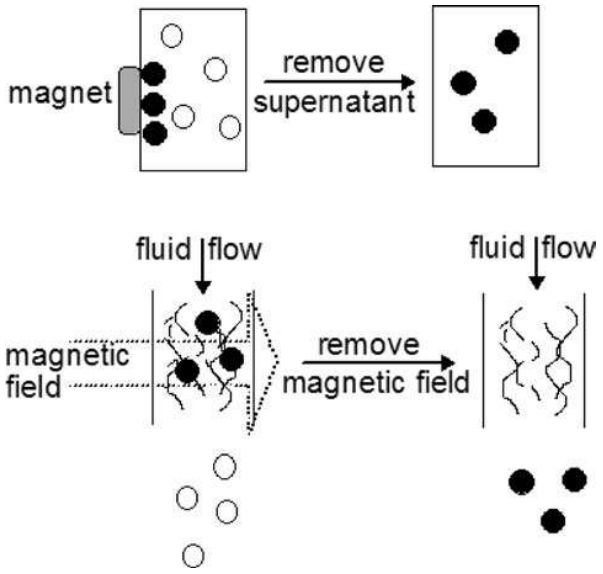

Figure 4.1: Magnetic separation technique from [83]

it is useful to produce regions of high magnetic field gradient for example with a magnetizable matrix of wires or beads [84] and to pump the magnetically tagged fluid through the column in which the magnetic field is applied (see 4.1). Due to the problems deriving from the absorption of the magnetic particles in the wires matrix, an alternative way has been proposed based on the use of specifically designed field gradient systems, such as a quadrupolar arrangement [83]. Other general requirements of MNPs are their dispersibility in polar solvent in which usually the entities are, and the superparamagnetic behavior at room temperature in order to avoid their aggregation.

A simple mathematical model can be developed by describing the nanoparticle in water solvent as a magnetic dipole $\vec{m} = V_m\vec{M}$ where $\vec{M}$ and V_m are the magnetization and the volume respectively, $M = \Delta\chi H$ with $\Delta\chi = \chi_m - \chi_w$ that is the effective susceptibility of the particle relative to the water. In the presence of an external magnetic field gradient, the MNPs are attracted by a force:

$$\vec{F}_m = (\vec{m}\cdot\vec{\nabla})\vec{B} = \frac{\Delta\chi V_m}{\mu_0}\left(\vec{B}\cdot\vec{\nabla}\right)\vec{B} \tag{4.1}$$

The force 4.1 has to overcome the hydrodynamic drag force on nanoparticle,

$$F_d = 6\pi\eta R_m \Delta v \tag{4.2}$$

where η is the viscosity of the medium, R_m is the radius of the magnetic particle, Δv is the difference between velocity of water and the marked entities.

4.2.2 Magnetically driven drug delivery

In order to avoid the chemiotherapy drugs distribution in healthy cells, the possibility of new therapeutic protocols able to distribute the drugs only to the target tumor cells has been proposed from the late 1970s, in particular the use of magnetic carriers to target specific sites within the body [85, 86]. The use of nanovectors can reduce the amount of systemic distribution of the cytotoxic drug, and reduce the dosage. The drugs are carried by MNP vector that has to be biocompatible and then the nanosystem is injected into the patient via the circulatory system. Magnetic field gradients are used to drive the complex at a specific target site within the body (as shown in figure 4.2). The physical principle is similar to

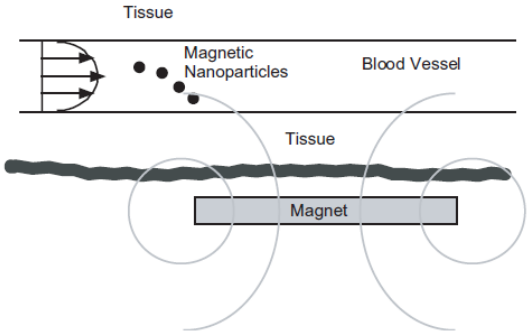

Figure 4.2: Magnetic drug deliver scheme (after [83])

magnetic separation, but more physical and physiological parameters have to be taken into accounts [83]:

- field strength and field gradient
- volumetric and magnetic properties of the particles
- ferrofluid concentration
- blood flow rate
- infusion route

- circulation time
- tissue depth to the target site
- strength of the drug/carrier binding
- tumor volume

When the target is reached then the drug can be released by exploiting different processes such as enzymatic activity or by changes in physiological conditions such as pH, osmolality, or temperature [83].

4.2.3 Magnetic resonant imaging and magnetic particle imaging

The MNPs can be used as contrast agents for magnetic resonance imaging (MRI). In presence of a large magnetic field the hydrogen nuclei present in a water molecule, align parallel to external field, then a perpendicular time-varying magnetic field is applied in a pulsed sequence, of duration sufficient to have a coherent response. The frequency of magnetic field is a resonant frequency that corresponds to the Larmor precession frequency $\omega_0 = \gamma B_0$ of the protons where B_0 is the applied magnetic field and γ is the gyromagnetic ratio (for H protons the $\gamma = 2.6 \cdot 10^8 rads^{-1}T^{-1}$), so if the applied field is $B_0 = 1T$ the Larmor precession frequency corresponds to a radio frequency $42.57MHz$. The relaxation of the coherent response is measured through the induced currents in pickup coils. A scheme of the physical behavior is shown in figure 4.3. If the magnetic field B_0 is applied in z-direction then we can describe the relaxation of magnetization when the perpendicular field is removed as

$$m_z = m\left(1 - e^{-t/T_1}\right) \tag{4.3}$$

and

$$m_{xy} = msen\left(\omega_0 t + \varphi\right) e^{-t/T_2} \tag{4.4}$$

where φ is the phase and T_1 and T_2 are the longitudinal (or spinlattice) and transverse (or spinspin) relaxation times. The longitudinal relaxation is related to a loss of energy, to its surrounding and is a measure of the dipolar coupling of the proton moments to the lattice, while the relaxation in the xy-plane is rapid, and is due to loss of phase coherence caused by the magnetic interactions between protons. In presence of local magnetic inhomogeneity the relaxation time T_2 changes in T_2^*:

$$\frac{1}{T_2^*} = \frac{1}{T_2} + \gamma\frac{\Delta B_0}{2} \tag{4.5}$$

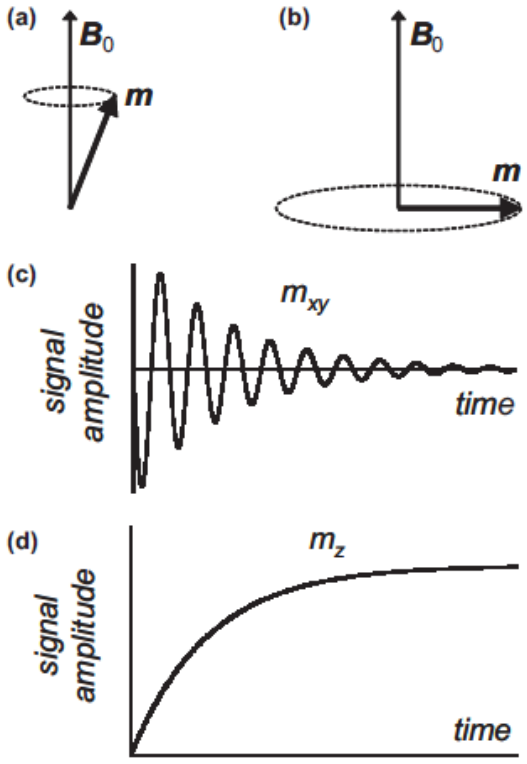

Figure 4.3: MRI signal of an ensemble of protons, we can distinguish two parts: a) the net moment precesses around B_0. In (b) the field perpendicular to B_0 is applied. In (c) and (d) the oscillating perpendicular field is removed at time zero, the in-plane (c) and longitudinal (d) moments relax back to their initial values [83].

The magnetic contrast agents shorten the two relaxation times T_1 and T_2. The most commonly used contrast agents are gadolinium ion complexes, but also superparamagnetic nanoparticles are today commercially available. The effect of superparamagnetic nanoparticles is to perturb field which leads and to a shortening of T_2 as shown in figure 4.4

There is a different behavior of MNPs in dependence of size effect: MNPs with diameters of 30 nm or more are rapidly collected by the liver and spleen, while particles with sizes of 10 nm or less are not so easily recognized. The particles with size lower than 10 nm can circulate in blood for longer time than bigger one and are collected by reticuloendothelial cells throughout the body, so they can be used to visualize the vascular system, and the central nervous system. Tumor cells do not have the reticuloendothelial system , so their signals are not changed by the contrast agents [83].

A second type of magnetic imaging that has been particular studied and developed in the last years is the magnetic particle imaging in which the non linearity of hysteresis loop is

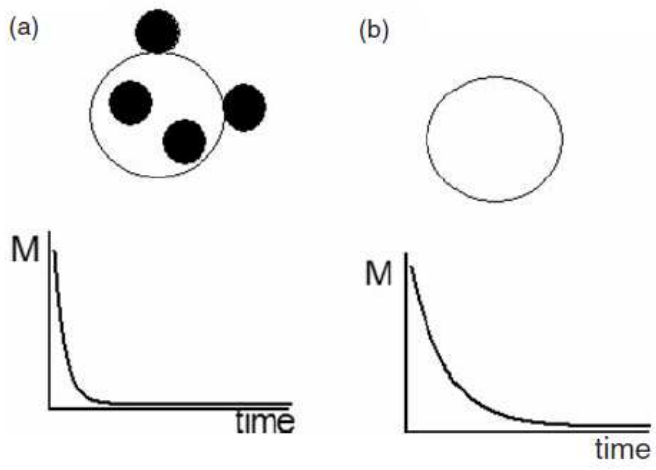

Figure 4.4: a) MRI signal with MNPs contrast agent, b) magnetic signal without magnetic contrast agent from [83]

used [77]. This imaging technique was introduced by Gleich and Weizenecker in 2005 [87] and it consists in the measurement of the spatial distribution of superparamagnetic iron oxide nanoparticles. A time varying magnetic field $H_{ac}(t) = H_0 sin(2\pi f_0 t)$ is applied to the MNPs and a signal is detected by means of a pickup coil. It has the possibility to carry out a very good and fast three-dimensional real time in vivo experiments, an example is given in the article [88] in which a beating mouse heart is shown. The detected signal is proportional to the time derivative of magnetization as shown in equation 4.6 that for its nonlinearity contains harmonics proportional to the excitation frequency f_0 [77]

$$u(t) = -\mu_0 \int_V \frac{H_r(x)}{i_0} \frac{\partial}{\partial t} M(x,t) dV \tag{4.6}$$

where μ_0 is the vacuum permeability, V the sample volume, $H_r(x)$ the magnetic field the pickup coil would generate, if it is driven by a current i_0.

In order to detect the spatial nanoparticles distribution, a static magnetic field gradient H_{dc} is superimposed so that the total applied field is $H(t) = H_{dc} + H_{ac}(t)$. In a local point the magnitude of the static field is zero (field-free point FFP) and increases linearly in all directions. Only in the FFP point the signal is different from zero, because at all other locations the magnetization is saturated due to the presence of the static field. If the position of FFP is moved then the particles distribution can be controlled. The physical principle is presented in figure 4.5.

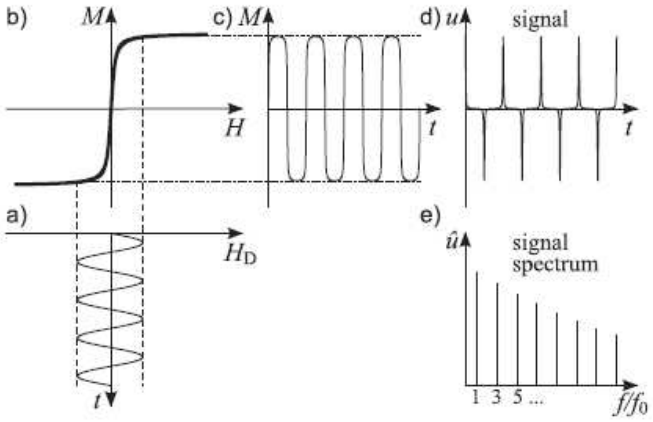

Figure 4.5: MPI: (a) applied time-varying magnetic field (b)Superparamagnetic nanoparticles behavior. (c) Signal induced in the receive coil (d), (e)frequency harmonics (after [77])

4.2.4 Magnetic hyperthermia

One of the most interesting application is the magnetic hyperthermia. MNPs are mediator of heat transfer when a radio-frequency magnetic field is applied. The local tissue temperature has to be higher than 42°C but lower than 47°C for almost 30 min, in this way the cancer cells die, while the healthy ones are not affected. The product of applied magnetic field and frequency has to be lower than a specific value $4.85 \cdot 10^8 A/ms$ [89]. These parameters have to be controlled because of peripheral and skeletal muscles, possible cardiac stimulation and arrhythmia, and non-specific inductive heating of tissue, in fact the frequencies and amplitudes must be $f = 0.05 - 1.2MHz$ and $H = 0 - 15kAm^{-1}$ [83]. The nanoparticles can be directly injected in tumor or can be injected through intravascular administration or antibody targeting. This method is not efficient enough when applied alone [90], even if for certain types of cancer, it is more suitable than the conventional treatments of radiotherapy and chemotherapy; in particular when the tumor is located close to vital organs or is drug resistant. Sometimes it is used together with chemotherapy, in fact below 43°C, it does not directly cause cell death but can increase the effectiveness of certain chemotherapy drugs that are more active at higher temperatures, and in this way they require a lower dose.
Radiotherapy can also be used with hyperthermia [91].
The ability of a magnetic material to be an hyperthermia mediator depends on many different parameters and the mechanism of heating is not well understood and can be due to losses in a hysteresis cycle, susceptibility loss, or frictional heating due to particle rotation in a liquid

environment. When a magnetic moment is exposed to a field there exists a magnetostatic energy and in order to reduce its magnetostatic energy it rotates to align with the field. If a low field strength is applied at a high frequency the moment can not follow the field and heat is generated due to this phase lag and also to frictional effects.

Mechanism of heat transfer

If we consider multidomains MNPs, the effects of heat transfer are related to the mechanism of hysteresis loop, as wall movement. The amount of heat generated per unit volume P_{FM} is given by the frequency f multiplied by the area of the hysteresis loop:

$$P_{FM} = \mu_0 f \oint H dM \tag{4.7}$$

For ferromagnetic particles well above the superparamagnetic size limit the P_{FM} can be approximately determined from quasi-static measurements of the hysteresis loop. The re-orientation and growth of spontaneously magnetized domains within a given ferromagnetic particle depends on both microstructural features such as vacancies, impurities or grain boundaries, and intrinsic features such as the magnetocrystalline anisotropy as well as the shape and size of the particle. If we consider instead single domain nanoparticles near to superparamagnetic size we can identify two mechanisms: hysteresis looses, relaxation of magnetization. The time dependence of the magnetization when an alternating field is applied leads to a frequency dependence of hysteresis loss. The remanence and the coercivity increase at high sweep-rate, increasing loop squareness [92, 93, 94] and the hysteresis losses are proportional to the square of the frequency. At high frequency, in fact, some nanoparticles are not in superparamagnetic state. Therefore we can conclude that frequency of the alternating applied field is an important parameter in controlling the amount of heat produced from hysteresis losses. Another mechanism of release of heat is the physically rotation of particles in order to align their moments with an applied field. It is called Brownian relaxation and depends on hydrodynamic volume of nanoparticles V_H, on the solvent viscosity η and on temperature T [4]

$$\tau_B = \frac{3\eta V_H}{k_B T} \tag{4.8}$$

The other mechanism of relaxation of magnetization is the Néel relaxation that is due to the thermal fluctuation of magnetization at a given temperature and it is :

$$\tau_N = \frac{\sqrt{\pi}}{2} \tau_0 \frac{\Gamma}{\Gamma^{1/2}} \tag{4.9}$$

where $\Gamma = KV/k_BT$ (K anisotropy constant, T temperature). In general both the processes are present and the effective relaxation time can be written as:

$$\frac{1}{\tau} = \frac{1}{\tau_N} + \frac{1}{\tau_B} \tag{4.10}$$

As we can easily understand there is a dependence on the volume for both relaxation times, and the dependence of the relaxation times as a function of MNPs size is shown in figure 4.6. It has been shown that particles suspended in a colloidal ferrofluid have a reduced

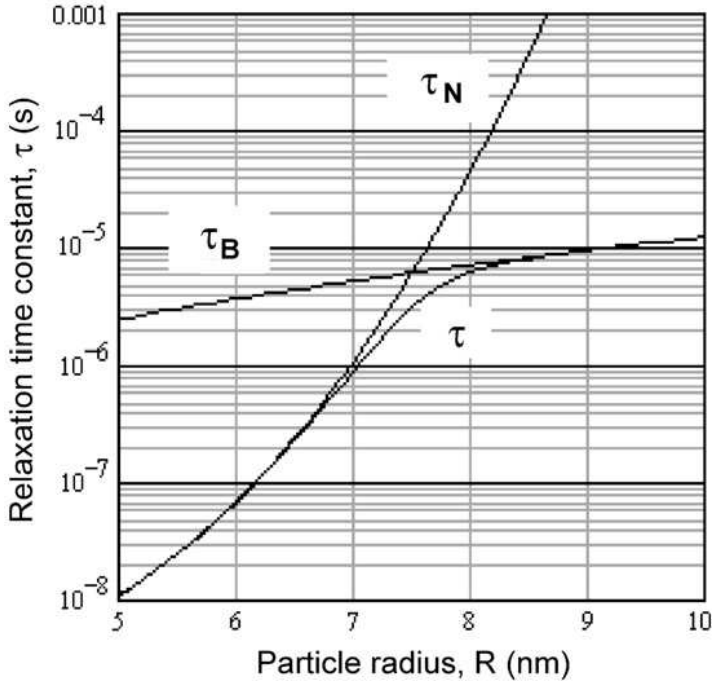

Figure 4.6: Time constants as a function of particle size for magnetite particles. After [95]

heating when Brownian relaxation is prevented, but when injected into a tumor the ability of the particles to move freely will be reduced and Brownian losses are unable to contribute to the heating. So for magnetic nanoparticles non interacting and in a single domain state we can describe the power dissipation by following the Rosensweig model [95]. If we consider the field as $H = Re(H_0 e^{(i2\pi ft)})$ where Re is the real part, H_0 is the amplitude, and $f = \omega/2\pi$ is the frequency of applied field. In a linear regime, the magnetization can be written as

$$M(t) = H_0(\chi^I cos\omega t + \chi^{II} sin\omega t) \tag{4.11}$$

where χ^I is the in-phase component, and χ^{II} the out-of-phase component of susceptibility. So by substituting the above equation in the equation (4.7) we obtain

$$P = \mu_0 \pi \chi^{II} f H_0^2 \tag{4.12}$$

The immaginary part of susceptibility χ^{II} depends on the relaxation time:

$$\chi^{II} = \frac{\omega\tau}{1+(\omega\tau)^2}\chi_0 \tag{4.13}$$

where χ_0 is the equilibrium susceptibility and in general τ is given by the equation (4.10) From the above equations we can conclude that an optimum particle size exists and yields to a maximum heating nearly independent of the applied field intensity. This size depends on the material of nanoparticle, because it depends on the anisotropy constant [95]. Figure 4.7 shows the variation of heating rate defined as $\Delta T/\Delta t$ as a function of particles size for different magnetic materials, and we can observe the variation of the maximum position. In particular higher is the anisotropy and lower is the size for which we have the maximum. The

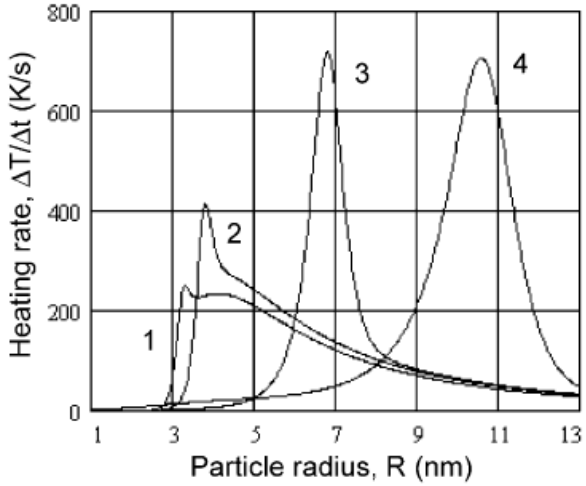

Figure 4.7: Heating rates for different MNPs. 1 Barium ferrite, 2 Cobalt ferrite, 3 Magnetite, 4 Maghemite. (f= 300 kHz, B=0.09 T). After [95].

given model is very easy but it is useful to visualize the basic phenomena that are involved in the heat transfer, even if for a correct approaching to the theory micromagnetic models or statistical simulations can be done.

Another mechanism of heating is the presence of eddy currents. The electrical conductivity of the particles induces eddy currents at the surface of the particle when a changing field is applied and they produce heat due to the resistance of the material, but they depend on the limit of penetration of the field into the particle. The eddy currents have been shown to be negligible for small particles (less than 100 nm in diameter) if the frequency of the the alternating field is also less than 10 GHz [96].

Other characteristics influence the heat rate, as MNPs size distribution the surface function-

alization [97, 98, 99, 100], the anisotropy and the interactions [101, 102, 103]; the ferrofluid parameters as the concentration of nanoparticles in solution and the solvent properties as viscosity [95, 104] .

4.3 Iron Oxides

The most important and studied materials for biomedicine application are magnetite (Fe_3O_4) and maghemite ($\gamma - Fe_2O_3$) thanks to their known biocompatibility and the possibility to control size and shape [30]. Magnemite has been studied for the variety of its physical properties.

4.3.1 Magnetite (Fe_3O_4)

Magnetite has the following composition Fe_3O_4 and has an inverse spinel crystal structure. The 32 O^{2-} ions have a cubic close packing (ccp) with a ABCABC stacking. The anions packing gives rise to two different interstitial sites: tetragonal and octahedral sites. The spatial crystal group is Fd3m and the unit cell dimension is 0.8369 [105, 106], as it is shown in figure 4.8, the tetrahedral sites are in blu (A) and the octahedral sites are in red (B).

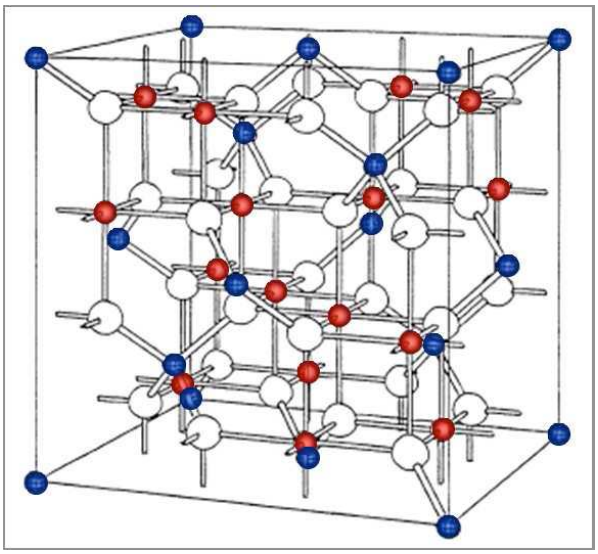

Figure 4.8: Magnetite crystal structure: ccp of oxygen anions with the tetrahedral sites that are in blu and the octahedral sites that are in red.

The tetrahedral sites are occupied by cations Fe^{3+} while the octahedral are occupied by both Fe^{2+} and Fe^{3+} randomly distributed. The inverse spinel structure can be written as $Y[XY]O_4$ where $X = Fe^{2+}$ $Y = Fe^{3+}$ and the brackets indicate octahedral sites, in this way the cations

Fe^{3+} occupy the smaller sites that are the tetrahedral sites and half of the octahedral ones. Below the Curie temperature $T_C = 850K$ [107] the magnetite is ferrimagnetic. The coupling between ions in each sublattice (A and B) is ferromagnetic, while the coupling between ions of one lattice and the other is antiferromagnetic and stronger. For this reason we can obtain the value of the saturation magnetic moment:

$$\mu_{total} = \mu(Fe^{3+}B) + \mu(Fe^{2+}B) - \mu(Fe^{3+}A) = 5\mu_B + 4\mu_B - 5\mu_B = 4\mu_B \tag{4.14}$$

The result of equation 4.14 is in good agreement with the experimental results that give 4.1 μ_B.

Verwey transition

The first observation of a phase transition as a function of temperature in magnetite was observed by Renger in 1913 on a synthetic polycrystal, by the measurement of the initial susceptibility as a function of temperature [108]. Then a maximum in the specific heat was observed at low temperature between 113 and 115 K by Okamura [109] , Parks and Kelley [110], Millar [111] and summarized by Ellefson et al [112]. The first electric measurements as a function of temperature in which the evidence of a change in resistivity was observed, were done by Okamura [109] and Verwey [113]. They observed a variation of resistivity by about a factor of 100 at the critical temperature T_V (Verwey transition temperature). At the beginning no structural transition was identified by XRD and only later the crystal structure was solved [106]. Verwey theory can explain the variation of all the structural parameters at the Verwey temperature $T_V \approx 125K$. He proposed that the Fe^{2+} and Fe^{3+} ions, above T_V, are randomly distributed over the B-sites, permitting relatively easy valency exchange by means of thermally activated fast electron hopping (see 4.15).

$$Fe^{2+} - e \rightleftharpoons Fe^{3+} \tag{4.15}$$

If the sample is cooled below the critical temperature, there is a reduction of the crystal symmetry from cubic to tetragonal and a charge ordering in a way that successive, a/4-spaced (100) lattice planes would be occupied, alternatively, by ferric and ferrous ions. In this way, above the Verwey transition the electronic conduction is described by a thermally activated hopping process between the ferrous and ferric ions in the octahedral lattice sites, and their random distribution gives rise to an isotropic conductivity [114]. Below the transition the conductivity, and can be either thermally activated or due to an hopping mechanism [115, 116].

Bickford immediately re-interpreted the low temperature phase as orthorhombic [117]. The x-ray difraction [118, 119] and, decisively, the neutron studies of Hamilton [120] confirmed this hypothesis (figure 4.9). At the end the transition to low temperature was identified as a

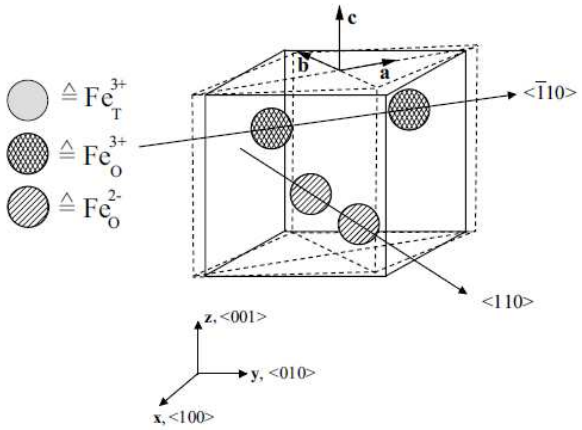

Figure 4.9: Verwey transition to an orthorombic deformation. After [114]

monoclinic [114], with a tendency to even lower symmetry, a conclusion supported by different experiments [114]. The change in crystalline order corresponds to a change in the anisotropy constant with the variation of temperature, in fact at high temperature the cubic structure correspond to the first-order magnetocrystalline anisotropy constant of $K_1 = -1.35\ 10^4 J/m^3$ along the diagonal of cubic $< 111 >$. The anisotropy constant changes sign at low temperature, passing through an isotropic point at a temperature few degrees above the Verwey transition. Below TV , the structure changing from cubic to triclinic yields a change to uniaxial anisotropy with $< 001 >$ easy axis [117, 121, 122, 123, 124, 125].

The material is still a matter of scientific debate.

The temperature of the transition is 119-125 K in stoichiometric materials, but the presence of vacancies and impurities can modify it. If an high pressure is applied it can induce a decreased of the T_V, due to the suppression of cation ordering and delocalization of electrons [126]. The occurrence of the Verwey transition and the temperature T_V in nanosized systems is still being discussed [127, 128], and it strongly depends on the synthesis and on the nonmagnetic matrix or substrate chosen. For a given synthesis technique the final magnetic properties depends on changes in the local structure like antiphase boundaries, oxygen deficiency, and local ionic disorder. In nanostructured materials as nanoparticles and films T_V changes to lower values and under a critical size no transition is still present [125].

4.3.2 Maghemite ($\gamma - Fe_2O_3$)

Maghemite has a crystalline structure similar to magnetite, referring to magnetite cell in figure 4.8, Fe^{3+} cations are only present and vacancies are present instead of Fe^{2+}. Maghemite cubic cell parameter was determined by Hagg(1935) as $a = 0.834nm$. The maghemite cell contains 32 O^{2-} anions in a ccp structure similar to magnetite, $21 \cdot \frac{1}{3}$ Fe^{3+} and $2 \cdot \frac{1}{3}$ vacancies. The tetrahedral interstitials sites and a part of the octahedral sites are occupied by Fe^{3+}, while the octahedral sites that in magnetite are occupied by ions Fe^{2+} in maghemite are not occupied at all. The space group is the same of magnetite $Fd3m$. In highly crystalline maghemite a vacancies superstructure is shown. In nanoparticles no vacancies order is present for particles with size lower than 5 nm [129]. By heat treatment in oxygen atmosphere the magnetite transforms into maghemite as can be easily understood in the phase diagram shown in figure 4.10. Under the Curie temperature $T_C = 863 - 945K$ [5] the material is ferrimagnetic and has

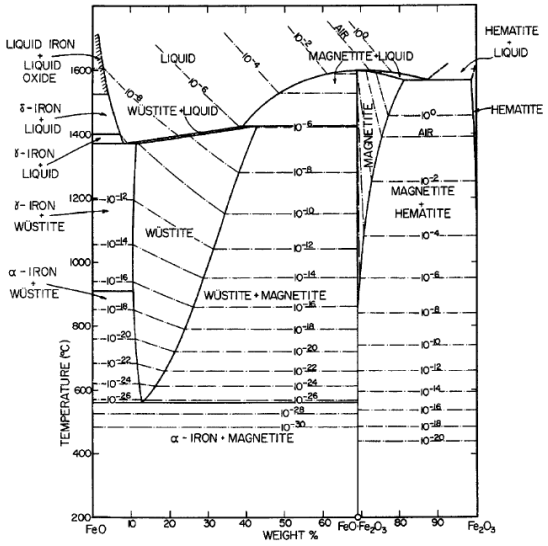

Figure 4.10: Magnetite phase diagram after [130]

an anisotropy constant $K_1 = -4.7 \cdot 10^3 J/m^3$ [105] along the $< 110 >$.

4.3.3 Hematite ($\alpha - Fe_2O_3$)

Hematite is isostructural to corundum and shows only trivalent iron ions, as in maghemite. The unit cell is hexagonal with $a = 0.5034\ nm$ and $c = 1.375\ nm$ [131]. The oxygen ions are in a hcp structure stacked along the [001] direction. Two thirds of the sites are filled with Fe^{3+} ions arranged with two filled sites followed by a vacancy. The space group is

$R\bar{3}d$. Above the Curie temperature $T_C = 956K$ the hematite is paramagnetic [105], while at room temperature it is weakly ferromagnetic and becomes antiferromagnetic below the Morin temperature $T_M = 260K$.
The spin structure is shown in figure 4.11.

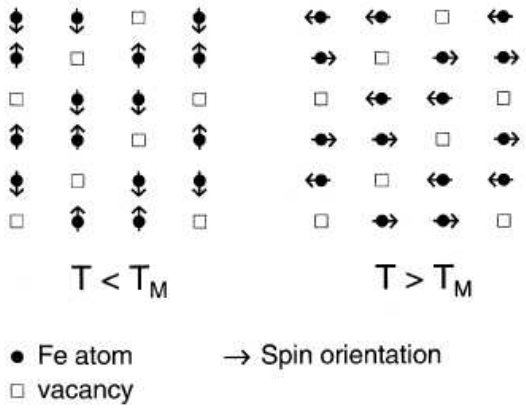

Figure 4.11: Morin transition in hematite from [105]

In the basal plane there are two sublatteces that are interpenetrating and with an antiferromagnetic coupling, but above the Morin temperature the spins are not exactly antiparallel, they have a canting angle $< 0.1°$ and a weak ferromagnetic interaction is present. At T_M the dipolar anisotropy causes the electron spins to orient from the basal plane to an angle of 7° to the c-axis and in this case the spins are exactly antiparallel, the material is antiferromagnetic. The magnetic behavior depends on crystallinity and on size, the Morin temperature was found to decrease linearly with size [105].

4.3.4 Wustite ($Fe_{1-x}O$)

FeO structure is not stable at low pressure and at pressure higher than 10MPa, but a phase stable deficient cations exits as $Fe_{1-x}O$ (where $x = 0.83 - 0.95$). FeO has an NaCl defective structure, that can be seen as an interpenetrating face center cubic structure of Fe^{2+} and O^{2-}, the cell parameter changes as a function of the present vacances in the range $a = 0.428 - 0.431\,nm$ [105]. In another way the structure could be described as a ccp arrangement of anions along the [111] direction, and planes of cations are intercalated and the planes of cations alternate with the planes of anions (see figure 4.12). The iron ions, are mostly in the octahedral sites, with a small proportion of Fe^{3+} in the tetrahedral sites.

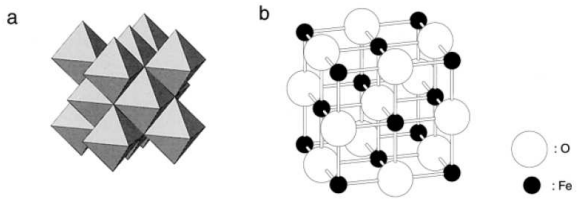

Figure 4.12: Wustite structure after [105]

Wustite is paramagnetic at temperatures above the Néel temperature $T_N = 203 - 211K$ and below it is antiferromagnetic. The spins are ferromagnetic ordered along the (111) plane and parallel to the [111] axis. Each plane is antiferromagnetic coupled with its neighbor planes.

4.4 Clusters of magnetite nanoparticles for magnetic separation

4.4.1 Introduction

At the beginning of this activity we studied diphenyl coated magnetite nanoparticles (see figure 4.13) to be used for solid phase extraction for the determination of polycyclic aromatic hydrocarbons in urine samples.

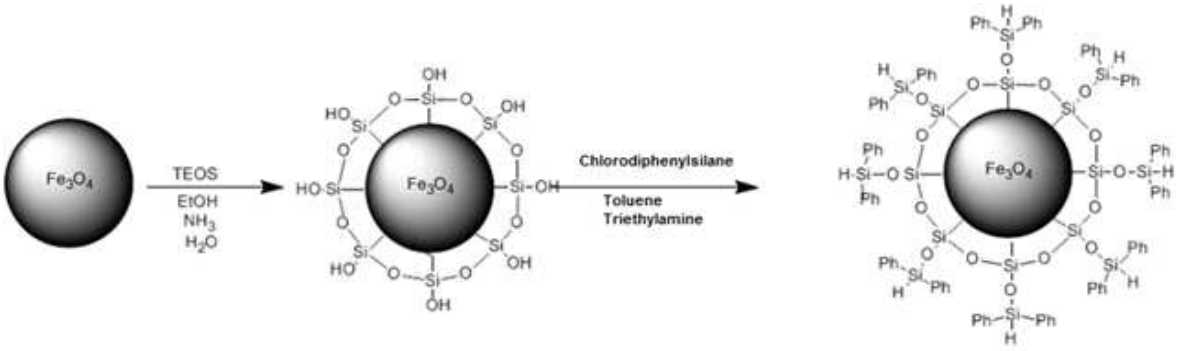

Figure 4.13: Schematic representation of the functionalization process.

4.4.2 Magnetic and structural characteristics of nanoparticles

Fe oxide MNPs with an average size of 4 nm have been obtained through solvo-thermal decomposition technique [132, 133, 134] as shown in figure 4.14 by the group of Prof. Bianchi (Chemistry Department of Parma University). As shown in figure 4.14 the nanoparticles are weakly interacting, the size is well peaked at 4 nm and the shape is spherical. The structure was assessed by means of XRD and we observed in figure 4.15 the peaks corresponding to the

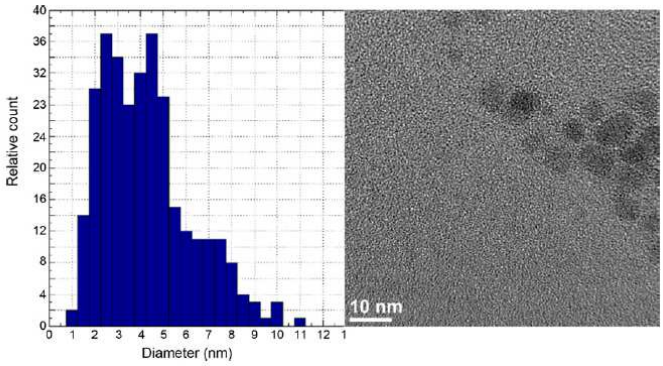

Figure 4.14: a) Nanoparticles size obtained over 324 MNPs, b) HRTEM image of MNPs.

(2 2 0), (3 1 1), (3 3 3), (4 0 0) and (4 4 0) reflections of Fe_3O_4 or $\gamma - Fe_2O_3$(JCPDS 82-1533) (figure 4.15).

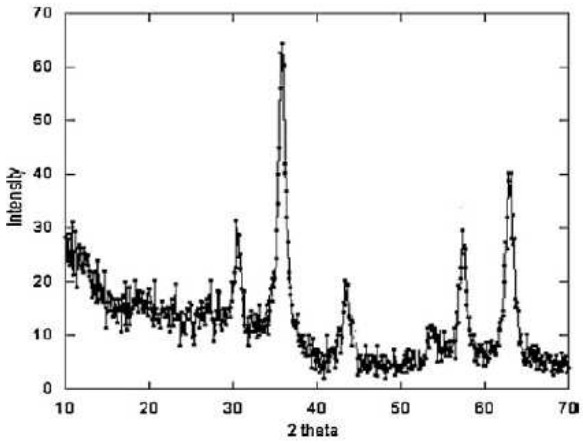

Figure 4.15: XRD of naked nanoparticles.

The ZFC-FC curves measured on the nanoparticles are shown in figure 4.16 and highlight a peak at 52 K that corresponds to the average blocking temperature of the ensemble. The nanoparticles are superparamagnetic at room temperature, but it is very difficult to collect them with a common magnet. The MNPs were then functionalized through diphenyl coating in order to obtain clusters of hundred nanometers (see figure 4.17), the surface functionalization is efficient to improve the selectivity of the extraction system. In figure 4.18 we can see the Energy Dispersive X-Ray Analysis (EDX) obtained through TEM, for Silicon and Iron present elements, we can see a very homogeneous distribution of elements in the particles and this highlights a very efficient functionalization. The magnetic characteristics of clusters are measured by VSM, at room temperature and at 30 K by applying a maximum magnetic field

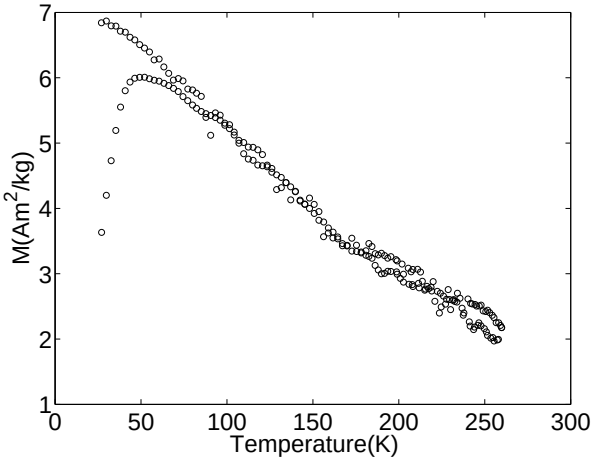

Figure 4.16: ZFC-FC obtained by VSM (Vibrating Sample Magnetometer) of naked MNPs dispersed in water with an applied field of 200 Oe

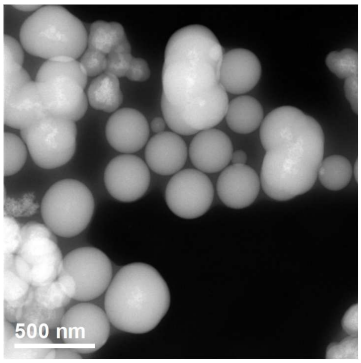

Figure 4.17: STEM image of diphenyl coated MNPs in clusters of 200 nm

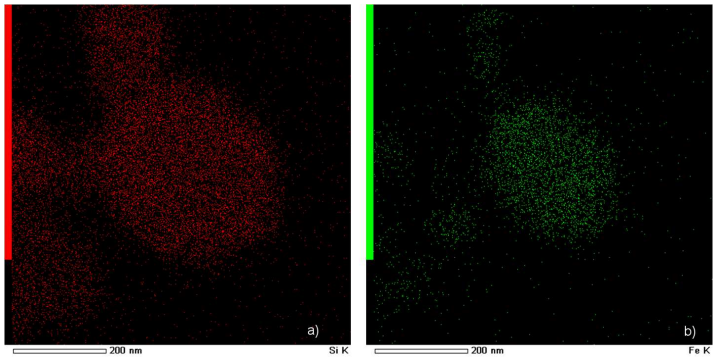

Figure 4.18: EDX map obtained in STEM mode: a) Si element distribution in cluster, b) Fe element distribution in cluster

up to 20 KOe and as a function of temperature in ZFC-FC measurements. The magnetic characteristics are different from the ones obtained in naked nanoparticles. The average blocking temperature is $T_B = 100K$ while $T_{irr} = 140K$, the difference in the two blocking temperature,

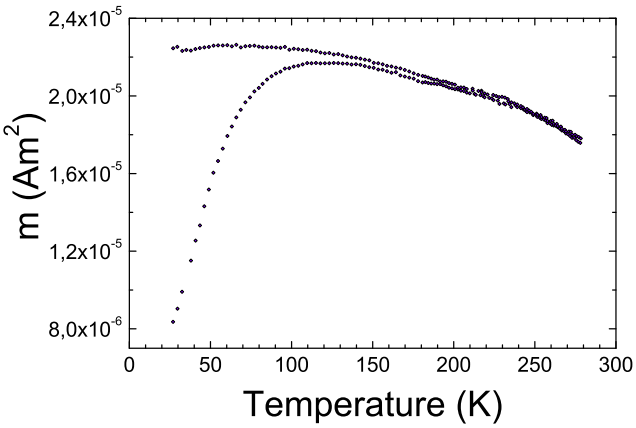

Figure 4.19: ZFC-FC measurement of diphenyl coated MNPs with an applied field of 100 Oe

before and after the functionalization is due to the variation of aggregation between nanoparticles, in fact in the second case the nanoparticles are more interacting, than in the case of ferrofluid, but they are superparamagnetic at room temperature as shown in the hysteresis loop in figure 4.20 and at 30 K the coercivity field is 140 Oe, that is typical for nanoparticles of this size.

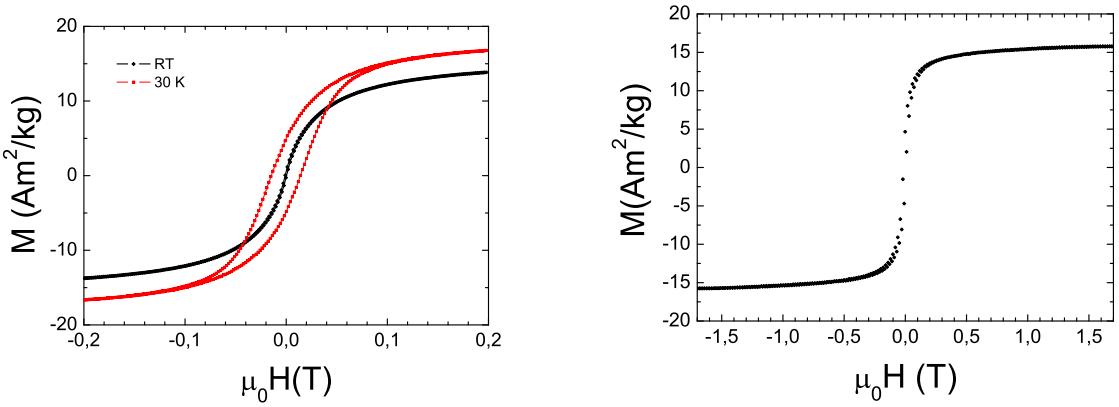

Figure 4.20: Hysteresis loop of diphenyl coated MNPs. Left: maximum magnetic field of 0.2 T at room temperature and 30 K, right: maximum magnetic field of 1.8 T

The saturation magnetization M_S of diphenyl-coated nanoparticles was evaluated from the loop measured up to 1.8 T (figure 4.20). The value is $16\,Am^2/kg$ at RT, by taking into account

the Fe-oxide mass obtained from thermogravimetric analysis. This low value can be due to an underestimation of the non-magnetic mass in the measured sample. Furthermore, the high surface-to-volume ratio of the nanoparticles can be partially responsible for the reduced magnetization. However the magnetization is sufficient to effectively isolate the nanoparticles from the matrix solution by means of an external magnetic field

4.4.3 Magnetic separation

Diphenil coated MNPs form clusters of 200 nm, and have been used as solid-phase extraction sorbent for the determination of polycyclic aromatic hydrocarbons in urine samples. After the activation of surface (done in methanol and distilled water) the clusters were dispersed into 800 μl of blank urine with a known amounts of analytes. The mixture was sonicated in order to avoid particles precipitation and, after a very short time, that was tested from 5 to 15 minutes (the best choice is 5 minutes) the nanoparticles were collected through a common magnet applied externally to the test tube, as shown in figure 4.21. In this way

Figure 4.21: Left: Diphenyl Fe3O4 nanoparticles dispersed in solution, Right: MNPs collection by a magnet

the MNPs were isolated with the wanted chemical entities. In order to take out the anlytes from nanoparticles they were washed three times with a known quantity of an apolar solvent: toluene or hexane. The best choice for the extraction has been demostered to be the toulene thanks to the presence of $\pi - \pi$ interactions between the solvent and the aromatic rings of the analytes.

One known quantity of this solution was injected into the gas chromatographymass spectrometry system. After a validation technique the method was used to detect polycyclic aromatic hydrocarbons in urine samples of smokers.

4.5 Functionalized magnetite nanoparticles for hyperthermia

4.5.1 Introduction

In the following section I am going to show you the main results I have obtained about the MNPs and the role of the interactions for their possible use as magnetic hyperthermic agents. Magnetite nanoparticles were synthesized by two different chemical techniques: co-precipitation and thermal decomposition. Their magnetic, structural and morphological characteristics have been studied in order to be used as magnetic hyperthermic agents and the main results will be shown.

4.5.2 Magnetite synthesis and functionalization

The magnetic nanoparticle have been realized by the group of Prof. Bigi (Chemistry Department of Parma University). The MNPs have been obtained through co-precipitation and functionalized with a silica shell (see figure 4.22). This functionalization is usually done in order to reduce the aggregation and to allow drug linking. The second preparation method of

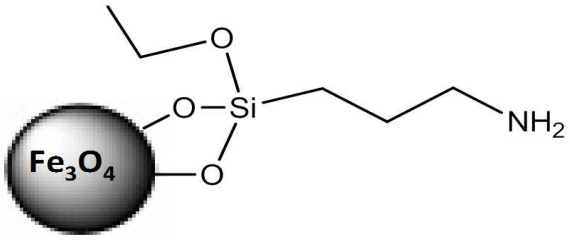

Figure 4.22: Scheme of magnetite MNP with a silica shell

MNPs has been thermal decomposition synthesis, highly stabilized in apolar solvents.

In the first method the precipitation of magnetite MNPs is easily obtained. $FeCl_2 \cdot 4H_2O$ and $FeCl_3 \cdot 6H_2O$ in molar ratio 1 : 2 were dissolved in deionized water under Argon with vigorous stirring at 85℃. NH_3 (30% in a water solution) was added in order to obtain coprecipitation at pH of 9.0. After 4 hours, the black magnetite precipitate was washed to pH=7 by deionized water [135, 136]. The obtained nanoparticles have been functionalized with APTES (aminopropyltriethoxysilane) through different processes for controlling their dispersibility in polar solvents and for possible conjugation with targeting molecules. Four samples have been obtained by co-precipitation: naked, NPM22, NPM23, NPM29. In NPM22(EtOH)the reaction of the functionaliation was done in a solution of ethanol and water in volume ratio 150/1 [137]. In NPM23(EtOH+NH3) the functionalization reaction was done in $EtOH/H_2O$ 150/1

as in NPM22 but adding NH_3 in order to change the shell thickness. IN NPM29(Tol)the functionalization reaction was done in a polar solvent, toluene but under sonication [138].
In the second case magnetite particles were synthesized using $Fe(acac)_3$ as a precursor in low bouling benzyl ether as solvent and 1,2-hexadecandiol, oleic acid, oleylammine, as surfactants. The above elements are mixed by mechanical stirrer under nitrogen in a reaction flask heated at 200°C. The MNPs obtained are then dispersed in hexane containing 10-undecynoic acid (in order to functionalised the surface) and heated at 60°C under mechanical stirring [139].
In both the chemical techniques the procedure have been studied in order to obtain nanoparticles with optimized physical characteristics, in particular narrow size distribution, well dispersity in polar solvents and absence of aggregates.

4.5.3 Chemical and structural characterization

Nanoparticles of 8 nm have been obtained through both coprecipitation and thermal decomposition, and 4 nm nanoparticles have been obtained through thermal decomposition (as shown in figure 4.23). As we can see in figure 4.23 there is a big difference between nanoparticles

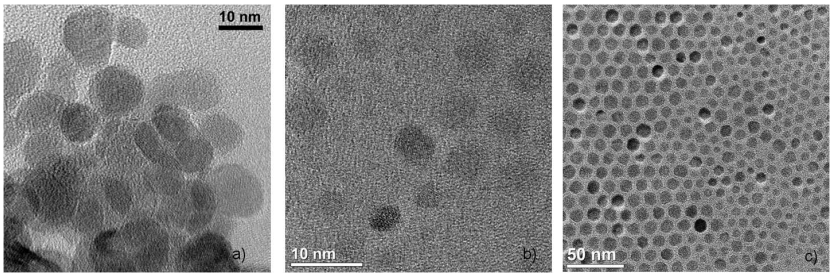

Figure 4.23: TEM images of a) 8 nm MNPs obtained by co-precipitation, b) 4 nm MNPs obtained by thermal decomposition, c) 8 nm MNPs obtained by thermal decomposition

obtained through co-precipitation and through thermal decomposition. In the first case, the nanoparticles are strongly interacting and form aggregates while in the second case they are well separated and the interactions are lower thanks to the surfactant added during the particles growth. The size distributions are well peaked at the average value, as shown in figure 4.24, even if the formation of aggregates in the naked nanoparticles obtained by co-precipitation prevents high counts.

The structure was tested by means of electron diffraction pattern. In figure 4.25 the energy-filtered ZLP (zero-loss peak) Electron Diffraction on a large area of the sample is shown and the red curve superimposed on the ring pattern is the integrated intensity profile. The positions

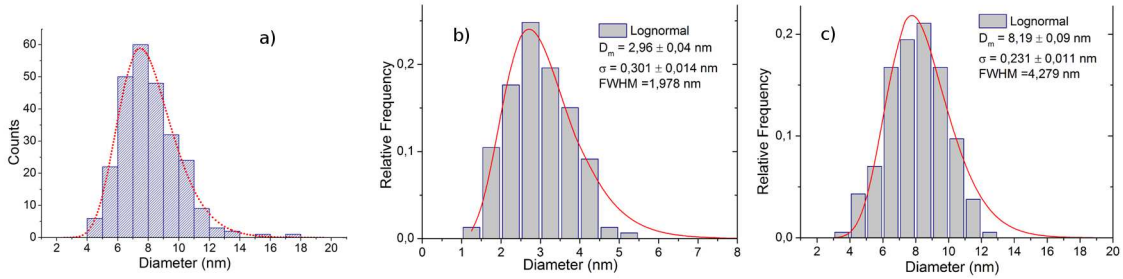

Figure 4.24: Size distribution obtained from TEM images a) Size distribution for MPNs obtained by co-precipitation with an average size of 8 nm, b) Size distribution for MNPs obtained by thermal decomposition with an average size of 4 nm, c) Size distribution for MNPs obtained by thermal decomposition with an average size of 8 nm

of the peaks correspond to magnetite/maghemite crystal structure (space group: Fd3m). In both samples the obtained phase is magnetite or maghemite. The composition of the

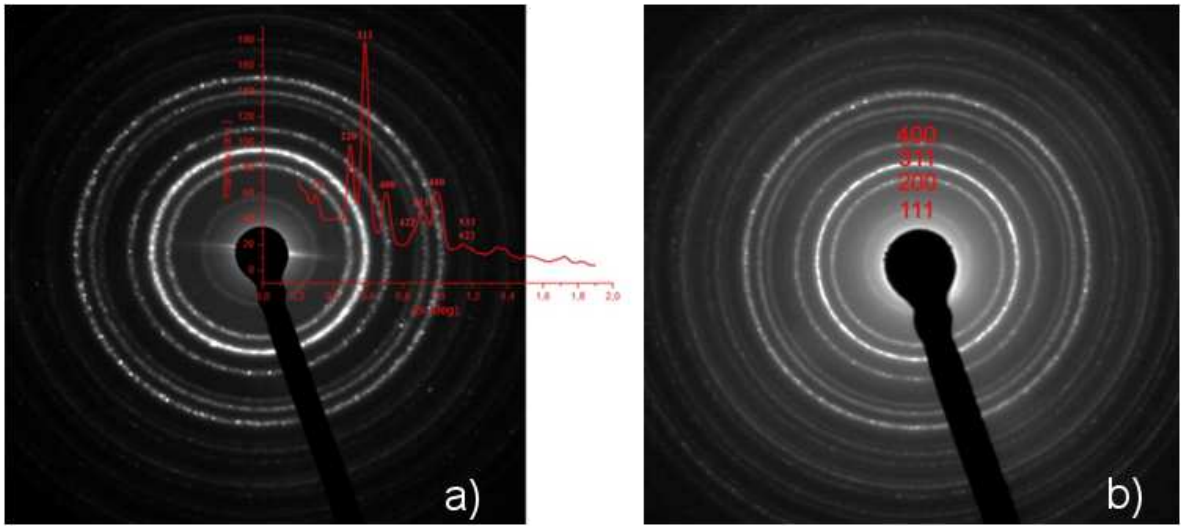

Figure 4.25: Energy-filtered ZLP (zero-loss peak) Electron Diffraction on a large area of samples, a) 8 nm size MNPs obtained by co-precipitation sample b) 8 nm size MNPs obtained by thermal decomposition sample

sample obtained by co-precipitation was also tested by means of Thermal Magnetic Analysis, i.e. the measures of the magnetic susceptibility as a function of temperature. A complete understanding of the measure is not straightforward because during the measurements the sample is heated. If the measurement is done in air we pass from magnetite to maghemite and then to hematite (as already discussed at the beginning of the chapter). If the measurement is done in an inert atmosphere as argon and maghemite is present, we transform it in magnetite. So this measurement is not exhaustive to distinguish the amount of magnetite and maghemite,

but it is useful for obtaining additional informations. A complete measurement consists in heating and cooling of sample starting from room temperature. As shown in figure 4.26, during heating the signal increases up to 200°C and this probably corresponds to the transformation from magnetite to maghemite, that is a material with a lower magnetocrystalline anisotropy, then the signal decreases probably due to the initial formation of hematite that is weakly ferromagnetic; the peak at (573 ± 5) °C corresponds to the Curie temperature of magnetite. During cooling the peak corresponding to Curie temperature of magnetite is still present, and at lower temperatures, the signal is constant and lower than in the heating curve, as a confirmation of magnetite to hematite phase transformation.

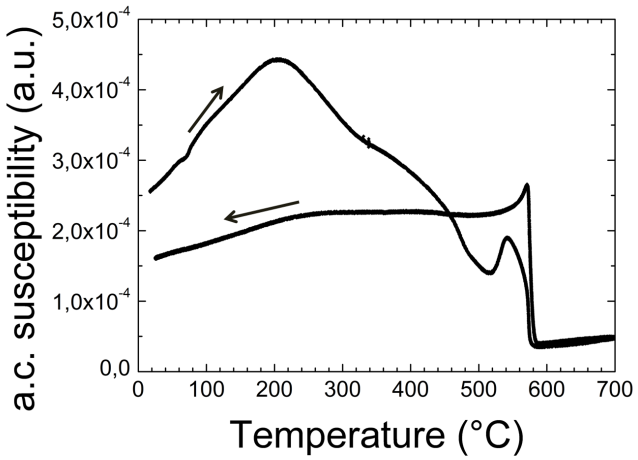

Figure 4.26: Termomagnetic Analysis of naked MNPs (obtained by co-precipitation). The measurement was done in air.

Effect of surface functionalization

The silica surface functionalization technique of MNPs influences the shell thickness and consequently affects the interactions between MNPs. In particular we can observe a shell thickness ranging from 1 to 3 nm. The nanoparticles functionalized in ethanol are strongly interacting and the shell thickness is around 1 to 2 nm and a small adding amount of NH_3 does not change the shell thickness. The MNPs functionalised in toluene have a shell of 3 nm and are less interacting. In figure we can observe the variation of shell in HRTEM image of clusters of nanoparticles functionalized with APTES. In a) and b) the thickness of the shell is about 1-2 nm, in c) in around 3 nm.

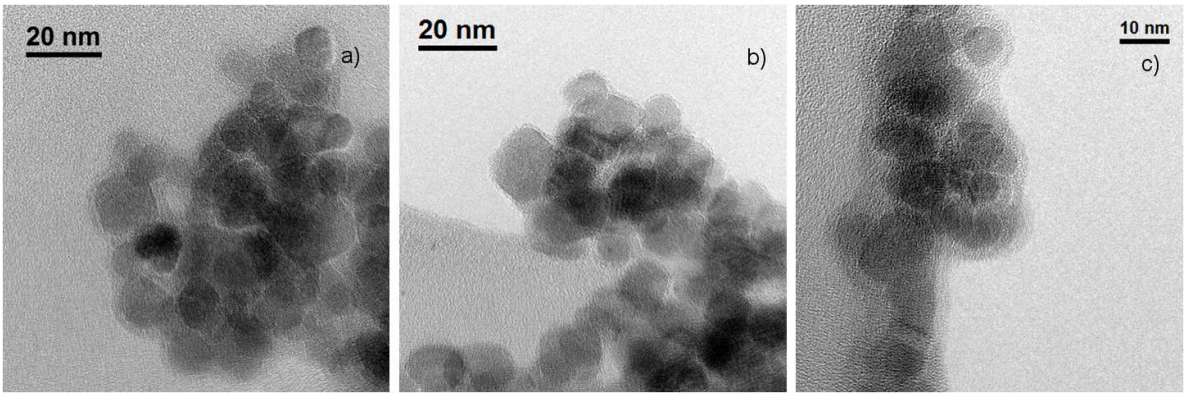

Figure 4.27: HRTEM (High resolution TEM) image of functionalized MNPs obtained by co-precipitation: a) NPM22 EtOh, b) NPM23 $EtOh + NH_3$, c) NMP29 Tol

The size of MNPs core does not change with the functionalization, as shown in size distributions in figure 4.28, where also the fitting results are reported. For small MNPs the size distribution is fitted with a log-normal function:

$$f(D) = \frac{e^{\frac{-(ln(D)-\mu)^2}{2\sigma^2}}}{\sqrt{2\pi\sigma^2}D} \tag{4.16}$$

where D id the size, σ and μ are parameters. We obtain the average size as $e^{\mu+\frac{\sigma^2}{2}}$.

This asymmetric distribution is more suitable for small MNPs than Gaussian distribution.

The bigger difference between the samples obtained by different fuctionalization is the size of the aggregates that leads to a different degree of dispersibility of nanoparticles. The first observation has been observed in STEM images reported in figure 4.29.

In NPM22 (EtOH) and NPM23 (EtOH+NH_3) there are few big aggregates, in NPM29(Tol) there are many small aggregates. In order to have a quantitative evaluation of the aggregates size in the ferrofluid we made dynamic light scattering measurements (DLS) on ferrofluid obtained by diluting the samples in water solvent. Water is the most interesting solvent because of its analogy with blood. No change in salinity has been done.
In the case of monodispersed nanoparticles the autocorrelation function is given by a singular exponential (as already discussed in the experimental chapter). In order to fit the experimental data the following model has been followed. The aggregates give a diffusion coefficient D_i contribute to the autocorrelation function with an exponential term $exp(-\Gamma_i t)$ where $\Gamma_i t = q^2 D_i$

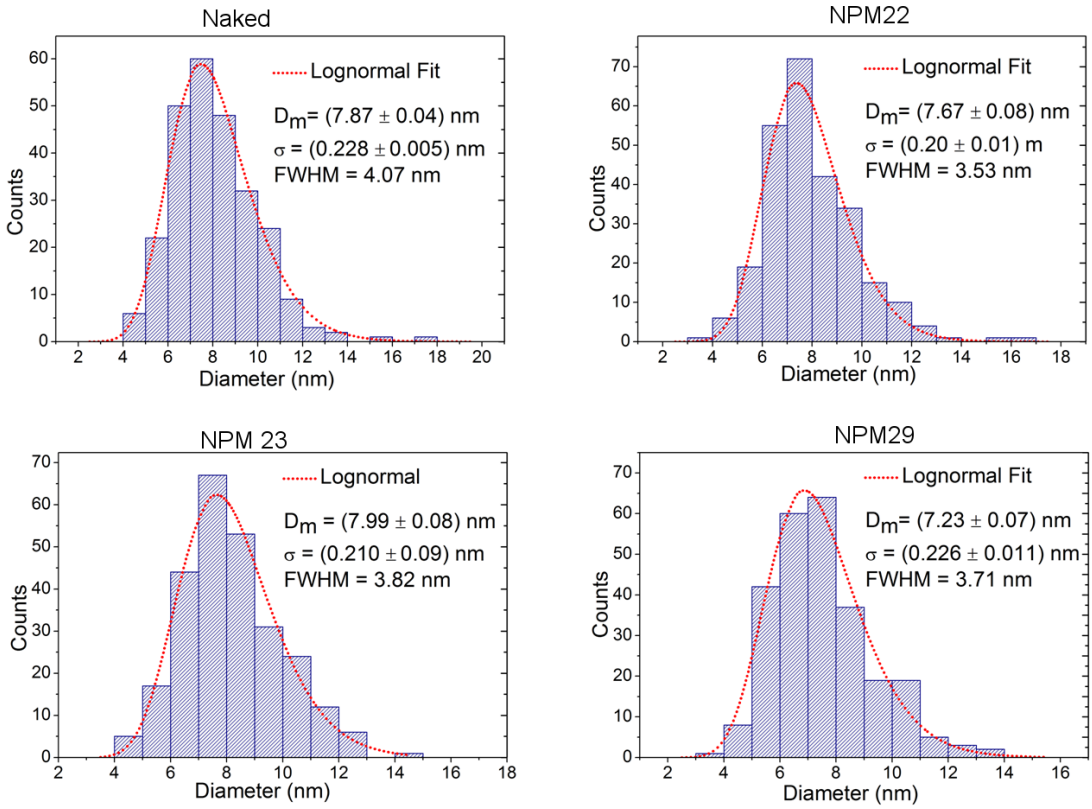

Figure 4.28: Size distribution obtained by TEM analysis on nanoparticles with different functionalizations

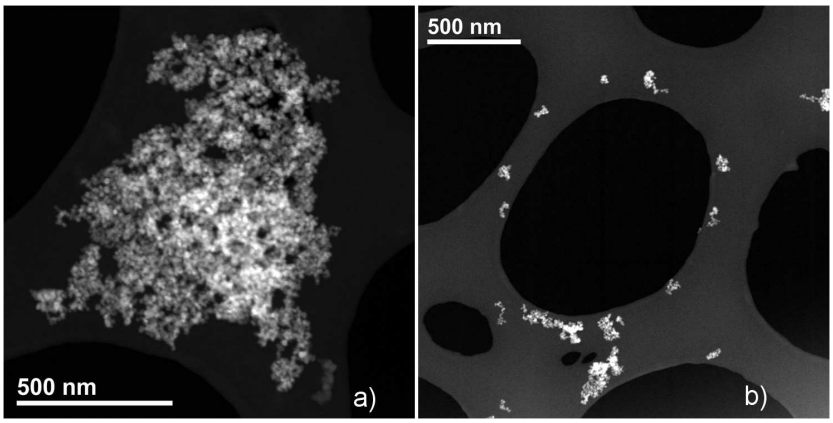

Figure 4.29: HAADF (High Angle Annular Dark Field) images obtained in STEM (Scanning Transmission electron microscopy) mode, a) NPM22 nanoparticles functionalized in ethanol, b) nanoparticles functionalized in toluene under sonication

is the opposite of the relaxation time, and the autocorrelation function can be written as

$$g^{(1)}(t) = \sum_i A_i e^{(-\Gamma_i t)} \tag{4.17}$$

A_i is a weight proportional to the contribute of different nanoparticles. A sum of exponential like in equation 4.17 can be written by introducing a *stretched exponential* like

$$f(t) = e^{-(t/\tau_r)^\beta} \tag{4.18}$$

where β is the stretching factor and τ_r is the relaxation time.
The function 4.18 describes a linear superposition of exponential [140], following the equation

$$e^{-(t)^\beta} = \int_0^\infty du\rho(u)e^{-t/u} \tag{4.19}$$

where $\rho(u)$ is the distribution of the relaxation times u. In this way the average relaxation time becomes

$$\langle\tau\rangle = \int_0^\infty e^{-(t/\tau_r)^\beta}dt = \frac{\tau_0}{\beta}\phi\left(\frac{1}{\beta}\right) \tag{4.20}$$

where ϕ is the Eulero function. For the above reason the autocorrelation function becomes:

$$g^{(1)}(t) = e^{-(t/\tau_r)^\beta} \tag{4.21}$$

and with this form we obtain g^2, an example of the fit done on naked nanoparticles is given in figure 4.30. From the fits we obtain the distributions of relaxation times by the equation (4.20)

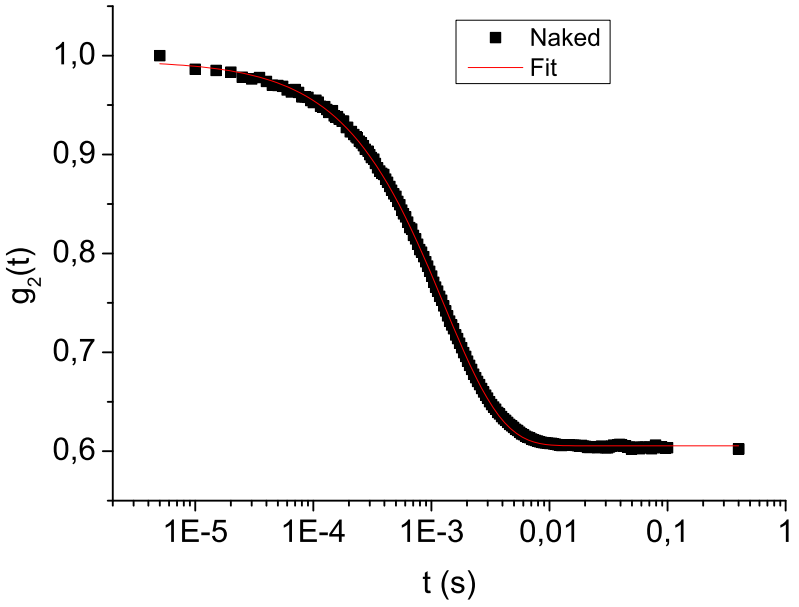

Figure 4.30: Example of fit of $g^{(2)}$ with a stretched exponential (sample NMP22)

and then the size distribution by using the equation (2.6). As we can see in the table 4.1 there

	Naked	NPM22(EtOH)	NPM23 (EtOH+NH_3)	NPM29 (Tol)
R (nm)	97	103	106	66
ΔR (nm)	40	55	55	33

Table 4.1: Aggregate sizes obtained through DLS

is a difference in the aggregates size, in sample functionalized in toluene under sonication, the aggregates size 30% lower than samples functionalised in ethanol. This behavior is a confermation of the results shown with TEM, and can be due to the effect of sonication during preparation that prevents the aggregation of nanoparticles.

4.5.4 Magnetic characterization

A complete study of magnetic characteristic has been done on both the samples series prepared by co-precipitation and by thermal decomposition. The ZFC-FC curves and the hysteresis loops at different temperatures have been measured by SQUID, AGFM and VSM magnetometers.

Nanoparticles obtained by co-precipitation

For the nanoparticles obtained by co-precipitation the ZFC-FC curves are very similar and no substantial differences can be appreciated betweeen functionalized and non functionalized MNPs. The measurements have been done on powders samples and highly concentrated ferrofluid ($10\,mg/ml$) and the results are equivalent.
The ZFC-FC measurement of naked MNPs obtained by co-precipitation is shown in figure 4.31.

We can observe a blocking temperature near the room temperature at $T_B = (250 \pm 5)\,K$, a very flat FC curve that corresponds, as I highlighted in the chapter 1, to strongly interacting MNPs. At room temperature we cannot appreciate an hysteresis, the curves are characteristic of superparamagnetic MNPs, as shown in figure 4.32.
High saturation magnetization of $M_S = (77 \pm 7)\,Am^2/kg$ is obtained, which is very high for MNPs of this size [98]. This high saturation value is due to the good crystallinity, but it could be also due to MNPs interactions which can be able to orient the surface spins parallel to each other [7, 17]. The functionalized MNPs have a saturation magnetization lower than 10%, compared to naked MNPs, and this is probably due to the weight of silica shell that we are not able to correctly evalueted. In table 4.2 the saturation magnetization values and

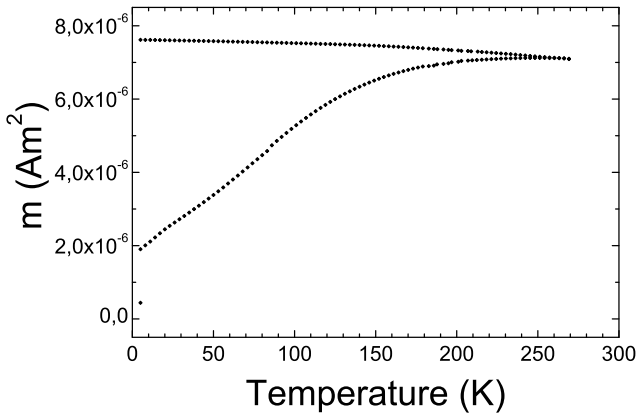

Figure 4.31: ZFC-FC of naked MNPs (obtained by co-precipitation) with an external applied field of 100 Oe

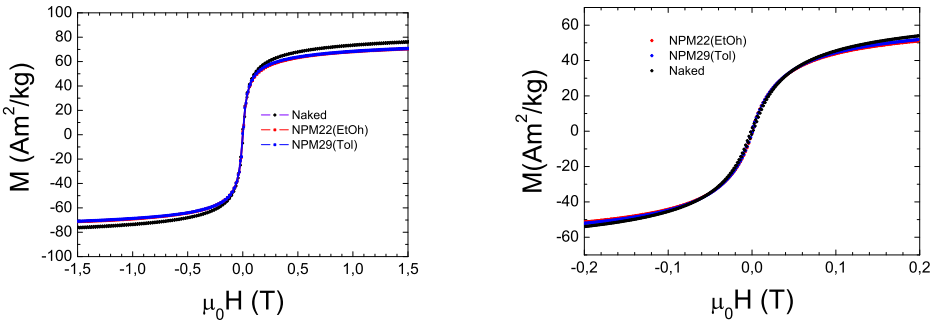

Figure 4.32: Magnetization curve of functionalized and naked nanoparticles obtained at room temperature. Left: maximum field 1.5 T, right: maximum field 0.2 T

the blocking temperatures are shown. We do not exclude the presence of a small fraction of

	Naked	NPM22(EtOH)	NPM29 (Tol)
M_S (Am^2/kg)	77±7	72±7	72±7
T_B (K)	249±5	255±5	254±5

Table 4.2: Saturation magnetization and blocking temperatures of nanoparticles obtained by co-precipitation at room temperature

blocked nanoparticles at room temperature, but this behavior can be mainly attributed to strong interactions

The low temperature hysteresis loops below the blocking temperature (at 30 K) are shown in figure 4.33 where a coercive field, typical of blocked magnetite nanoparticles can be observed

table (4.3)

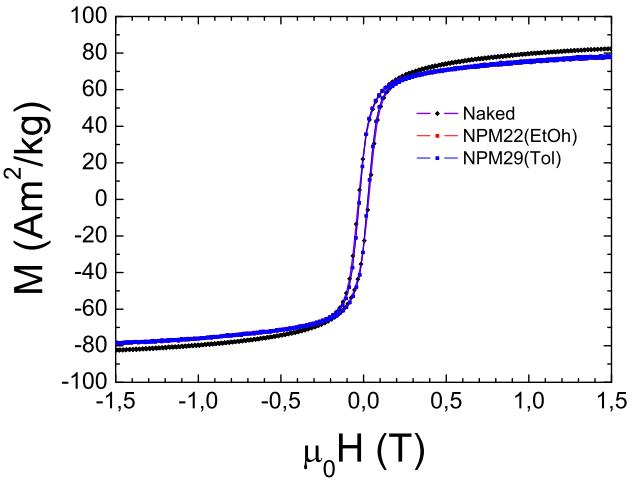

Figure 4.33: Magnetic hysteresis loops of naked and functionalized MNPs at 30 K.

	Naked	NPM22(EtOH)	NPM29 (Tol)
$\mu_0 H_C$ (T)	0.028±0.002	0.025±0.002	0.026±0.002

Table 4.3: Coercive field of nanoparticles obtained by co-precipitation at 30 K

The value reported in table 4.3 highlighted a very good crystallinity.

Nanoparticles obtained by thermal decomposition

The MNPs with size of 8 nm obtained by thermal decomposition show a different magnetic behavior, in particular the ZFC-FC curves have a very lower blocking temperature as shown in figure 4.34, and the FC curve is less flat than ZFC-FC of MNPs obtained by co-precipitation. This evidences that the nanoparticles are less interacting, thanks to the organic shell, that is added directly during the growth. The blocking temperature is 80 K and the nanoparticles are superparamagnetic at room temperature as shown in figure 4.35. The saturation magnetization is 22% lower than MNPs obtained by co-precipitation, in fact it is $M_s = (63 \pm 20) Am^2/kg$ (here we have substracted the weight of organic shell obtained by thermogravimetric analysis). This is due to the fact that the interparticles separation is increased and the dominating interaction is of dipolar origin [141, 142].

At 3 K the magnetic properties have been measured and, as we can see figure 4.36, the coercivity is 0.034 T in good agreement with the value of single domain for Fe_3O_4 particle.

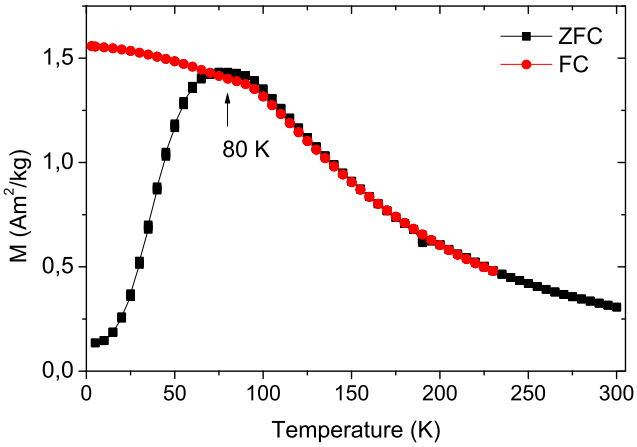

Figure 4.34: ZFC-FC of 8 nm nanoparticles (obtained by thermal decomposition) with an applied field of 10 Oe.

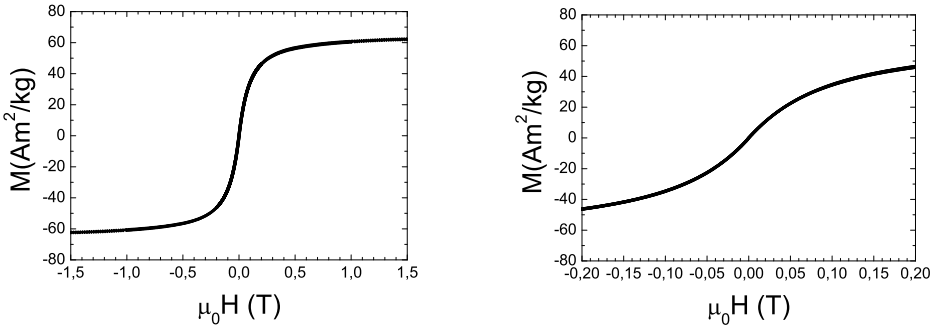

Figure 4.35: Hysteresis loop at RT of 8 nm MNPs obtained by thermal decomposition: Left: maximum field of 1.5 T, right: maximum field of 0.2 T .

Hysteresis loop is symmetric and this is a good indication of absence of frustration effect that can be due to both nanoparticles interaction, both to spin at the surface [17]. For comparison, the magnetic curve of 4 nm MNPs at room temperature is shown in figure 4.37.

It is evidence that magnetization at highest field is $(3.4 \pm 0.3) Am^2/kg$ and this value is very low respect to the bulk. The low magnetic value and Langevin like behavior reflect the small size of the MNPs, which are far from saturation at room temperature. Other effects can be also taken into account, i.e. the dead layer spins and the dipolar interactions.

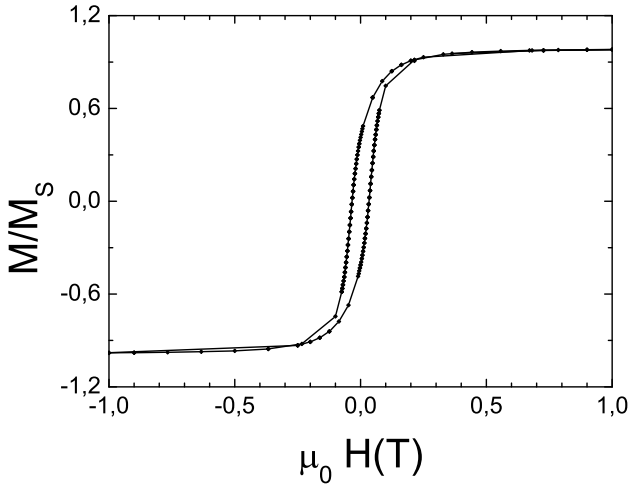

Figure 4.36: Hysteresis curve at 3 K of 8 nm MNPs obtained by thermal decomposition

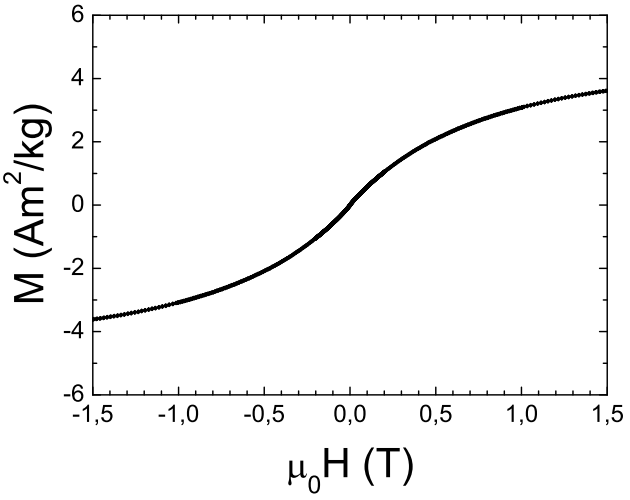

Figure 4.37: Hysteresis curve of 4 nm MNPs obtained by thermal decomposition, measured at RT.

4.5.5 Hyperthermia measurements

An hyperthermia measurement consists in applying a magnetic radio-frequency field to a colloidal solution and measuring a variation of temperature as a function of time by a optic fiber sensor (as already described in chapter 2). In our experiment we applied a field of 160 Oe at a frequency of 250 kHz. The parameter that describes the behavior of the sample is the

specific absorption rate:

$$SAR = \frac{c_{sol}\delta_{sol}}{\phi}\frac{\Delta T}{\Delta t} \tag{4.22}$$

where ΔT is the temperature variation in the time Δt, c_{sol} is the specific heat of solvent, δ_{sol} is the solvent density and ϕ is the concentration of nanoparticles in solution. The concentration of nanoparticle is in the range of 8-12 mg/ml. The characteristic variation of temperature as a function of time is shown in figure 4.38

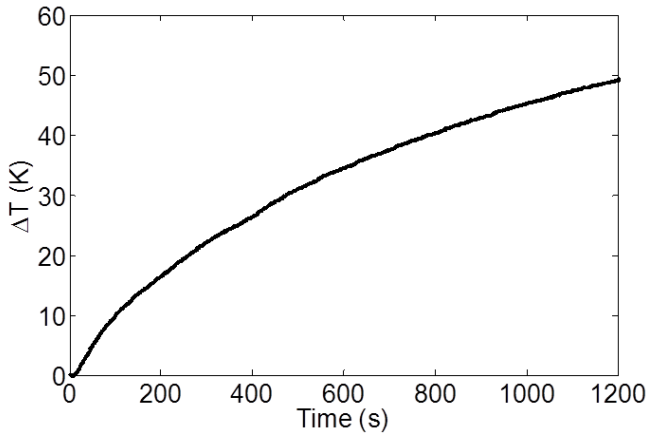

Figure 4.38: Hyperthermia measurement: variation of temperature as a function of time obtained on Naked MNPs

The SAR depends significantly on size, in fact for nanoparticles of 4 nm no significant value can be measured, while for nanoparticles of 8 nm the value is 3.4 W/g and depends significantly on interactions between nanoparticles. For MNPs obtained through co-precipitation the $SAR = 50\ W/g$ is obtained, that is one order of magnitude greater than nanoparticles obtained through thermal decomposition, even if MNPs size is the same and the crystalline phase is equal in both cases.

	Naked	NPM22(EtOH)	NPM29 (Tol)
d (nm) TEM	7.9	7.8	7.2
R (nm) DLS	96	104	66
SAR (W/g)	50	43	15

Table 4.4: SAR values obtained for functionalised nanoparticles obtained through co-precipitation, TEM size and hydrodinamic radius obtained through DLS

Then we measured all the functionalised MNPs obtained through co-precipitation and the results are shown in the table 4.4 where we can see a strong variation of SAR in dependence of the aggregates size measured by means of dynamic Light Scattering (DLS). The difference

between NPM22 and naked can be accounted by considering the weight of shell. On the other hand lower SAR can be observed for NPM29 sample that shows much smaller aggregates size. Considering the hyperthermia measurements, we can conclude that when the MNPs are aggregated, behave as if they were bigger, but not as big as the aggregate size for which we would expect a value of $200 - 300 W/g$ taking into account the models above described.

4.6 Core-shell magnetite nanoparticles

4.6.1 Introduction

In this section I am going to show the main results obtained on nanoparticles in which a core shell structure with two iron magnetic oxides is present. In particular this structure is very common in magnetite sample obtained by thermal decomposition of $Fe(acac)_3$, where usually a FeO wustite core can be synthesized by reductive decomposition of $Fe(acac)_3$ in oleic acid and oleylamine at high temperature. After the formation of a wustite core, while cooling down the solution in dry-air the Fe_3O_4 shell forms [143, 144, 145]. These MNPs are very interesting for possible biomedical applications thanks to the exchange anisotropy of the interface between the two phases.

4.6.2 Morphological characterization

The nanoparticles have been obtained through thermal decomposition by the group of Prof. Cozzoli (NNL Lecce).
The metallorganic precursor is $Fe(acac)_3$. In order to obtain two different shapes: cubic or spherical, different surfactants have been used [144, 145, 146, 147, 148, 149, 150, 151, 152]. Cubic nanoparticles have size in the range 11-26 nm, spherical nanoparticles have size in the range 9-28 nm. In both cases MNPs are very well dispersed in chloroform and have a very narrow distribution size (figure 4.39). The two characteristic shapes are shown in figure 4.39, and as we can see they are low interacting.

4.6.3 Magnetic characterization

In order to evaluate the presence of the two phases (wustite and magnetite) two different kinds of measurements have been done: ZFC-FC measurements and hysteresis loops at low temperature after having cooled the sample in an applied field of 5 T (FC loop). This measurement is very useful to identify the presence of an exchange bias effect; in fact, as already

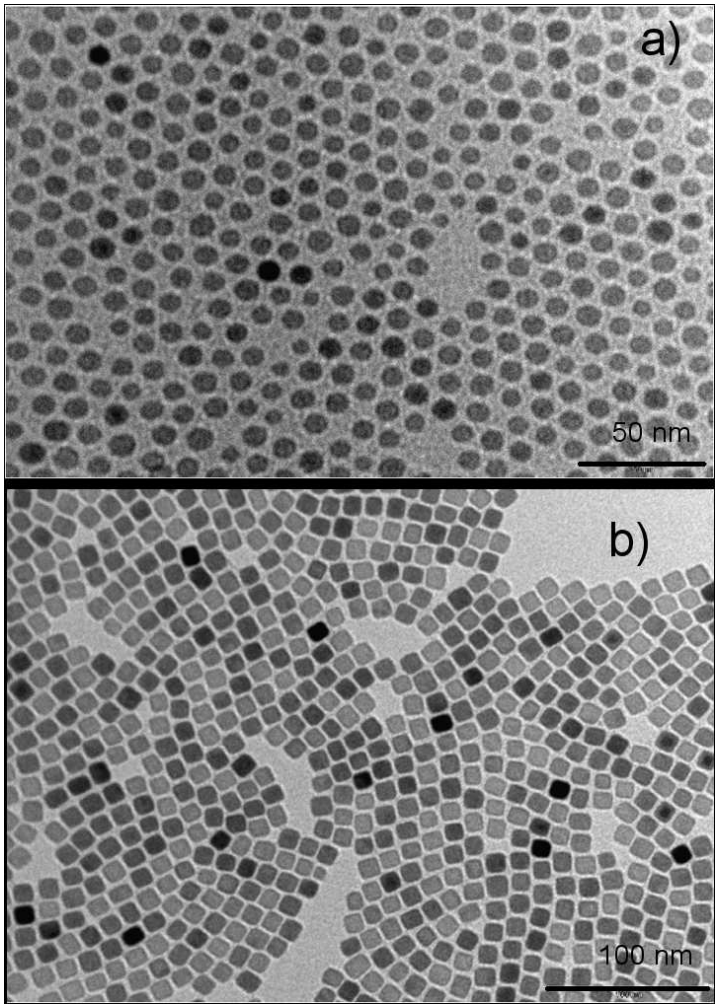

Figure 4.39: TEM image of MNPs a) G117 spherical nanoparticles, b) G119 cubic nanoparticles

discussed in the chapter 1, if we field cooled an antiferro-ferro composite material, through the Néel temperature we can observe a shift in the hysteresis loop (exchange bias field). All the measurements have been done on both colloidal suspension of nanoparticles and on dry samples, in order to avoid the effect of the solvent. Figure 4.40 shows ZFC -FC measurements of spherical nanoparticles under an applied field of 50 Oe. With sol we indicate colloidal dispersions of nanoparticles in chloroform. The sample G122 has been dried before measurements since we expected a blocking temperature higher than the boiling point of chloroform. The nanoparticles of dimension lower than 12 nm show a typical ZFC-FC behavior typical of superparamagnetic MNPs. The results are shown in table 4.5 where T_B is the average blocking temperature that corresponds to the maximum of ZFC measurement; T_{irr} is the temperature of irreversibility that corresponds to the first temperature at which ZFC and FC measurements

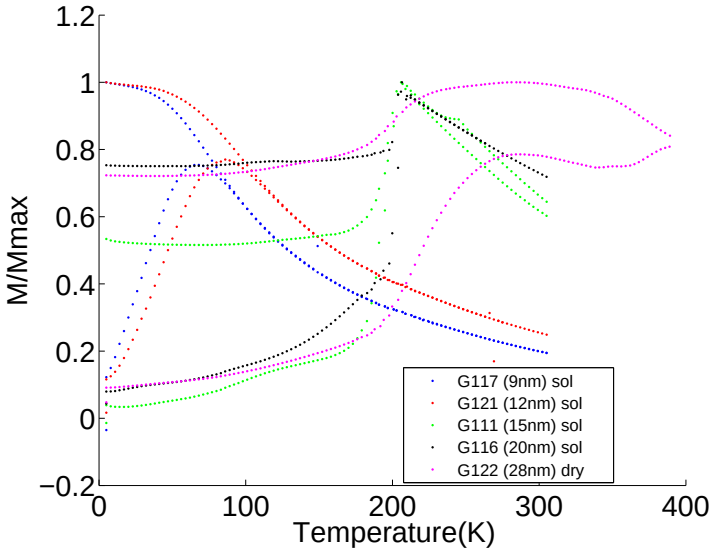

Figure 4.40: ZFC-FC measurements on spherical nanoparticles with an external field $H = 50\,Oe$

	$T_B(K)$	$T_{irr}(K)$	$T_{Sat}(K)$
$G_{117}\ 9nm$	65	85	44
$G_{121}\ 12nm$	86	107	65

Table 4.5: Blocking temperatures of spherical nanoparticles

coincide and is the highest blocking temperature of MNPs assembly; T_{sat} is the temperature under which the FC measurement becomes constant, this is the lowest blocking temperature. The ZFC-FC curves of other samples show a jump at the Néel temperature of wustite (200 K), that is a fingerprint of wustite presence. No blocking temperature is shown in the analyzed range. So we can deduce that in smaller spherical nanoparticles only magnetite/maghemite is present because the wustite core is completely oxidized to $Fe_3O_4/\gamma Fe_2O_3$ for small MNPs size. The same results are shown for cubic nanoparticles (figure 4.41). Also the cubic samples were analyzed in chloroform dispersion except for sample G124 where the particles have been dried before measurements since we expected a blocking temperature higher than the boiling point of chloroform. In this case we have measured up to 400 K. All the three cubic samples have a jump in magnetization at the Néel temperature of wustite. Only the smallest G119 (11 nm) sample shows a ZFC-FC superparamagnetic behavior below 200 K (see table 4.6).

	$T_B(K)$	$T_{irr}(K)$	$T_{Sat}(K)$
$G_{119}\ 11nm$	143	161	122

Table 4.6: Blocking temperatures of cubic nanoparticles

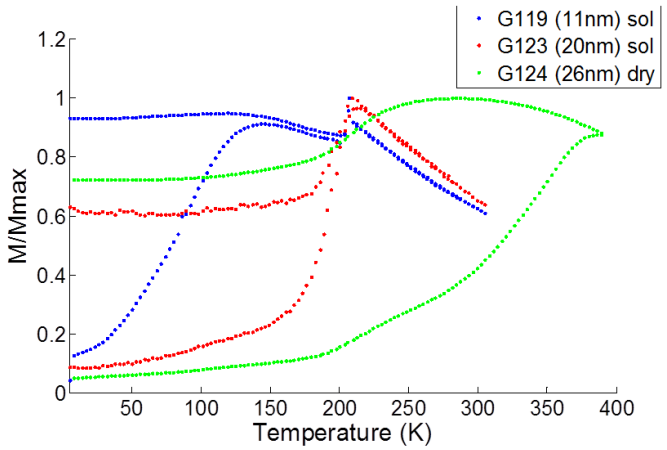

Figure 4.41: ZFC-FC measurements of cubic nanoparticles with an external applied field of H=50 Oe.

Chloroform has the melting temperature near 200 K and in order to exclude that the jump is only due to a mechanical rotation of nanoparticles in a liquid environment under an applied field, we have measured some samples also in dry state obtaining identical results. In order to investigate the presence of exchange bias behavior due to the exchange coupling between nanoparticles core and shell phases, we cooled the sample in the presence of a 5T field and then measured the hysteresis loop at 5K. We compared the results with the loop obtained after zero field cooling (figure 4.42). We can see a shift of FC respect to ZFC loop along the field axis

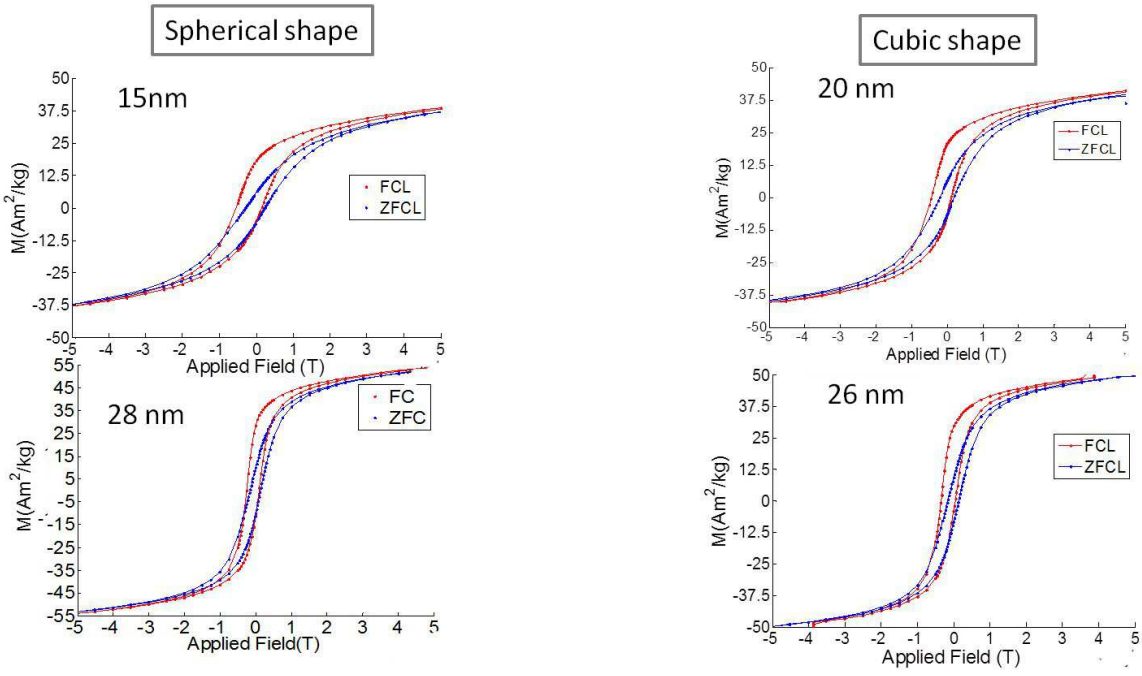

Figure 4.42: Magnetic ZFC-FC loop at 5K for spherical and cubic nanoparticles

that can be attributed to the exchange coupling between the antiferromagnetic phase (wustite) and the ferromagnetic phase (magnetite-maghemite). It can be noted that the exchange field values depend on nanoparticles size (see table 4.7) because there is a difference in exchange bias effect related to the wustite volume respect to magnetite/maghemite volume. In the 4.7 the exchange field values are reported together with coercivity and saturation magnetization.

	$M_S(Am^2/kg)$	$H_C(Oe)$ ZFC	$H_C(Oe)$ FC	$H_E(Oe)$ FC
Spherical G_{111} $15nm$	38	2400	3270	1759
Spherical G_{116} $20nm$	48.5	330	330	0
Spherical G_{122} $28nm$	53	1510	1760	750
Cubic G_{119} $11nm$	64	400	400	0
Cubic G_{123} $20nm$	41	2030	2772	1663
Cubic G_{124} $26nm$	50.5	1391	2014	1507

Table 4.7: Magnetization saturations, exchange bias fields and coercive fields at 5 K

The saturation magnetization values are lower than the magnetite and maghemite bulk one, this could be due to the presence of wustite and to high surface to volume ratio, while the coercivity values are higher because of the induced anisotropy at the interface between the two phases. As we can observe in the table 4.7 only two of the spherical samples show an exchange bias behaviour: G111 (spherical 15nm), G122 (spherical 28nm). In sample G122 (spherical shape with diameter 28 nm) the exchange field is lower and coherently the coercivity is lower the saturation is higher respect to G111. These results reflect the lower wustite content respect to magnetite in sample G122, already shown in ZFC-FC measurement (figure 4.40). These conclusions have been confirmed by XRD characterization, not shown here. If we consider sample G116, which shows a small peak at 200 K (figure 4.40), we can see that no shift and consequently no exchange bias have been measured, this could be related to a very low ratio between wustite and maghemite/magnetite content. In agreement with the ZFC-FC temperature measurements (figure 4.6), we can observe an exchange bias between an antiferromagnetic and a ferromagnetic phase in samples G123 (cubic with size 20 nm) and G124 (cubic with size 26 nm) . Moreover, the saturation magnetization is lower than bulk value of magnetite, this can be due to the small size and to the presence of wustite.

4.7 Conclusions

We have analyzed magnetite-maghemite MNPs of different sizes (8 and 4 nm) and obtained through two different chemical syntheses. A complete characterization of magnetic, structural

and morphological characteristics has been performed for all the nanoparticles. The MNPs have high crystallinity, narrow size distribution and superparamagnetic behavior at room temperature. We have focused our attention on the role of interactions between them and the role of surface functionalization.

Two different applications have been studied: magnetic separation and hyperthermia.

In the first case we have found the optimal characteristics for a good solid phase separator in clusters of nanoparticles. The method of extraction for polycyclic aromatic hydrocarbons in urine samples was studied and optimized. Compared with commercial devices, the synthesized magnetic beads allowed to achieve superior extraction performances obtaining lower limits of quantification values in ng/l range using a rapid and low-cost procedure.

In the case of magnetic hyperthermia we have shown that the specific absorption rate increases by increasing nanoparticles interactions, showing higher values (up to 50 W/g) than reported in the literature due to the collective behavior.

Then we have studied some composite MNPs with a core of wustite and a shell of magnetite/maghemite. These systems are very interesting and we have observed the evolution of exchange bias by reducing the size and changing the shape of MNPs (i.e. spherical and cubic). We have noted that in low dimension the coexistence of the two phases is not allowed. It was found for spherical particles of diameter higher than 15 nm and, for cubic particles of edge higher than 11 nm, giving rise to exchange bias behavior. These samples show a shift (up to 1760 Oe), in hysteresis loop at 5 K after a field cooling in H=5T, and an high coercivity values.

Chapter 5

Composite and multifunctional nanostructured materials

New nanocomposite materials have been studied, able to combine the complementary characteristics of two different materials or complex multicomponent inorganic/organic nanostructures, for example semiconductor and magnetic nanoparticles [153, 154, 155, 156]. These material can be able to satisfy and give an answer to different problems, they can be used as actuators or elements for biomedicine even through remote control.
Here I present the results on three nanostructures: $ZnO-Fe_3O_4$ nanocomposites, $SiC-Fe_3O_4$ nanocomposites and Ni-Mn-Ga intrinsically multifunctional material.

5.1 $ZnO - Fe_3O_4$ nanocomposites

The aim of this work is to realize a material with the complementary characteristics of a semiconductor and a magnetic material in order to exploit the different functional properties of the two materials. Zinc oxide is chosen for its physical characteristics, it is a II-VI compound semiconductor and it has a wide bandgap (3.4 eV), it has a wurtzite structure with lattice spacing a = 0.325 nm and c = 0.521 nm. For the above characteristics its main application fields are transparent electronics, ultraviolet (UV) light emitters, piezoelectric devices, chemical sensors and spin electronics. In particular, its larger exciton binding energy (60 meV) makes it a very promising UV emitter [157]. When employed as sensors , ZnO bulk crystals and films, have demonstrated high sensitivity to toxic gases [158, 159, 160]. Another possibility is to drug ZnO with ferromagnetic ions as Manganese [161] and Vanadium [162] in order to have a magnetically doped semiconductor to be used for spintronics applications. In the last decades many efforts have been devoted to the synthesis, characterization and device applications of ZnO

nanomaterials; in particular different kinds of nanostructures, such as nanowires, nanotubes, nanorings, and nano-tetrapods, have been grown via a variety of methods: chemical vapor deposition, thermal evaporation, and electrodeposition [163, 164, 165, 166, 167, 168, 169]. In biomedical applications ZnO nanostructures have been studied for their possibility to produce singlet oxygen under UV and X-Ray irradiation [170, 171, 172]. We have analysed the magnetic characteristics of a nano-composite material formed by ZnO tetrapods and magnetite nanoparticles in order to obtain multifunctional nanostructures

5.1.1 Nanocomposite material preparation

In collaboration with the group of Dr. Zappettini (IMEM-CNR Parma), ZnO and nanoparticles have been obtained by two different syntheses and then the materials are bring together. ZnO tetrapods (shown in figure 5.1) have been obtained from vapor phase with very high crystalline and optical quality [173].

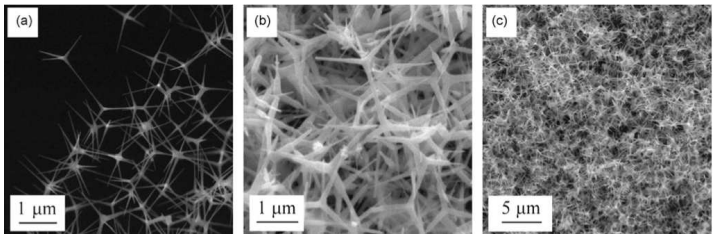

Figure 5.1: SEM images of ZnO tetrapods with different concentrations

Fe_3O_4 MNPs have been synthesized by thermal decomposition, using $Fe(acac)_3$ as the metallorganic precursor and oleylamine as the surfactant. Specific amounts of magnetite nanoparticles and ZnO tetrapods have been mixed in hexane and then quickly heated under nitrogen atmosphere at $400°C$. The weight ratio between Fe_3O_4 and ZnO was varied in the range 1/75 - 1/135 (values obtained by SEM microanalysis), in order to optimize the nanocomposites characteristics.

5.1.2 Morphological and structural characterization

The morphological and structural characterizations have been done by TEM and XRD. As prepared nanoparticles have hexagonal shape, as shown in figure 5.2, and a structure Fd3m, a good size homogeneity with the nanoparticle size peaked at 9 nm. We can see the nanocomposite material in figure 5.3: Fe_3O_4 MNPs are linked to tetrapods surface. The nanoparticles on tetrapods are randomly destributed (figure 5.3), they form aggregates of different sizes, but

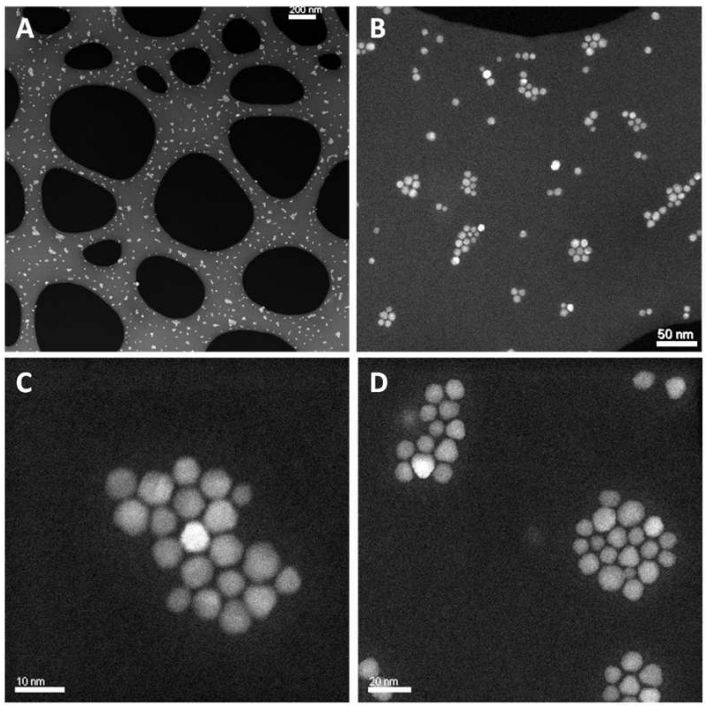

Figure 5.2: TEM images of the as-prepared magnetite MNPs

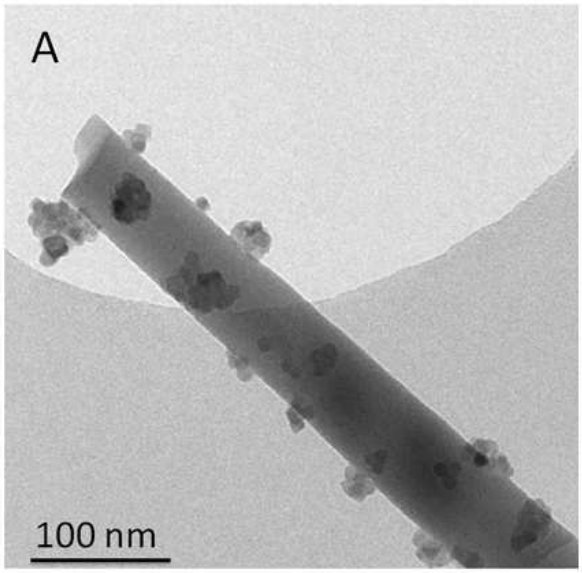

Figure 5.3: STEM of ZnO tetrapods and nanoparticles

the size of singular nanoparticle is not change, so the difference it is only due to the different interactions between nanoparticles in colloidal dispersion and nanoparticles on tetrapods. In the first case their interaction is dipolar, while, when they are attached to tetrapods the absence of shell, that probably has been damaged during heat treatment, gives origin also to

exchange interaction in a sort of superferromagnetic behavior.

The nanoparticles are very well bounded to tetrapods surface: as the two materials are oxides their surfaces have very similar chemical groups, an affinity which favours a ligands formation. Moreover at Fe_3O_4/ZnO interface the HRTEM has evidenced a meniscus, due to MNPs deformation in order to adapt to tetrapod surface.

5.1.3 Magnetic and photoluminescence measurements

The main characteristics that we wanted to control in the composite nanostructure are photoluminescence and magnetic behavior. The doping effect with magnetic ions does not give the same possibility because the magnetic effect is usually very low if the amount is low and if the magnetic ions are added in a too high amount big differences in the photoluminescence behavior is done.

The first observation is the conservation of the photoluminescence properties in nanocomposites after the functionalization with Fe_3O_4 nanoparticles. In particular the photoluminescence measurement done at room temperature is shown in figure 5.4 and it reveals a near band edge emission, for the coupled compound $Fe_3O_4 - ZnO$ (red line), similarly to what is observed for the bare ZnO tetrapods (blue line). It has to be underlined that magnetite shows no emission in the measured range, and the only difference is the shift in the peak at 500 nm, that is usually ascribed to the ZnO surface defects emission and which origin is still under debate. The shift is very low and it is due to the effect of the functionalization of surface.

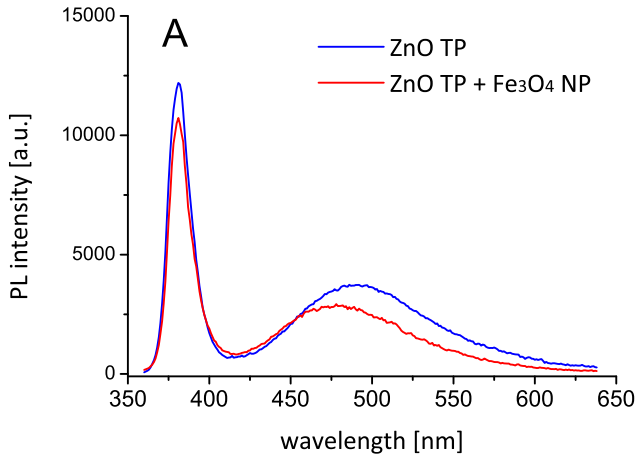

Figure 5.4: PL spectra at RT of bare ZnO tetrapods (blue line) and functionalized ZnO tetrapods (red line)

Similarly to the approach chosen for ZnO tetrapods, the magnetic characteristics of nanoparticles are measured before and after their attachment to the tetrapods surface. Before the MNPs attachment, in agreement with the size distribution evidenced by TEM, the MNPs behavior is superparamagnetic at room temperature (figure 5.5), with a saturation magnetization of $(53 \pm 2)\, Am^2/kg$. The shell weight was not taken into account and the magnetization value can be underestimated. In order to estimate the blocking temperature and the behavior

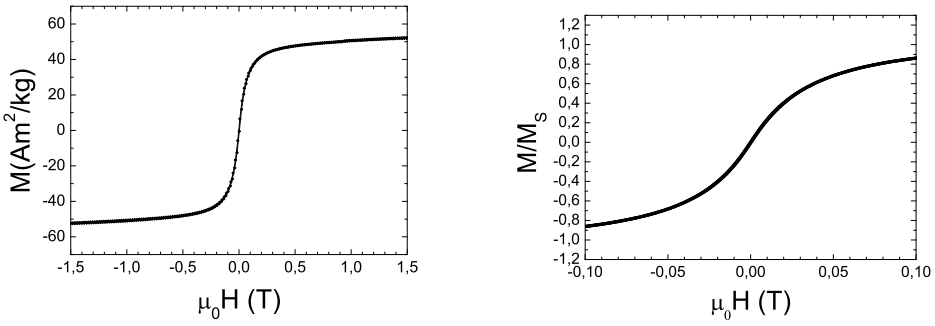

Figure 5.5: Hysteresis loop at RT of the as prepared MNPs. Left: maximum filed of 1.5T. Right: maximum field of 0.1 T

as a function of temperature, ZFC-FC measurements have been performed. As shown in figure 5.6, the blocking temperature is $(88 \pm 10)\, K$ and the irreversibility temperature is $(143 \pm 10)\, K$. Furthermore the FC curve highlights the presence of nanoparticles not very interacting in fact it has a saturation temperature at 30-40 K. Tetrapods-nanoparticles have been magnetically characterized and a first difference has been observed in the presence of hysteresis at room temperature, as shown in figure 5.7. The coercive field is $(20 \pm 2)\, Oe$ and the remanence is 2% of saturation. In order to better understand nanoparticles behavior, a ZFC-FC measurement has been performed. The result is shown in figure 5.8. Most of the MNPs are in the superparamagnetic regime at room temperature and the average blocking temperature is $(46 \pm 5)\, K$. However a small fraction of MNPs are blocked at room temperature due aggregation and inter-particles interaction. A saturation temperature can be identified in the FC curve at $(42 \pm 4)\, K$ and can be related to a superspin glass behavior, due to inter-particle interactions. The absence of irreversibility temperature causes the hysteresis at room temperature, because some nanoparticles are still blocked. This blocked state could be due to MNPs interactions, but we can not exclude an increment of MNPs size during nanocomposite material preparation, considering that TEM analysis of $ZnO + Fe_3O_4$ samples has not meaningful statistics

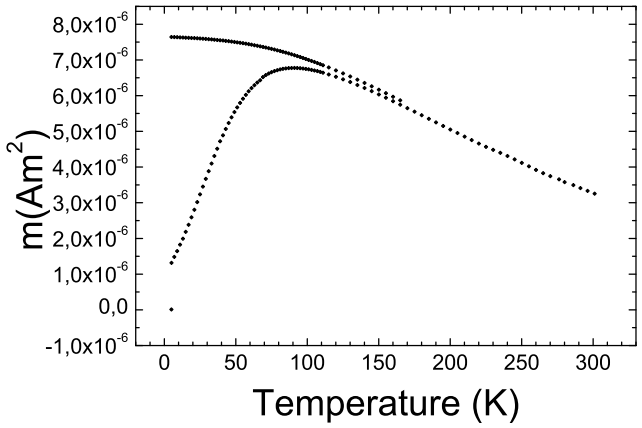

Figure 5.6: ZFC-FC curves measured on as-prepared Fe_3O_4 . The magnetic applied field is 100 Oe

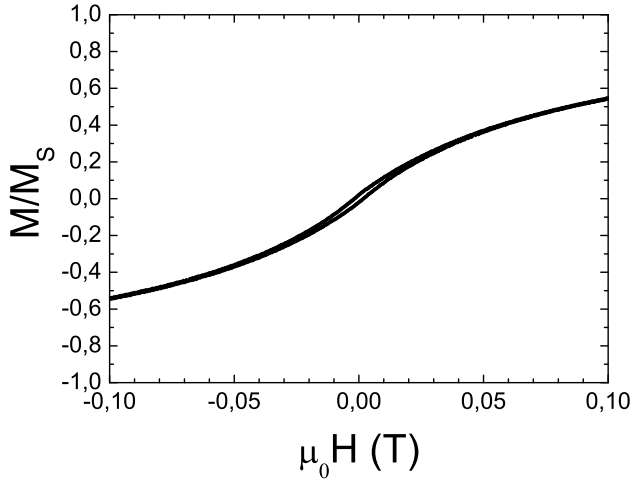

Figure 5.7: Hysteresis loop at RT of magnetic nanocomposite material $ZnO - Fe_3O_4$

concerning the Fe_3O_4 size. In order to have information about the nanoparticles size we have used a model [174] for fitting the derivative of ZFC curve following the equation:

$$m_{ZFC}(T) = \frac{H m_S^2(T)}{3k_B T} \int_0^T f(T_B) dT_B \tag{5.1}$$

where m_{ZFC} is the ZFC moment, m_S is the saturation moment of singular nanoparticle, T_B is the blocking temperature of singular particle, $f(T_B)$ is the distribution function of blocking temperatures of the nanoparticles considered as a lognormal (see equation 4.16). The result

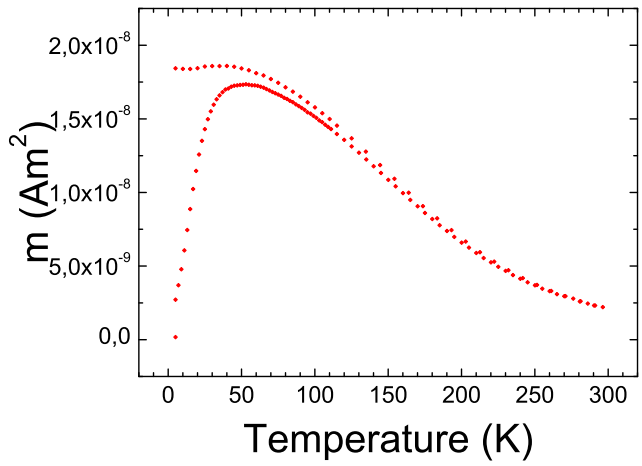

Figure 5.8: ZFC-FC measurement of $ZnO - Fe_3O_4$ nanocomposite with an applied field of 100 Oe.

is shown in figure 5.9

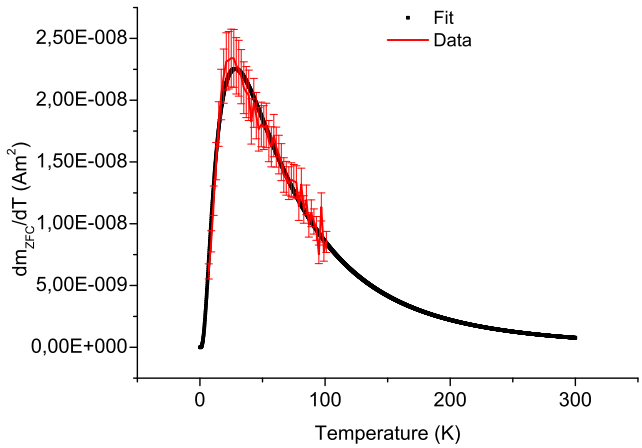

Figure 5.9: Derivative of the experimental ZFC curve (red) and result of the fitting (black) for the Fe_3O_4 MNPs on tetrapods.

Taking into account the relation between the size and the blocking temperature (equation 1.50), we have obtained the size distribution of nanoparticles in superparamagnetic state, using as anisotropy constant the value $K_{eff} = (4.4 \cdot 10^4)\ J/m^3$ that takes into account the effect of surface [175]. The size distribution (figure 5.10), shows an average size 10 nm, close to the TEM average size on as prepared nanoparticles (9 nm). So we can conclude that most

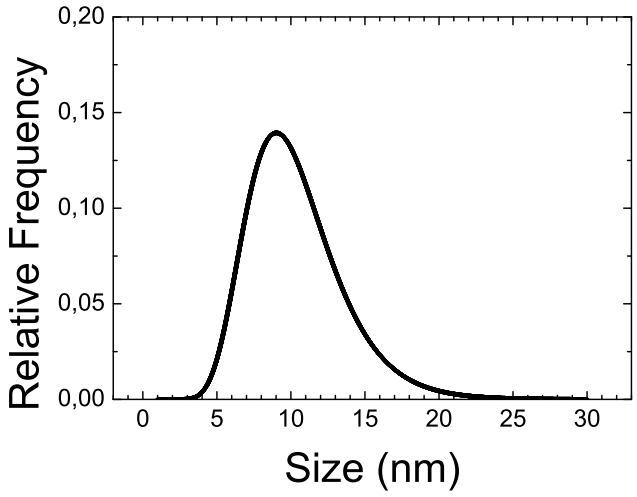

Figure 5.10: Size distribution of nanoparticles on tetrapods

of the nanoparticles on tetrapods are in the superparamagnetic state with a size distribution similar to the starting distribution, but a small fraction of nanoparticles are in a blocked state at room temperature. Furthermore the nanoparticles are interacting in fact there are few aggregates on tetrapods of different sizes.

5.1.4 Conclusions

In conclusion, we have obtained a new nanocomposite material, in which superparamagnetic Fe_3O_4 nanoparticles are coupled to vaporphase grown ZnO tetrapods. The sintering process does not affect the crystalline phase of each material and has small effects on ZnO photoemission spectra and Fe_3O_4 superparamagnetic properties. For these reasons, such functionalized nanostructures can be readily used in photocatalytic systems or gas sensing devices. Considering superparamagnetism as a further degree of freedom respect to ZnO functionalities, it would be very interesting to study the Fe_3O_4ZnO coupled compound in water splitting, biomedical applications and new-concept piezo-magnetic actuators.

5.2 $SiC - Fe_3O_4$ nanocomposites

In the frame of a collaboration with group of Dr. Salviati (IMEM-CNR Parma) and group of Prof. Bigi (Chemistry Department of Parma University) we have studied a nanocomposite material: magnetite MNPs linked to the surface of Silicon carbide. SiC is a semiconductor

chosen for its properties, in particular its light emission efficiency. Significant improvements of its light emission have been made by using porous or nanosized cubic (3C) structures [176, 177, 178, 179], in which the increase is due to surface states or quantum confinement effects. Furthermore this material has a very high biocompatibility [180, 181], so 3C-SiC is a promising material for biomedical applications. SiC nanostructures functionalized with specific organic molecules could be used as nanoprobes for new classes of highsensitivity biosensors. A very interesting molecules choice can be porphyrins, because of the good match between the 3C-SiC near-band-edge optical emission and the porphyrin absorption Q band, and this organic/inorganic material can be used to realize electro-optical sensing devices [182] or for cancer cure. The 3C-SiC green emission can be used to create the singlet oxygen production by porphyrins, that is the dominant cytotoxic agent during photodynamic therapy [183, 184]. Another important improvement could be related to the presence of silica shell around the SiC nanostructure, as recently proved on SiC nanowires [185].
In this work we propose a new multifunctional innovative nanocomposite system made up of $3C - SiC/SiO_2$ nanowires and superparamagnetic Fe_3O_4 nanoparticles. The system is proposed for concurrent photodynamic and hyperthermia therapies as well as for magnetic resonance imaging. The biocompatibility of nanowires and magnetic nanoparticles has been separately tested by in-vitro tests. A complete magnetic, morphological and compositional characterization has been obtained on both nanoparticles and nanocomposite systems.

5.2.1 Nanocomposite material preparation

3C-SiC nanowires with a silica shell was obtained by means of carbothermal method, based on the reaction between carbon monoxide and the native oxide on (001) Si substrates, using different chatalists [185]. The process was done in an open tube under a flow of CO and with N_2 or Ar as carrier gases, at high temperature (1050°C and 1100°C). The nanowires are very well organized on the silicon surface, and their size and lenght change by changing temperature, the flux and type of gas; thanks to this growth technique very high deposition rates can be obtained. Nanoparticles have been obtained through thermal decomposition with the same procedure described in section 4.5, and then linked to nanowires by means of click-chemistry (process shown in figure 5.11). The free hydroxy groups present in the nanowires silica shell were properly functionalized and then the superparamagnetic iron oxide MNPs, after further stabilization (10-undecynoic acid), were grafted onto the NWs by exploiting an

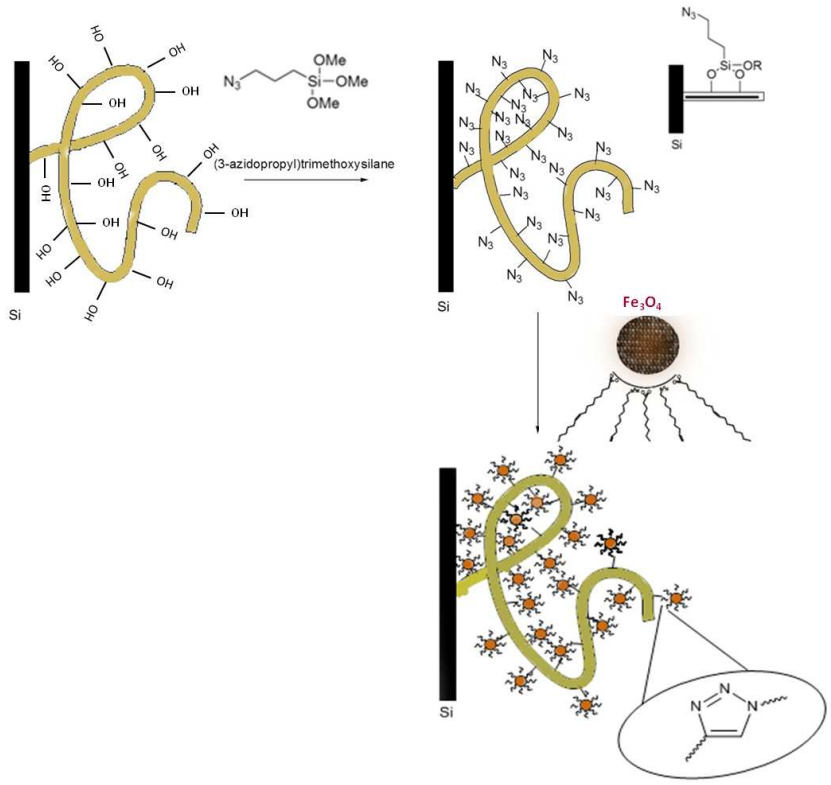

Figure 5.11: Click chemistry scheme

azide-alkyne Huisgen cycloaddition reaction [186].

5.2.2 Morphological and structural characterization

The obtained nanowires were observed by TEM and SEM. We can observe a high density of well oriented wires (see figure 5.12). The size of nanowires changes from 500 nm to few micron in length and 20-50 nm in diameter.

After having removed the wires from the substrate, and functionalized them with nanoparticles of 8 nm, we have observed a composited material in which nanoparticles are well distributed along the nanowire with an almost uniform distribution (figure 5.13). The MNPs surface functionalization allows the chemical bonding to the nanowire maintaining the original shape and size. Differently to what observed on $ZnO + Fe_3O_4$ samples, the magnetic nanoparticles do not form aggregates on the nanowire and the MNPs distribution is homogeneous.

The content of Fe respect to Si has been evaluated by an EDS analysis: considering a perfect magnetite composition we can estimated a 1.48 weight % of magnetite respect to $3C - SiC - SiO_2$.

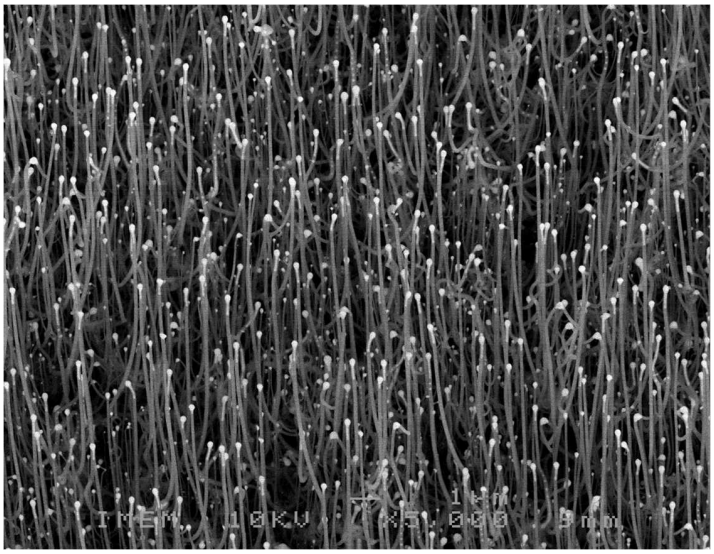

Figure 5.12: SEM image of nanowires of $3C - SiC - SiO_2$ with the chatalist head

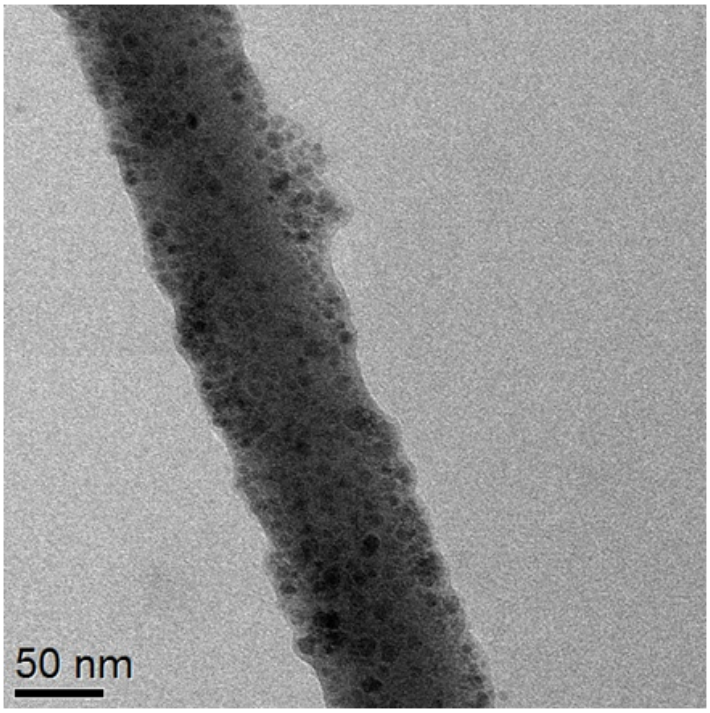

Figure 5.13: STEM image of a SiC nanowire with magnetite nanoparticles on its surface

5.2.3 Magnetic characteristics of the nanocomposite material

The magnetic characteristics of the as-prepared nanoparticles have been already shown in the section 4.5: they are superparamagnetic at room temperature (see figure 4.35), they are weakly magnetically interacting and well dispersible in polar solvent thanks to their surface function-

alization. The magnetic characteristics of the nanocomposite material have been analyzed by the same techniques used for the previous samples. As shown in figure 5.14, we can observe that at room temperature a small coercive field of $(18 \pm 3)\, Oe$ and a ratio of 2.2% between remanence and saturation are evident. In order to understand the origin of this hysteresis not

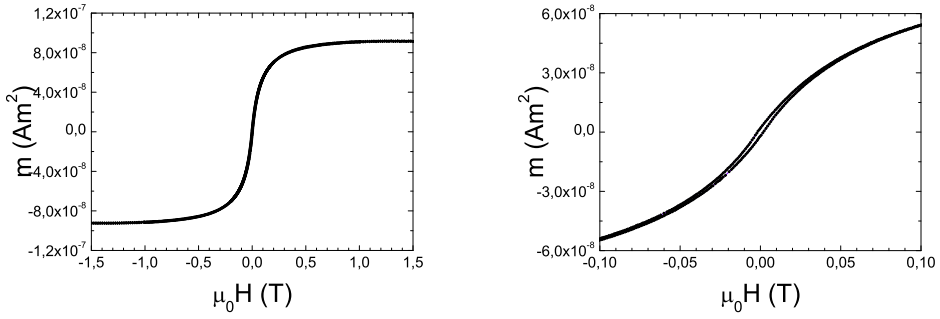

Figure 5.14: Hysteresis loop at room temperature of nanocomposite $SiC - Fe_3O_4$ wires. Left: maximum field 1.5 T, right: maximum field 0.1 T

present in the as-prepared MNPs we have done an analysis as a function of temperature (figure 5.15): the ZFC-FC curves are typical of a sample showing superparamagnetic regime at room temperature, a $T_B = (36 \pm 5)\, K$ and an an irreversibility temperature of $T_{irr} = (55 \pm 5) K$. The small difference between these values reflects the homogeneous distribution of the MNPs and the absence of aggregates. So the ZFC-FC measurement does not justify the presence of this

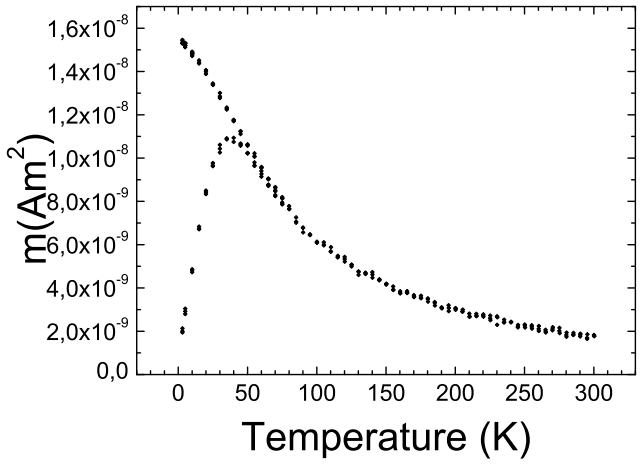

Figure 5.15: ZFC-FC measurements of $SiC - Fe_3O_4$ nanocomposite with an applied field of 20 Oe

small coercivity observed at room temperature. A deeper analysis of magnetic characteristics at low temperature (5K) highlights a very small coercivity lower than 130 Oe, which induced us to consider the possible presence of soft magnetic impurities due to the precursor used for SiC growth. We are going to improve the wires growth and functionalization technique in order to have pure samples without catalyst impurities.

5.2.4 Conclusions

In conclusion, we have obtained a new nanocomposite material with Fe_3O_4 nanoparticles on the surface of $3C - SiC/SiO_2$ nanowires, showing MNPs with optimized size homogeneity (8 nm), distribution on nanowires' surface, and superparamagnetic behavior. Fe_3O_4 properties, coupled to SiC/SiO_2 photoemission, make the composite nanowires very promising agents for a cancer therapy combining magnetic hypertermia with photodynamic therapy.

5.3 An intrinsically multifunctional material

The last part of this study on magnetic materials to be used in sensors and biomedicine, is on a new intrinsically multifunctional material: Ni-Mn-Ga alloy, in particular we decide to obtain nanodisks by means of a lithographic technique applied to thin films grown by rf. sputtering. This technique consists in two steps: a monolayer of nanoparticles are deposited on film surface and in the second step they act as mask during sputter etching. The activity was performed with the group of Dr. Tiberto (INRIM Torino).

5.3.1 Ni-Mn-Ga properties

The Ni-Mn-Ga alloy is a very interesting and studied magnetic shape memory alloy. It has been studied in the last decades thanks to the very high macroscopic strain (up to 10 % in high quality single crystal) which exceeds by one order of magnitude the strain of piezoelectrics. The interplay between structure and magnetism is at the origin of their extraordinary phenomenology: a martensitic transformation between two phases, a low symmetry martensite and a cubic austenite occurs, also involving a change in the magnetic properties. The shape memory effect was discovered in 1996 [187] and it is related to the magnetic field induced reorientation of twin boundaries in the martensitic phase.
Remarkable high magnetic field induced strains were also obtained in policrystalline materials by inducing the martensitic transformation in magnetic field (magnetic super-elasticity) [187,

188, 189]. In the first case, the magnetic key property is the magnetocrystalline anisotropy of martensite that makes the twin boundary displacement more favorable than the magnetization rotation. In the second case it is the magnetization variation ΔM at the transformation, and the magnetic field dependence of the martensitic transformation temperature.
The Curie temperatures of the two crystalline phases and the transition temperature can be widely tuned by suitable changing of compositions.
This emerging class of materials has been intensely studied in the last years for the possibility of combining the advantages of high strain and high cycling ability that paves the way to new applications as actuators or sensors. They have mainly been studied as bulk crystal, recently many efforts have been also devoted to their realization in thin film form by different deposition techniques. The characteristics of the film change in dependence on the sputtering deposition parameters and substrate choice. It has been grown in many different substrates as MgO, Si, Al_2O_3, $NaCl$ [190, 191, 192, 193, 194, 195]. The aim of the works on thin films is to create at room temperature a martensitic material in order to reorient the twin boundary by means of magnetic field. On the other hand the possibility to induce the martensitic transformation close to room temperature and exploit the properties variation, e.g. shape, magnetic and electronic characteristics, are an important goal also in thin films. The fingerprint of martensite is the presence of twinning. Their period Λ depends on the elastic volume energy and on surface energy. In particular if we consider the linear elastic theory, the elastic energy depends on the E-modulus (E) and increases with the volume of martensitic variants. so if the volume of a martensitic variant is reduced there is an increase of the number of twin boundaries, and the twin boundary energy increases. So the martensitic microstructires is due to the minimization of the sum of both competing energies and the resulting twinning period of the microstructure depends on the thickness of the martensitic variant d, the twin boundary energy γ_I and the crystal-lattice strain ϵ_I following a law [196] equal to Kittel one originally developed for magnetic stripe domains [197]:

$$\Lambda = \left(\frac{\gamma}{E\epsilon_I^2} d \right)^{\frac{1}{2}} \tag{5.2}$$

The present work is mainly addressed to the realization of epitaxial freestanding nanodisks showing conventional and magnetic shape memory at temperatures slightly above room temperature, to be exploited in biomedical applications.

5.3.2 Ni-Mn-Ga grown on Si with resist underlayer

Driven by the idea of obtaining free standing disks at the beginning we decided to grow thin films by sputtering with thickness ranging from 60 to 100 nm on Silicon substrate covered by a common phoresist layer. The sputtering parameters (pressure and voltage) have been chosen in order to minimize the increment of substrate during growth. The grown samples are reported in table 5.2. All the films show low crystallinity as highlighted by XRD analysis

Sample	Voltage (V)	Pressure (mbar)	Thickness (nm)
1461	700	$1.4 \cdot 10^{-2}$	100
1462	700	$1.4 \cdot 10^{-2}$	60
1463	900	$1.4 \cdot 10^{-2}$	100
1464	900	$1.4 \cdot 10^{-2}$	60

Table 5.1: Ni-Mn-Ga films grown on resist

shown in figure 5.16. Only one peak is present, suggesting an oriented growth along one of the face diagonals (110-type) of the cubic structure From the peak we can esteem the average size of nanocrystals: 4-5 nm. The SEM shows a very flat surface (figure 5.17) that could be

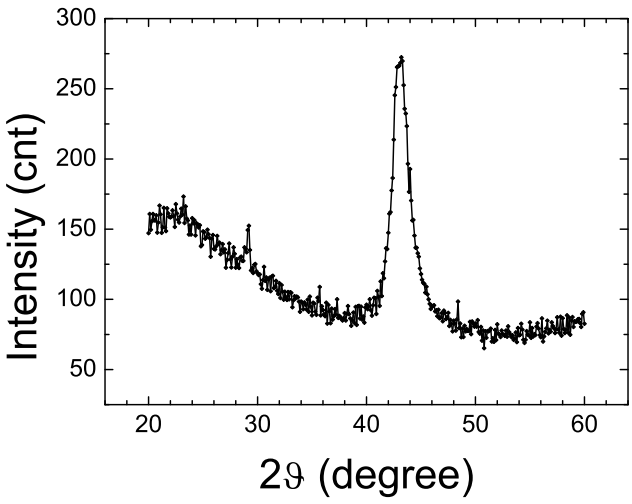

Figure 5.16: XRD scans measured in Bragg-Brentano geometry of 100 nm film grown on silicon at room temperature (sample 1461)

associated with a nanocrystalline structure. The obtained films have been fully characterized in order to assess their suitability for the lithographic process. The magnetic signal at room temperature is very low and not significant and has induced us to change substrate and growth

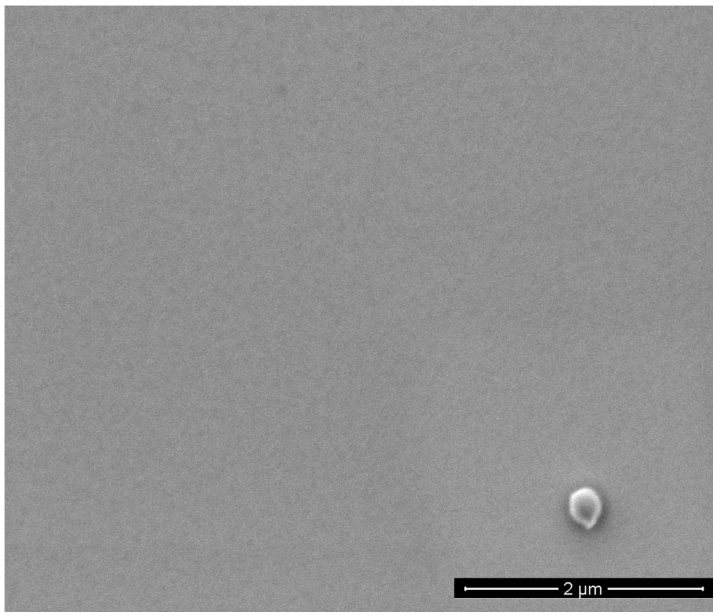

Figure 5.17: SEM image of a sample of 100 nm grown on silicon with resist underlayer. We can not observe the presence of any kind of crystalline structure, and this agree with the XRD analysis.

temperature. For the above reasons we have decided to grow the material on MgO with an underlayer of Cr, which can be selectively removed with a specific etchant. This technique has been already reported in literature in order to obtain free standing films of Ni-Mn-Ga [198, 199].

5.3.3 Ni-Mn-Ga grown on MgO with Cr underlayer

Cr is a suitable candidate for sacrificial layer because it grows epitaxially on single crystalline MgO substrates [199]. Furthermore the lattice spacings of Cr (a_{Cr} = 2.8839 nm [199]) has a very low misfit with respect to Ni-Mn-Ga (0.9 %) that grows epitaxial on it. From the comparison between the lattice parameters of these materials, it is expected that the Cr unit cell grows face-on-face rotated by 45° respect to the MgO. On the other hand, no rotation of the face-on-face growth is expected between Cr and Ni-Mn-Ga. In order to avoid interdiffusion of Cr in MgO and in NiMnGa, we control the growth of Cr alone on MgO by changing the temperature. We chose two temperatures namely 400℃and 350℃. The voltage between target and substrate was fixed at 700 V and we chose two thicknesses 100 nm and 50 nm for each temperature. At both temperatures the growth is epitaxial in fact in the XRD patterns we can see a peak corresponding to (200) Cr as reported in literature. At 400°C an interdiffusion

of Cr in MgO substrate was observed by XRD, as shown in figure 5.18.

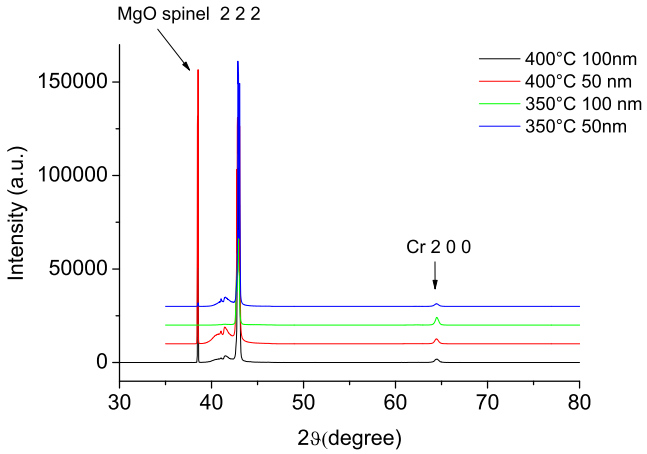

Figure 5.18: XRD pattern diffraction in Bragg-Brentano geometry obtained at room temperature on Cr films grown on MgO substrate at 400°C and 350°C

In samples grown at 400°C in addition to the peak of the Cr (200) and to MgO (200) a peak at 38.5 degree is present that could correspond to a crystal spinel structure of MgO probably due to a change in crystal structure due to the interdiffusion of Cr in the substrate. In order to avoid this effect we have decided to grow the material at 350°C We have decided to grow the thinnest Cr layer in order to decrease the etching time. From the above observation Ni-Mn-Ga has been grown in thin film form on 50 nm thick Cr at 350°C(see table)

Sample	Voltage (V)	Pressure (mbar)	Thickness (nm)
1481	900	$1.4 \cdot 10^{-2}$	100
1485	900	$1.4 \cdot 10^{-2}$	75
1486	1200	$1.4 \cdot 10^{-2}$	100
1536	1200	$1.4 \cdot 10^{-2}$	75

Table 5.2: Ni-Mn-Ga films grown on Cr(50 nm)/MgO at 350°C.

In this case we have chosen two voltages 900 V and 1200 V, and we grew two thicknesses for each power: 75 and 100nm (table 5.2). At high temperature the NiMnGa grows in austenite phase; the occurrence of the martensitic transformation on cooling beyond a critical temperature (the martensitic transformation temperature) is related to both intrinsic and extrinsic characteristics: in particular, while composition is the main intrinsic property affecting the transformation temperature in bulk materials, in thin films the interaction with the substrate plays a pivotal role. The martensitic transformation involves a noticeable change in the lat-

tice parameters of the material, thus the lattice mismatch and the elastic constrains set by the presence of a rigid substrate may dramatically affect the transformation. As observed on Ni-Mn-Ga thin films on Mgo substrates elsewhere, [200] the occurrence of the martensitic transformation induces morphological changes to the surface of Ni-Mn-Ga: the self accommodated twin variants of the martensitic phase can generate a superficial pattern, hereby defined as "roofs", easily observable by AFM measurements.

In the case of 100 nm sample grown at 900 V only a few roofs can be observed (see figure 5.19 a), while in the sample grown at 1200 V the roof-like modulation can be observed throughout all the surface area measured (see figure 5.19 b), the same behavior is shown for 75 nm samples, i.e. the film grown at 1200 V shows a considerably larger area covered by roof-like surface modulation.

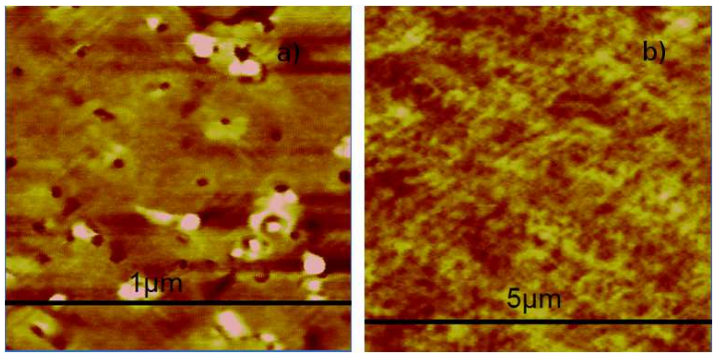

Figure 5.19: AFM images of 100 nm thick NiMnGa grown on Cr/MgO: a) voltage growth 900 V, b) voltage growth 1200 V

However, there is also an important dependence on thickness of the structural stability of the two phases. Figure 5.20, for instance, shows the AFM signal of the 75 nm sample grown at 900 V: we can see a very different morphology, where no roofs are present, but a very net grainy morphology suggesting that the film is still in the austenitic phase. If we limit our analysis to AFM evidence, it appears that by increasing both the thickness and the sputtering voltage, the critical temperature is pushed at higher temperatures so that the martensitic phase is stabilized at room temperature. On the contrary, films with lower thickness and/or grown at lower voltage show a coexistence of austenite and martensite at room temperature.

In order to achieve a deeper comprehension, a thorough structural characterization by means of XRD and electron microscopy and electron diffraction by TEM has been carried out. We show here the results for the 100 nm thick film grown at 900 V. Figure 5.21 and figure 5.22 show high resolution micrographs collected by TEM of the cross section of the film.

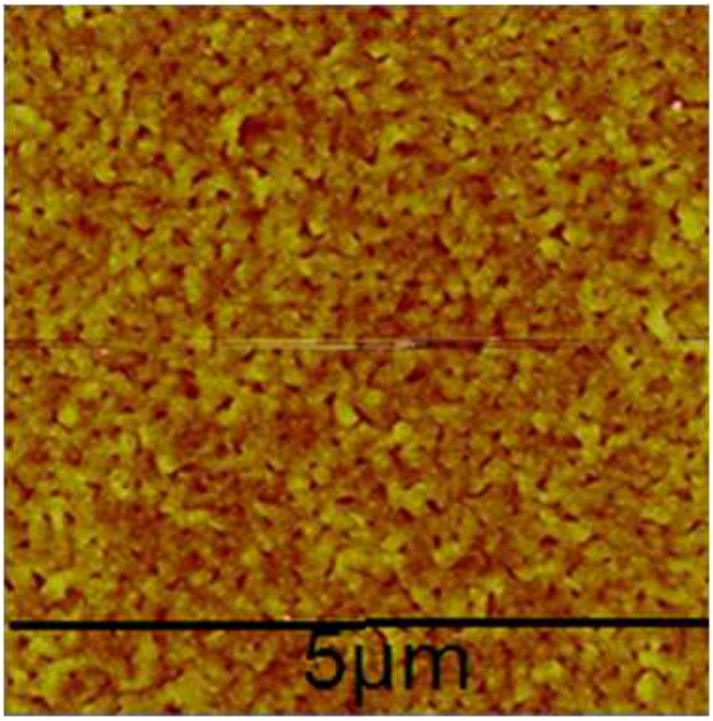

Figure 5.20: AFM signal of 75 nm thick NiMnGa grown on Cr/MgO

The martensitic twins are visible across the entire thickness of the Ni-Mn-Ga film, as well as some Cr intermixing into Ni-Mn-Ga , which protrudes above the Cr layer in some limited regions probably at the edges of the martensitic crystallites. According to the microprobe analysis of the TEM the composition of the film is slightly Ni-rich, i.e. Ni54Mn22Ga24.

Selected Area Electron Diffractions collected on different areas (figure 5.23) highlight the

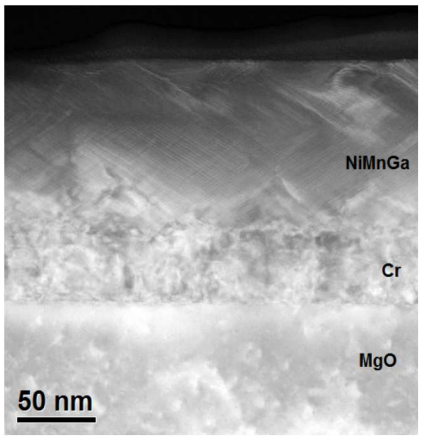

Figure 5.21: High Angle Annular Dark Field image of Ni-Mn-Ga 100 nm film (sample 1481)

symmetry of the martensitic phase and show the structural relations with the underlayer and

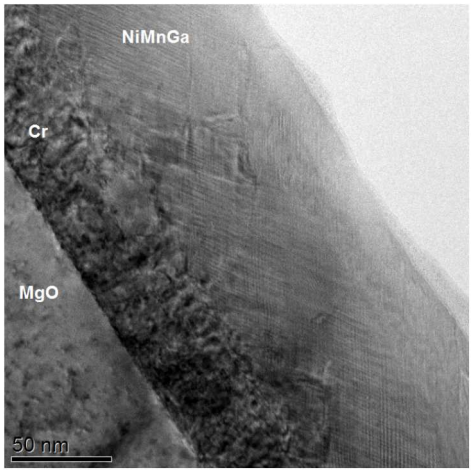

Figure 5.22: HRTEM image of Ni-Mn-Ga 100 nm film (sample 1481)

the substrate. The film and the underlayer grow epitaxially on MgO as expected from the mismatch analysis reported at the beginning of this paragraph. The Ni-Mn-Ga film is in the martensitic phase, showing a 7M monoclinic structure in accordance with previous literature for Ni-rich alloys [201]; the metric of this cell is quasi-tetragonal and in first approximation we can describe it as a deformation of the austenitic cubic cell. In this frame the martensite displays two basal axes, a and b, of approximately the same length and one unique axis, c, perpendicular to them. The angle between a and b is slightly different from 90 degree and the modulation (responsible for the satellite reflections observable in the figure 5.23) runs along one of the a-b diagonals. The martensitic basal axes are longer than the austenitic lattice parameter, while the c axis is considerably shorter.

Figure 5.24 shows the XRD pattern measured in Bragg-Brentano geometry on the same film. The measure highlights the epitaxial growth of (200) Cr on MgO and of Ni-Mn-Ga on Cr. The peak position is consistent with the occurrence of one of the basal axes of martensite perpendicular to the film plane, and therefore the unique axis c lays on the film plane. This configuration is consistent with TEM analysis and also with mismatch considerations: in fact, as the Cr lattice parameter is shorter than the austenitic and basal martensitic ones, the Ni-Mn-Ga films experiences a compressive stress on the film plane. This configuration promotes the growth of a martensitic phase with the shorter c axis on the film plane. The overall epitaxial relations of the Ni-Mn-Ga/Cr films is sketched in figure 5.25. It is interesting to observe that either by TEM nor by XRD it is possible to observe the occurrence of austenitic phase in the 100nm thick, 900 V film. This is apparently in contrast with the first considerations that

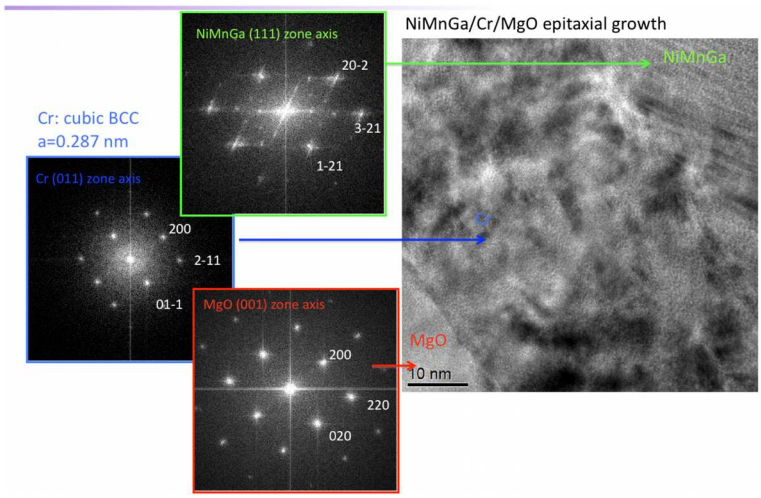

Figure 5.23: High resolution TEM image (right) and SAED collected on the different materials on 100 nm film (sample 1481).

we inferred by the AFM observations of the morphology. Therefore it propose the hypothesis that, contrary to what observed in NiMnGa on Mgo films, the presence of the Cr underlayer induces a different twin configuration of the martensitic phase where surface height modulation is no longer required.

The magnetic characteristics at different temperatures have been measured by means of AGFM in both parallel and perpendicular configuration. The loops are very similar for all the analyzed samples and here we show just the 100 nm sample grown at 900 V as a function of temperature. The saturation magnetization for 100 nm sample at room temperature is $(400 \pm 20)\ emu/cm^3$ and coercivity field in plane is $(154 \pm 5) Oe$. The in-plane measurements are consistent with the structural analysis presented above, the martensitic c axis being the easy magnetization direction. The MFM signal is very low for all the samples. The values for other samples are very similar.

5.3.4 Ni-Mn-Ga nanodisks

An array of dots have been obtained by the deposition of a monolayer of polystyrene nanospheres on thin films, and, after the deposition, the sphere size is lowered by using a Reactive Ion Etching (RIE). The spheres act as mask during a sputter etching with Ar ions, in this way the film not covered by sphere is removed. For the moment we have lithographyed the thinner film in order to control and study the process. After the lithography the sphere can be removed with specific solvents. In figure 5.27 we can see a SEM image of disk with spheres on it and then

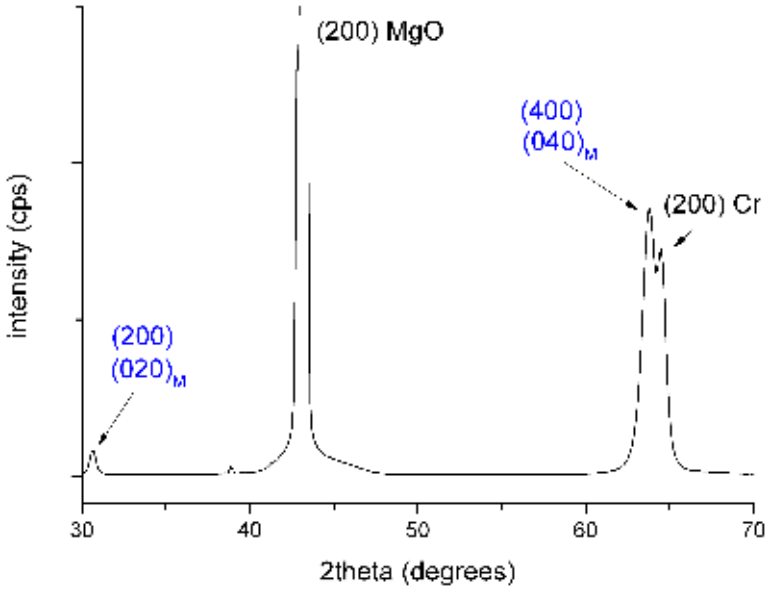

Figure 5.24: XRD pattern collected at room temperature of the 100 nm thick, 900 V Ni-Mn-Ga film grown onto Cr underlayer (sample 1481)

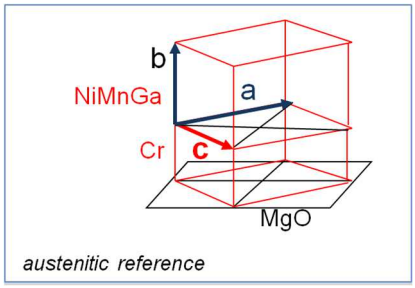

Figure 5.25: Growth mechanism of NiMnGa on Cr/MgO

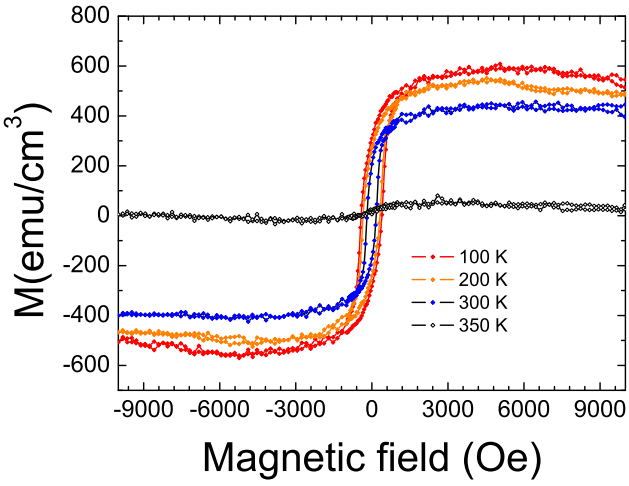

Figure 5.26: Magnetic loops at different temperatures for 100 nm Ni-Mn-Ga film grown at 900 V (sample 1481)

disks after sphere removing. So we have obtained nanodisks on MgO now we are studying the

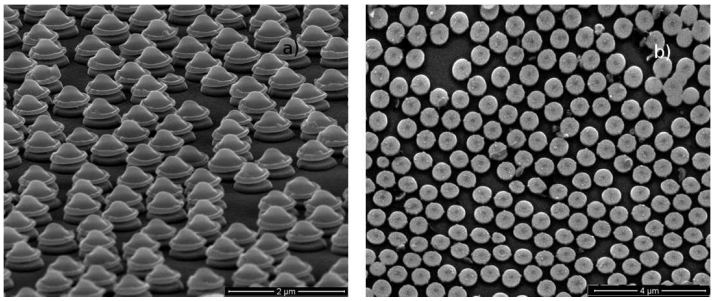

Figure 5.27: SEM image of Ni-Mn-Ga nanodisks: a) with sphere on it, b) after sphere removing

magnetic characteristics, and the preliminary results show a very interesting behavior, in fact as shown in figure 5.28 the hysteresis loop in plane does not change its shape. This is a good indication of the fact that magnetic characteristics are not changed.

5.3.5 Conclusions

In conclusion we have obtained magnetic thin films of NiMnGa on Cr under layer after having optimized the growth parameters. A complete study has been done on continuous film. The film has been lithographyed thanks to a self assembly nanosphere technique. Now we are going to study the disks characteristics and thanks to the Cr presence we are going to remove the disks from substrate. The free disks can be used as actuators for new biomedicine applications

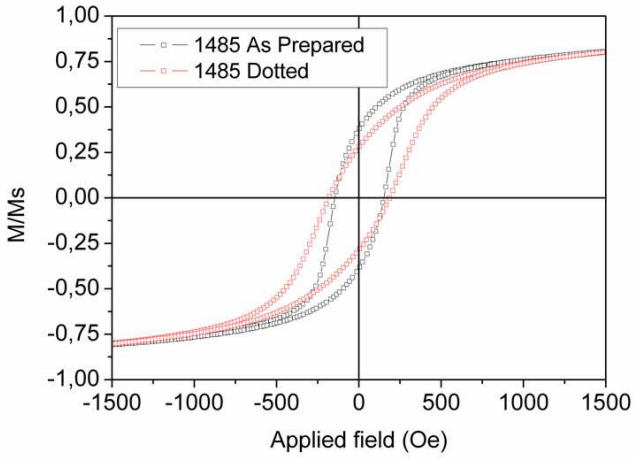

Figure 5.28: Hysteresis loops at room temperature of continuous film (blu line) and on dotted film (red line)

as for example the cell death induced by the movement induced by shape memory, but also as sensor or for other applications.

Chapter 6

Conclusions

In this thesis we have deepened and tailored the effects of size reduction of magnetic nanomaterials in order to exploit the arising new phenomenology in novel multidisciplinary applications.

Soft magnetic thin films constituted by amorphous Co-based alloys have been prepared by means of sputtering and fully characterized. Stress anisotropy induced during growth has been modeled and eliminated by means of suitable growth procedures and heat treatments. New chemical compositions have been proposed and exploited in order to reduce the number of the constituent elements, simplify the preparation procedure, make it compatible with Si technologies, and improve the functional properties. The films were initially grown on a Si substrate by r.f sputtering at IMEM-CNR. Subsequently, the growth recipe was transferred to STMicroelectronics and the preparation process was integrated in a silicon line technology. We have demonstrated for the first time the possibility to integrate a Co-rich amorphous soft-magnetic thin film as magnetic concentrator into a 8" silicon Bipolar CMOS DMOS technology Hall sensor Integrated Circuit.

Magnetic particles of nanometric size (MNPs) have also been widely studied. Magnetite/maghemite MNPs have been prepared by different techniques and the dependence of physical properties on chemical synthesis and functionalization has been investigated. We have found that the functionalization changes the possible interactions between nanoparticles, while size is mainly dependent on chemical synthesis. The most important nanoparticles phenomenology is related to the transition from ferromagnetic to superparamagnetic regime by decreasing size, the interactions between MNPs and surface effects. These properties were studied and controlled in order to exploit them in two possible applicative fields: magnetic hyperthermia and magnetic separation. Important new results have been obtained in both fields. MNPs of dimensions ranging from 4 nm and 8 nm have been produced. For magnetic

separation the best solution in order to have superior extraction performances obtaining lower limits of quantification values in the low ng/l range using a rapid and low-cost procedure, has been identified in diphenyl coated 4 nm MNPs embedded in aggregates of 200 nm. In the case hyperthermia application, the nanoparticles of 8 nm have been proved to show high values of specific absorption rate up to 50 W/g, that increase by increasing inter-particles interactions. Exchange-bias FeO/Fe_3O_4 core shell nanoparticles have also been studied, Two different shapes, cubic and spherical, have been analyzed demonstrating a strong influence of both properties on the possible realization of composite core-shell nanoparticles showing exchange-bias effect.

Moreover, MNPs have been used to prepare nanocomposite multifunctional semiconductive-magnetic nanostructures by means of physical method, in order to combine in one material the complementary properties of the two components. Two different semiconductors have been chosen: ZnO and SiC, for their extraordinary characteristics. In ZnO tatrapods, the MNPs have been linked through thermal treatment, while on SiC wires the MNPs have been linked by means of click chemistry. In the case of ZnO, the MNPs have been fond not to have a uniform distribution on tetrapod legs, forming some particles and aggregates. These two phenomena are at the origin of the small hysteresis shown by the material at room temperature; the magnetic remanence was found to be very low. We have fond that the peculiar characteristics of ZnO, and in particular the photoluminescence properties, have been conserved in nanocomposites materials, making them promising for multifunctional applications (e.g. photodynamic and magnetic hyperthermia combined therapies). MNPs on SiC have been instead uniformly distributed. The interactions between MNPs are negligible and the magnetic properties have been conserved also in nanocomposite materials.

In the last part of this thesis dots of ferromagnetic shape memory Ni-Mn-Ga have been realized by nanosphere lithography of thin films. A study on the effect of size reduction on the main properties is in progress. This intrinsically multifunctional material could be used as magnetic actuator or as active element as nano-medicine agent, even if its biocompatibility is not known. These important findings, that will be further deepened and improved, pave the way to novel applications of magnetic material.

Last but not least, this thesis, due to its multidisciplinary vocation, offered me the extraordinary possibility to enter in strong contact with many research groups both in academia and in industry involved in several research topics e.g. physics, chemistry, technological de-

velopment, medicine, biology.

Bibliography

[1] C. Kittel. *Introduction to solid state physics*. Wiley, 2005.

[2] B. D. Cullity and C. D. Graham. *Introduction to magnetic materials*. Wiley, 2009.

[3] M. Getzlaffi. *Fundamentals of Magnetism*. Springer, 2008.

[4] J. Frenkel et al. *Nature*, 126:274, 1930.

[5] R. O Handley. *Modern Magnetic Materials Principles and Applications*. Wiley-Interscience, 2000.

[6] E.C. Stoner et al. *Phil. Trans. Roy. Soc.*, A 240:599, 1948.

[7] S. Betanda et al. *J. Phys. D App. Phys.*, 42:013001, 2009.

[8] L.Neel. *Ann. Geophys.*, 5:99, 1949.

[9] W. F. Jr. Brown. *Phys. Rev.*, 130:1677, 1963.

[10] S. Blundell. *Magnetism in condensed matter*. New York Oxfor University Press, 2001.

[11] M. Sasaki et al. *Phys. Rev. B*, 71:104405, 2005.

[12] O. Petracic et al. *J. Magn. Magn. Mater.*, 300:192, 2006.

[13] J. Mydosh. *Sping Glasses: An Experimantal Introduction*. London: Taylor and Francis, 1993.

[14] M. F. Hansen et al. *J. Phys.: Condens. Matter*, 14:4901, 2002.

[15] S. Morup et al. *J. Magn. Magn. Mater.*, 40:163, 1983.

[16] I. S. Beloborodov et al. *Phys. Rev. Lett.*, 99:066602, 2007.

[17] D. Fiorani. *Suraface Effect in Magnetic Nanoparticle*. Springer, 2005.

[18] J. M. Coey. *Phys. Rev. Lett.*, 27:1140, 1971.

[19] R. H. Kodoma et al. *Phys. Rev. Lett.*, 77:394, 1996.

[20] W.H. Meiklejohn et al. *Phys. Rev.*, 102:1413, 1956.

[21] R.L. Stamps et al. *J. Phys. D: Appl. Phys.*, 33:R247, 2000.

[22] M. Kiwi et al. *J. Magn. Magn. Mater.*, 234:584, 2001.

[23] R. Coehoorn. *Handbook of Magnetic Materials*. North-Holland, Amterdam, 2003.

[24] J. Nogues et al. *Physics Reports*, 422:65, 2005.

[25] R. Harris et al. *Phys. Rev. Lett.*, 31:160, 1973.

[26] Y. Imry et al. *Phys. Rev. Lett.*, 35:1399, 1975.

[27] R. Schafer A. Hubert. *Magnetic Domains*. Springer, 2009.

[28] J.Yu et al. *J. Appl.Phys.*, 91:8357, 2002.

[29] M. Coisson et al. *J. Mag. Mag. Mat.*, 321:806, 2009.

[30] A.G. Roca et al. *J. Phys. D: Appl. Phys.*, 42:224002, 2009.

[31] F. D. Czeschka. *Ph.D. thesis,Munchen University, Facolta di Scienze Matematiche Fisiche Naturali*, 2007.

[32] S. Foner et al. *Rev. Sci. Instrum.*, 30:548, 1959.

[33] P.J.Flanders et al. *J.Appl.Phys*, 63:3940, 1988.

[34] J. R. Brauer. *Magnetic actuators and sensors*. Wiley-Interscience, 2006.

[35] P. Ripka. *Sens. Act. A*, 106:8, 2003.

[36] F. Celegato et al. *Phys. Stat. Sol. A*, 205:1745, 2008.

[37] S.N. Kane et al. *Cur. App. Phys.*, 11:981, 2011.

[38] B.Ahamada et al. *J. Mag. Mag. Mat.*, 242:1443, 2002.

[39] J. Petzold et al. *J. Mag. Mag. Mat.*, 242:84, 2002.

[40] J. Yu et al. *J. App. Phys.*, 91:8357, 2002.

[41] N. Kaushik et al. *App. Phys. Lett.*, 97:072510, 2010.

[42] S. Ikeda et al. *J. App. Phys.*, 93:082508, 2008.

[43] T. O Donnell et al. *J. Mag. Mag. Mat.*, 322:1690, 2010.

[44] D. S. Gardner et al. *J. App. Phys.*, 103:07E927, 2008.

[45] H.P.J. Wijn. *Landolt Bornstein New Series*, volume 19. Springe Verlag, 1991.

[46] Vacuumschmelze. URL `"www.vacuumschmelze.de"`.

[47] D. Riccardi et al. *19th ISPSD Proceedings.*, page 73, 2007.

[48] Z. B. Randjelovic et al. *Solid State Circuits*, 37:151, 2002.

[49] M.Marchesi. *Fluxgate Magnetic Sensor System for Electronic Compass.* Ph.D Thesis, UniversitÃ di Pavia, 2005.

[50] S.O. Choi et al. *Sensors and Actuators A*, 55:121, 1996.

[51] L. Chiesi et al. *Sensors and Actuators*, 82:176, 2000.

[52] F. Casoli et al. *Scripta Mat.*, 48:955, 2003.

[53] F. Casoli et al. *Acta Mat.*, 58:3596, 2010.

[54] J.A.Thornton. *Ann. Rev. Mater. Sci.*, 7:239, 1977.

[55] J.A.Thornton et al. *Thin Solid Films*, 171:5, 1989.

[56] T. J. Klemmer et al. *J. App. Phys.*, 87:830, 2000.

[57] K. Ozawa et al. *J. Mag. Mag. Mat.*, 35:289, 1983.

[58] L. M. Alvarez-Prado et al. *Physica B*, 343:241, 2004.

[59] A. R. Chezan et al. *J. Mag. Mag. Mat.*, 299:219, 2006.

[60] B. Peng et al. *J. Mag. Mag. Mat.*, 318:14, 2007.

[61] B. Peng et al. *J. App. Phys.*, 101:09C511, 2007.

[62] P. Sharma et al. *Phys. Rev. B*, 73:052401, 2006.

[63] J. McCord et al. *J. Mag. Mag. Mat.*, 271:46, 2004.

[64] M. Coisson et al. *J. App. Phys.*, 104:03392, 2008.

[65] Q. A. Pankhurst et al. *J. Phys. D: Appl. Phys.*, 42:224001, 2009.

[66] A. Figuerola et al. *Pharmacological Research*, 62:126, 2010.

[67] M. Tanase et al. *Lab. Chip.*, 5:598, 2005.

[68] J. P. Desai et al. *Annu. Rev. Biomed. Eng.*, 9:35, 2007.

[69] D. W. Inglis et al. *J. Appl. Phys.*, 99:08K101, 2006.

[70] D. W. Inglis et al. *J. Appl. Phys.*, 99:08K101, 2006.

[71] M. T. Bryan et al. *Appl. Phys. Lett.*, 96:192503, 2010.

[72] G. Li et al. *Sensors and Actuators A*, 126:98, 2006.

[73] M. Donolato et al. *Adv. Mater.*, 22:2706, 2010.

[74] U. Lehmann et al. *Angew. Chem. Int. Ed.*, 45:3062, 2006.

[75] V. Sivagnanam et al. *Langmuir*, 26:6091, 2010.

[76] Yicheng Ni. *Current Medical Imaging Reviews*, 4:96, 2008.

[77] S. Biederer et al. *J. Phys. D: Appl. Phys.*, 42:205007, 2009.

[78] C. Sun et al. *Advanced Drug Delivery Reviews*, 60:1252, 2008.

[79] T. Neuberger et al. *J. Mag. Mag. Mat.*, 293:483, 2005.

[80] M. O. Aviles et al. *J. Mag. Mag. Mat.*, 320:2704, 2008.

[81] Gazeau et al. *Nanomedicine*, 3:6, 2008.

[82] I. Sharifi et al. *J. of Mag. Mag. Mat.*, 324:903, 2012.

[83] Q.A. Pankhurst et al. *J. Phys. D: Appl. Phys.*, 36:R167, 2003.

[84] T. Rheinlander et al. *J. Magn. Magn. Mater.*, 219:219, 1999.

[85] K.J. Widder et al. *Proc. Soc. Exp. Biol. Med.*, 58:141, 1978.

[86] A. Senyei et al. *J. Appl. Phys.*, 49:3578, 1978.

[87] B. Gleich and J. Weizenecker. *Nature*, 435:1214, 205.

[88] B. Gleich et al. *Phys. Med. Biol.*, 35:N 81, 2008.

[89] W.J. Atkinson et al. *IEEE Trans. Biomed. Eng..*, 31:70, 1984.

[90] B. Hildebrandt et al. *Crit. Rev. Oncol. Hematol.*, 43:33, 2002.

[91] K. Maier-Hauff et al. *Int. J. Neurooncol.*, 241:317, 2011.

[92] R. W. Chantrell et al. *J. Phys. D: Appl. Phys.*, 21:1469, 1988.

[93] M. El-Hilo et al. *J. Magn. Magn. Mater.*, 117:307, 1992.

[94] A. M. de Witte et al. *J. Magn. Magn. Mater.*, 120:184, 1993.

[95] R.E. Rosensweig. *J. Magn. Magn. Mater.*, 252:370, 2002.

[96] R. Ramprasad et al. *J. Appl. Phys.*, 96:519, 2004.

[97] R. Hergt et al. *J. Phys.: Condens. Matter*, 20:385214, 2008.

[98] G. Goya et al. *IEEE Trans. on Mag.*, 44:4444, 2008.

[99] M.A.Gonzalez-Fernandez et al. *J. Sol. State Chem.*, 182:2779, 2009.

[100] G. Goya et al. *J. Magn. Magn. Mater.*, 316:132, 2007.

[101] I. Shafiri et al. *J. Mag. Mag. Mat.*, 324:903, 2012.

[102] M. Jeun et al. *Appl. Phys. Lett.*, 95:082501, 2009.

[103] H. Kobayashi et al. *J. of Appl. Phys.*, 107:09B322, 2010.

[104] Y. Pinero et al. *Nanoscale Research Letters*, 6:383, 2011.

[105] R.M. Cornel et al. *The Iron Oxides.* Wiley-VCH, 2003.

[106] W.H. Bragg. *Nature*, 95:561, 1915.

[107] L. Neel. *Ann. Phys. Fr.*, 3:137, 1948.

[108] P. Weiss and K. Renger. *Arch. Elektrotechn.*, 11:406, 1914.

[109] T. Okamura. *Sci. Rep. Tohoku Imp. Univ.*, 21:231, 1932.

[110] G.S. Parks et al. *J. Phys. Chem.*, 30:47, 1926.

[111] R.W. Millar. *J. Am. Chem. Soc.*, 51:215, 1929.

[112] B.S. Ellefson et al. *J.Chem. Phys.*, 2:58, 1934.

[113] E.J.W. Verwey. *Nature*, 144:327, 1939.

[114] F. Walz. *J. Phys.: Condens. Matter*, 14:R285, 2002.

[115] M. Pai et al. *J. Phys. C*, 16:L35, 1983.

[116] J. R. Drabble et al. *Solid State Commun.*, 9:275, 1971.

[117] R. L. Bickford. *Phys. Rev.*, 78:449, 1950.

[118] S.C. Abrahams and B.A. Calhoun. *Acta Crystallogr.*, 6:105, 1953.

[119] S.C. Abrahams and B.A. Calhoun. *Acta Crystallogr.*, 8:257, 1955.

[120] W.C. Hamilton. *Phys. Rev.*, 110:1050, 1958.

[121] L. Bickford et al. *Proc. IEEE*, 104:238, 1957.

[122] R.M. Bozorth H.J. Williams. *Phys. Rev.*, 31:1107, 1953.

[123] B.A. Calhoun. *Phys. Rev.*, 6:1577, 1954.

[124] R. Aragon. *Phys. Rev. B*, 46:5334, 1992.

[125] G. F. Goya et al. *J. Appl. Phys.*, 94:3520, 2003.

[126] S. K. Ramasesha et al. *Phys. Rev. B*, 50:13789, 1994.

[127] P. Poddar et al. *Phys. Rev. B*, 65:172405, 2002.

[128] H. Seo et al. *Phys. Rev. B*, 65:085107, 2002.

[129] M. P. Morales et al. *Chem. Mater.*, 11:3058, 1999.

[130] A. Muan et al. *Phase Equilibria Among Oxides in Steelmaking*. Oxford: Addison-Wesley ed., 1965.

[131] W.H. Bragg and W.L. Bragg. *X-rays and crystal structure 3d*. G. Bells and Sons London, 1918.

[132] X. Wang et al. *Nature*, 437:121, 2005.

[133] J. Park et al. *Nat. Mater.*, 3:891, 2004.

[134] G. Clavel et al. *Adv. Funct. Mater.*, 17:3159, 2007.

[135] R.Massart. *IEEE Trans. Mag.*, 17:1247, 1981.

[136] S. Luo et al. *Chem. Commu.*, page 5719, 2008.

[137] W. Stober et al. *J. Coll. Inter. Sci.*, 26:62, 1968.

[138] G. Prencipe et al. *Chem. Commun.*, page 6017, 2009.

[139] F. Cattaruzza et al. *Chem. Mater.*, 17:3316, 2005.

[140] C.P. Lindsey and G.D. Petterson. *J. Chem. Phys.*, 73:3348, 1980.

[141] P. Allia et al. *Phys. Rev. B*, 60:12207, 1999.

[142] P. Allia et al. *Phys. Rev. B*, 64:144420, 2001.

[143] X. Sun et al. *NanoLett.*, 12:246, 2011.

[144] B. P. Pichon et al. *Chem. Mat*, 23:2886, 2011.

[145] L. M. Bronstein et al. *Langmuir*, 27:3044, 2011.

[146] M.V. Kovalenko et al. *J. Am. Chem. Soc.*, 129:6352, 2007.

[147] G. Salazar-Alvarez et al. *J. Am. Chem. Soc.*, 130:13234, 2008.

[148] D. Kim et al. *J. Am. Chem. Soc.*, 131:454, 2009.

[149] B. Luigjes et al. *J. Phys. Chem. C*, 115:14598, 2011.

[150] P. Guardia et al. *Langmuir*, 26:5843, 2010.

[151] P.D. Cozzoli et al. *Nano Lett.*, 6:1966, 2006.

[152] J. Park et al. *Nature Mat.*, 3:891, 2004.

[153] R. Buonsanti et al. *J. Am. Cem. Soc.*, 128:16953, 2006.

[154] R. Buonsanti et al. *J. Am. Cem. Soc.*, 132:2437, 2010.

[155] M. Casavola et al. *Nano Lett.,*, 7:1386, 2007.

[156] M. Casavola et al. *Nano Lett.,*, 9:366, 2008.

[157] P. Yang et al. *Adv. Mater.*, 12:323, 2002.

[158] H.W. Ryu et al. *Sens. Actuator B*, 96:717, 2003.

[159] G. Sberveglieri. *Sens. Actuator B*, 23:105, 1995.

[160] X.L. Cheng et al. *Sens. Actuator B*, 102:248, 2004.

[161] P. Sharma et al. *Nat. Mater.*, 2:673, 2003.

[162] H. Saeki et al. *Solid State Commun.*, 120:437, 2001.

[163] S. Fujita et al. *J. Cryst. Growth*, 272:138, 2004.

[164] H. Zhou and Z. Li. *Mater. Chem. Phys.*, 89:326, 2005.

[165] D. W. Zeng et al. *Appl. Phys.*, A79:1865, 2004.

[166] J. Zhang et al. *Cryst. Growth Des.*, 4:309, 2004.

[167] Y. H. Leung et al. *Chem. Phys. Lett.*, 394:452, 2004.

[168] H. Zhang et al. *Nanotechnology*, 15:622, 2004.

[169] P. X. Gao et al. *J. Phys. Chem. B*, 108:7534, 2004.

[170] M. C. DeRosa et al. *Coordination Chemistry Reviews*, 351:233, 2002.

[171] Y. Yamamoto et al. *Methods in Enzymology*, 29:319, 2000.

[172] S. Kishwar et al. *Nanoscale Res Lett.*, 5:1669, 2010.

[173] D. Calestani et al. *Sensors and Actuators B*, 144:472, 2010.

[174] R.S. DiPietro et al. *Appl. Phys. Lett.*, 96:222506, 2010.

[175] B.D. Plouffe et al. *J. Magn. Magn. Mat.*, 323:2310, 2011.

[176] L.S. Liao et al. *Appl. Phys. Lett.*, 66:2382, 1995.

[177] M. Yu et al. *Thin Solid Films*, 377:177, 2000.

[178] X.L. Wu et al. *Phys. Rev. Lett.*, 94:026102, 2005.

[179] X.M. Liu et al. *Nanotechnology*, 16:2932, 2005.

[180] C. Coletti et al. *Proc. 29th Annu. Int. Conf. IEEE EMBS*, 5849, 2007.

[181] G. Cicero et al. *Phys. Rev. Lett.*, 93:016102, 2004.

[182] P. Gomez Romero and C. Sanchez. *Functional Hybrid Materials.* Weinheim: Wiley-VCH, 2004.

[183] R.R. Allison et al. *Photodiag. Photodyn. Therapy*, 1:27, 2004.

[184] W. Chen et al. *J. Nanosci. Nanotechnol.*, 6:1159, 2006.

[185] F. Fabbri et al. *Nanotechnology*, 21:345702, 2010.

[186] R. Huisgen et al. *Chem.Ber.*, 100:2494, 1967.

[187] K. Ullakko et al. *Appl. Phys. Lett.*, 69:1966, 1996.

[188] I.E. Dikshtein et al. *JETP Letters*, 72:536, 2000.

[189] R. Kainuma et al. *Nature*, 439:957, 2006.

[190] G. Jakob et al. *J. Magn. Magn. Mater.*, 310:2779, 2007.

[191] M. Thomas et al. *New. J. Phys.*, 10:023040, 2008.

[192] C.A. Jenkins et al. *Appl. Phys. Lett.*, 93:234101, 2008.

[193] T. Eichhorn et al. *Mat. Sci. Forum*, 635:155, 2010.

[194] O. Heczko et al. *Appl. Phys. Lett.*, 92:072502, 2008.

[195] P. Leicht et al. *New J. Phys.*, 13:033021, 2011.

[196] A.Diestel et al. *Scripta Materialia*, 67:423, 2012.

[197] K.Kittel. *Phys. Rev.*, 70:956, 1946.

[198] T. Eichhorn et al. *Acta Mater.*, 59:5067, 2011.

[199] A. Backen et al. *Acta Mater.*, 58:3415, 2010.

[200] P. Ranzieri et al. *Acta Mat.*, 61:263, 2013.

[201] L. Righi et al. *Acta Mat.*, 56:4529, 2008.

Publications

P-1 F. Bianchi, V. Chiesi, F. Casoli, P. Luches, L. Nasi, M. Careri, A. Mangia *Magnetic solid-phase extraction based on diphenyl functionalization of Fe3O4 magnetic nanoparticles for the determination of polycyclic aromatic hydrocarbons in urine samples*, *J. Chromatogr. A* **1231** (2012) 8.

P-2 V. Palumbo, M. Marchesi, V. Chiesi, D. Paci, P. Iuliano, F. Toia, F. Casoli, P. Ranzieri, F. Albertini, and M. Morelli *Hall current sensor IC with integrated Co-based alloy thin film magnetic concentrator*, *European Physical Journal Web of Conferences* **40** (2013).

P-3 M. Villani, T. Rimoldi, D. Calestani, L. Lazzarini, V. Chiesi, F. Casoli, F. Albertini, A. Zappettini, *Composite multifunctional nanostructures based on ZnO tetrapods and superparamagnetic Fe_3O_4 nanoparticles*, submitted to *Nanotechnology* (2013).

This Thesis work has produced over twenty contributions to national and international scientific conferences.

Acknowledgments

I would like to express my heartfelt gratitude to my supervisors Dr. Franca Albertini and Dr. Francesca Casoli, for their constant and important support, teachings and helps. I would like to thank Prof. Antonio Deriu and Dr. Salvatore Iannotta for their guidance.
I am most grateful to all the people who have given an essential contribution to this research: Dr. Marco Campanini, Dr. Lucia Nasi, Dr. Marco Negri, Dr. Giancarlo Salviati, Dr. Marco Villani, Dr. Tiziano Rimoldi, Dr. Laura Lazzarini, Dr. Andrea Zappettini, Dr. Francesca Licci, Dr. Tullo Besagni at IMEM Parma; Dr. Elena Bedogni, Dr. Antonio Mega, Prof. Franca Bigi, Prof. Federica Bianchi at Chemistry Department of Parma University; Prof. Davide Cozzoli at NNL Lecce; Dr. Vincenzo Palumbo, Dr. Marco Marchesi, Dr. Dario Paci, Dr. Caterina Riva, Dr. Sonia Pirotta, Dr. Marco Morelli and all the researchers at STMicroelectronics with whom I have collaborated; Prof. Clara Marquina, Prof. Gerardo F. Goya, Prof. Ricardo Ibarra at University of Zaragoza (Spain); Dr. Federica Celegato, Dr. Paola Tiberto at INRIM Torino. I would like to thank all the people of Magnetic Materials group at IMEM for the help, work and teachings: Simone Fabbrici, Paolo Ranzieri, Lara Righi, Riccardo Cabassi, Fulvio Bolzoni, Antonio Paoluzi, Pierpaolo Lupo, César De Juliàn Fernàndez, Daniele Bono.
I thank the coordinator of physics doctorate Prof. Pier Paolo Lottici.

Infine ringrazio in italiano tutti gli amici di fisica, in particolare Carmen Mandalari, Stefano Mori e Davide Orsi per i loro suggerimenti ed aiuti. Un grazie speciale alla mia famiglia e a Luca.